Bloch Oscillations of Metastable Helium in an Optical Lattice

Ruud van der Beek

VRIJE UNIVERSITEIT

Bloch Oscillations of Metastable Helium in an optical lattice

ACADEMISCH PROEFSCHRIFT

ter verkrijging van de graad Doctor aan
de Vrije Universiteit Amsterdam,
op gezag van de rector magnificus
prof.dr. V. Subramaniam
in het openbaar te verdedigen
ten overstaan van de promotiecommissie
van de Faculteit der Exacte Wetenschappen
op woensdag 17 maart 2021 om 9.45 uur
in de aula van de universiteit,
De Boelelaan 1105

door

Rudolf Franciscus Hubertus Joseph van der Beek
geboren te Venlo

promotor:	prof.dr. H.L. Bethlem
copromotoren:	prof.dr. K.S.E. Eikema
	prof.dr. W.M.G. Ubachs

voor mijn ouders

This thesis was approved by the members of the reviewing committee:

prof.dr. A. Freise	(Vrije Universiteit Amsterdam)
dr. N.J. van Druten	(Universiteit van Amsterdam)
prof.dr. K.A.H. van Leeuwen	(Technische Universiteit Eindhoven)
prof.dr. S.Y.T. van de Meerakker	(Radboud Universiteit Nijmegen)
prof.dr. S. Guellati-Khélifa	(Laboratoire Kastler Brossel, Université P. et M. Curie)

This work has been funded by the Foundation for Fundamental Research on Matter (FOM), which is part of the Netherlands Organisation for Scientific Research (NWO), and has been carried out at the LaserLaB of the Vrije Universiteit Amsterdam.

The cover shows Bloch oscillations of a metastable helium BEC, recorded with horizontal absorption imaging on 29-04-2020 (even shots of data-runs 152 to 176). The atoms oscillate for 46 + 2 ms per consecutive image.

Printed by Ipskamp Printing B.V., Enschede
ISBN: 978-94-6421-247-1

Contents

CHAPTER 1

Introduction

1.1 Prologue & General Introduction

This thesis deals with an experiment that is one of many that are made possible by numerous decades of research, theorising and experimenting by physicists around the world. Being allowed to stand on the shoulders of giants enables us to investigate, with incredible detail, the workings of the universe we live in. And so, our understanding of the universe is ever increasing, as is our understanding that there are even more things we do not understand.

Lord Kelvin is often wrongly quoted by famously having said that physics was as good as solved. What he actually said was *"The beauty and clearness of the dynamical theory, which asserts heat and light to be modes of motion, is at present obscured by two clouds"* [1]. The first cloud he referred to, was the outcome of the Michelson-Morley experiments, disproving the existence of 'luminiferous ether', which was later solved by Einsteins theory of special relativity [2].

Kelvin also noted a second cloud, which referred to a problem with the theory explaining the black-body radiation effect, which was later coined 'the ultraviolet catastrophe' by Ehrenfest [3]. The Rayleigh-Jeans law nicely described the low energy part of the black-body radiation behaviour, but diverged to infinity in the ultraviolet, hence the dramatic

nickname. This cloud was addressed by Planck in 1900 by his theory of quantisation and led to the derivation of Planck's law, which correctly reproduced the data. Subsequently, Einstein used the introduced principle of quantised energy to explain the photo electric effect, which landed him the 1921 Nobel Prize and led to a paradigm shift from classical- to quantum mechanics [4–6].

This, to me, is an example that physics is never fully understood, finished or in any way complete. What may seem a hindering cloud, casting a small shadow over our understanding, may hide worlds of unknowns that could overthrow our entire way of thinking about how the universe works. It is this belief that fuels and justifies fundamental physics research, and makes it an exciting field to work in.

The main subject of this thesis is to demonstrate that helium is a promising candidate for matter wave interferometry, with the goal[1] of providing an improved value for the fine-structure constant, α. In particular, I show fast and efficient momentum transfer via Bloch oscillations in an optical lattice, and demonstrate the enhanced sensitivity offered by an ion-detector based detection scheme that is unique to He^*. The experiments are performed in a setup that was built to produce, slow down and trap ultracold ($\approx$0.2 μK) metastable ^{4}He atoms.

There are several ways of determining the fundamental constant α, of which atom interferometry with caesium and rubidium are two of the most accurate [7, 8]. Competing at a similar accuracy is a measurement of the electron anomalous magnetic moment that can be combined with Quantum Electrodynamics to also provide an accurate value for α [9].

Since the value obtained using atom interferometry has virtually no QED dependence, it can be seen as a consistency check in physics, linking cold

[1] Bringing metastable helium into the atom-interferometry community to measure α was Wim Vassen's big dream. He initiated the project and managed to get funding for it. Sadly, Wim passed away early 2019. I have (with the help of many others) continued the project to the best of my abilities, and with every big or small experimental milestone, Wim's enthusiasm came to mind about making helium perform magic through the rules of physics.

atomic physics to the field of single particle Penning traps and QED. A description of the fundamental principles of atom interferometry is given in Sec. 1.2.2. We aim to extend the field of matter wave interferometry to metastable helium because of several of its unique properties, among which are its low second-order Zeeman shift, its accurately known mass, its calculability (as it is the second simplest atom), and the possibility to detect the atoms efficiently with a micro-channel plate detector. These advantages are further described in section 1.3.

Although the scope of this research is profoundly fundamental, atom interferometry is a field with a wide range of applications. From gravitational wave detection proposals, accelerometry, to geodesy, atom interferometry is being employed in many fields, making it an exciting subject to work on [10–12].

This chapter will first deal with the role of the fine-structure constant in physics, its value, its history and the history of its value. Next, the helium atom and its beneficial properties for atom interferometry will be described, followed by a short description of the recent SI change and the consequences for this research.

1.2 The Fine-Structure Constant

The Standard Model of particle physics (SM) describes three of the four fundamental forces known to man; the weak- and strong nuclear force and the electromagnetic force. Though it has proven itself to be a very successful model, to this day it fails to include the gravitational force, meaning there is still much room for additions or revisions. The SM has been instrumental in predicting the existence and some of the properties of sub-atomic particles such as the top quark or gauge bosons such as the W- and Z-bosons. In recent years, perhaps the most well known reconfirmation of its validity has been the observation of the Higgs boson.

Particles' interaction with their surroundings and each other is governed by (the magnitude of) certain constants. There are several of these so called 'fundamental constants', whose values cannot be derived from first

principles but rather have to be measured in some way. A few of these constants sound familiar, such as the speed of light, Planck's constant or the gravitational constant, but most of them are a bit obscure to the average physicist and are related to particle physics and the mysterious workings of the SM with all its gauge fields and Yukawa couplings.

The fine-structure constant is a dimensionless fundamental constant which determines the strength of the electromagnetic interaction between elementary charged particles and can be written as

$$\alpha = \frac{e^2}{4\pi\epsilon_0\hbar c}, \tag{1.1}$$

where e is the electron charge, ϵ_0 is the vacuum permittivity, c the speed of light and $\hbar$ the reduced Planck constant, $h/2\pi$. Its value is usually given as $1/\alpha$, as this gives the illustrious number $\sim$137.

The value of α

The value of α has puzzled many generations of physicists since its introduction by Sommerfeld [13], over one hundred years ago. Pauli wrote in 1948; "*The theoretical interpretation of its numerical value is one of the most important unsolved problems in physics*" [14], and even concluded his Nobel Lecture with the statement that there would be no conclusion to his report on the exclusion principle and quantum mechanics as long as there is no established theory which determines the value of α [15].

Interestingly, in a 1916 paper [16], Sommerfeld changed the definition of α to twice the square root of the original version he introduced in 1915, because it seemed "*more natural*" to use a simple ratio of constants that also fitted the model. This means that the 1/137 almost would have been 1/75076, which might somehow have sparked less inspiration.

Speculations are still ongoing on why the fine-structure constants value is what we measure. Attempts at an explanation range from scientific to more obscure numerological ones, where using 'aesthetically pleasing' mathematical functions that usually involve power series or root functions of π attempt to provide a value. Other questionable 'explanations'

were for example the Eddington number, which was an approximation of the number of protons in the universe that 'proved' $1/\alpha$ to be an integer, or the introduction of an aether-like frame to replace relativity theory [17].

The anthropic principle is often invoked as a philosophical explanation, stating that the measured value is only such, because it allows an observer to exist to measure the value in the first place. Indeed, if the value of α were slightly different, life as we know it, could not exist [18]. This realization leads to many different questions, suggestions and conclusions by scientists, philosophers and theologists, but that is beyond the scope of this work. Lengthy philosophical papers about how the origin of the value of α should be interpreted, prove that several communities are still puzzled by this constant.

1.2.1 A short history of the Fine-Structure Constant and the rise of Quantum Electrodynamics

In 1885, Balmer discovered that a simple equation gave the relation between the visible wavelengths of hydrogen absorption lines [19]. This allowed him to predict the values of some unobserved lines and even correct some previous measurements. The formula was generalised by Rydberg in 1889 for all transitions in hydrogen and hydrogen-like atoms [20]. The discovery of a doublet in some of these lines in 1887 by Michelson and Morley [21], puzzled spectroscopists for some time. The introduction of the concept of quantisation in 1900 by Planck [22], initiated the quantum theory and served as the basis for Bohr's famous model of the structure of the atom [23]. He considered the Balmer lines in the hydrogen atomic spectra and was able to derive Balmers relation based on an atomic model with circular orbits of the electron around the core. The first introduction of the fine-structure constant came in 1916, when Sommerfeld extended Bohr's model to solve the observed and unexplained existence of doublet and triplet lines in the spectra of hydrogen [16].

Sommerfelds solution for these unexplained structures in the measurements was to allow electrons to make elliptical orbits around the core

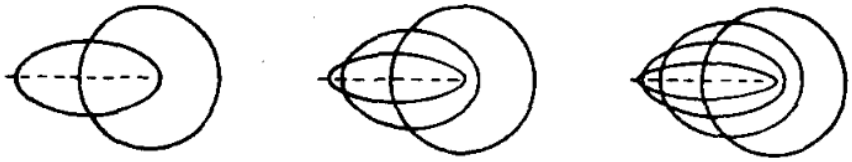

Figure 1.1 – *Sommerfelds introdution of elliptical orbitals as depicted in the original paper of 1916 [16].*

of the atom instead of circular orbits, and incorporating a relativistic correction for the mass of the electron at high velocity. By allowing n different possible orbits for each quantum number n, the splitting could be explained by the difference in energy between these orbits. The fine-structure constant was introduced as a ratio of velocities of the electron in different orbits around the core. Specifically, the ratio of the first momentum of an electron in the quantised orbital, to what Sommerfeld called the "*Grenzmoment*", being the limit of where an electron in a classical orbit around a core would begin to spiral inwards.

By using measurements of several other fundamental constants and the above mentioned spectra, Sommerfeld estimated the value of this "*charakteristische Konstante unsere Feinstrukturen*" to be $\sim 1/137$. This is also where the name comes from; in Sommerfelds paper, α emerged as a constant from the solution to the 'fine structures' in the hydrogen spectral data. He gave a first value for α^2 by stating that its magnitude was "*around* $5 \cdot 10^{-5}$"[16].

A follow up measurement by Paschen, initiated right after Sommerfelds presentation of the model in January of 1916, demonstrated that the extended Bohr model was successful in explaining the doublets and triplets. Paschen was happy to acknowledge Sommerfelds "*unermüdliche Bemühungen*" that led to the "*wundervollen Gesetze seiner schönen Theorie*" [24]. In 1940, Sommerfeld revisited α by commenting on its use in the description of actual fine-structure splitting as we know it today [51].

In 1947, Quantum Electrodynamics started being developed. Quantum mechanics, with the then recent inclusion of spin-orbit coupling, pre-

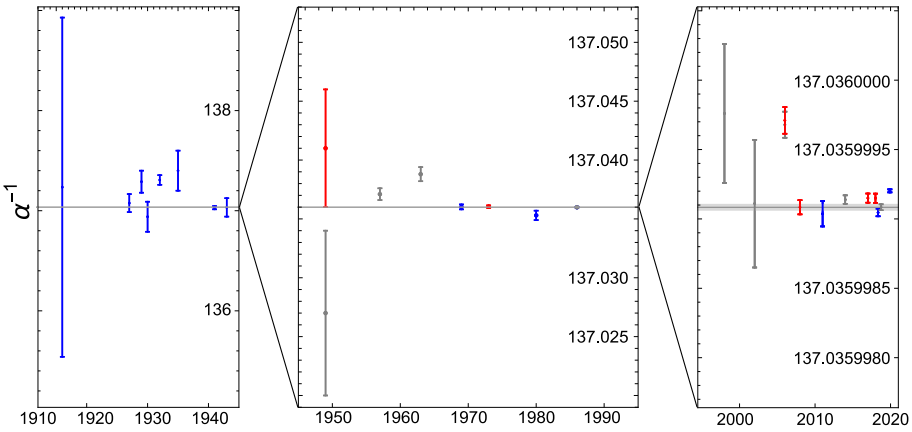

Figure 1.2 – *Accepted value of α^{-1} throughout the years. The blue colors indicate non-QED dependent measurements, such as the spectroscopic measurements from 1912 to 1945. The red datapoints indicate a determination that is QED-dependent, such as the 1949 α determination through electron g-factor measurements. The gray points show CODATA values, with the gray band at the 2018 agreed value. The panels zoom in with a factor ∼120 and ∼13000 respectively. From left to right: [24–33] - [34–40] - [7, 8, 41–50]*

dicted the observed fine splitting of energy levels in hydrogen levels but could not explain the observed splitting of the $2\ ^2S_{\frac{1}{2}}$ and $2\ ^2P_{\frac{1}{2}}$ levels in hydrogen. This observation of the so named 'Lamb shift' by Retherford and Lamb was theoretically resolved by Bethe [52–54], by combining quantum mechanics and Electrodynamics into one model: Quantum Electrodynamics (QED).

The theory proposes so-called vacuum fluctuations, particles that 'pop out' of the vacuum for very brief moments of time. This may seem unintuitive at first, but can be somewhat understood by considering the Heisenberg energy uncertainty principle

$$\Delta E \Delta t \geq \frac{\hbar}{2}. \tag{1.2}$$

This relation states that for an event that involves a particle, the prod-

ucts of the uncertainties of the quantities energy and time may not be smaller than a fixed value. It is important to note that this is not related to the uncertainty of a measurement device, but rather that it arises from quantum mechanics as an inherent property of nature.

In an intuitive view it is allowed for a certain amount of energy to come into existence, given it exists for a short enough time, without violating the energy conservation principle. These 'virtual' particles then interact with atoms and cause for example part of the now well known Lamb shift in the hydrogen atom. Because of its extremely accurate predictions of quantities such as the Lamb shift or the magnetic moment of the electron, Feynman famously dubbed QED 'the jewel of physics' [55].

The fine-structure constant became an object of study in experiments other than spectroscopy, for example in 1969 when Parker et al. [36] very accurately measured the ac-Josephson effect, thereby determining the value of e/h to an accuracy that allowed a new determination of α. This value was obtained with a solid-state type experiment, measuring voltages induced by tunneling effects of electrons through a barrier. As this measurement was independent of QED, the new value of α was an important step in the direction of testing QED itself, something that was also recognized by the authors [56].

In 'The Least-Squares adjustment of the Fundamental Constants' of 1973 [37], the first set of fundamental constants were published by the Committee on Data for Science and Technology (CODATA). In that article, the discussion about how to obtain a reliable value for α intensified. Many different methods (some with QED dependence and some without) provided slightly different values. Besides the ac-Josephson effect, which was by then investigated in detail in many labs, electron-g factor measurements, muonium[2] hyperfine splitting measurements and hydrogen hyperfine splitting contributed to the value. The authors felt the need to publish a separate value, listed under 'Without Quantum Electro Dynamics' (WQED), even though the difference in the final rec-

[2]Muonium is not, as one might expect, a combination of a muon and an anti-muon, but rather the combination of a positively charged anti-muon and an electron.

ommended value and the WQED value was only about half a standard deviation.

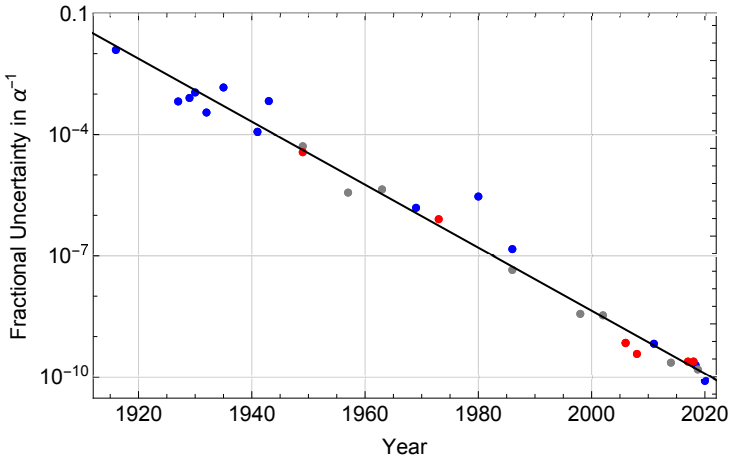

Figure 1.3 – *The fractional uncertainties of the α determinations in Fig. 1.2 are shown. A fit reveals that an order of magnitude in accuracy is gained every 12.8 year [7, 8, 24–50].*

In 1980, von Klitzing found that the quantum hall resistance is quantised, earning him the 1985 Nobel Prize [38]. He immediately realized that this also opened up a new method of measuring α, since the value of the measurable quantised Hall resistance, now called the von Klitzing constant, is expressed in units of h/e^2.

By 1986, the value of α was determined by a combination of measurements of the electron magnetic moment anomaly combined with accurate QED calculations, quantum Hall effect measurements and measurements of the muonium hyperfine structure [40]. The CODATA task group decided to no longer make the distinction between QED and WQED data or determinations, as "*There is no clear basis for any distinction between QED and WQED data*".

1.2.2 Current state of the art α determinations

As can be understood from the CODATA report of 2006, there are two very accurate ways of determining α; a combination of measurements of the electron magnetic moment anomaly combined with accurate QED calculations and measurements of the recoil velocity of an atom using atom interferometry. Both are explained further in this section.

QED-based α determination

Using a measurement of the electron magnetic moment, also called the electron g-factor, from the US-based Gabrielse group [9], and their high level Quantum Electrodynamics (QED) calculations, the group of Kinoshita in Japan arrived at $\alpha^{-1} = 137.0359991491(331)$, with an uncertainty of 0.24 ppb [49]. The basis of turning this measurement into an α determination is that, according to QED, the electron g-factor can be written as a series expansion in α

$$\frac{g}{2} = 1 + C_2(\frac{\alpha}{\pi}) + C_4(\frac{\alpha}{\pi})^3 + C_6(\frac{\alpha}{\pi})^3 ... + \alpha_{hadronic} + \alpha_{electroweak}, \quad (1.3)$$

where $\alpha_{hadronic}$ and $\alpha_{electroweak}$ represent contributions from hadronic and weak force interactions. The C_2, C_4 and C_6 coefficients can be calculated using QED theory and represent respectively second-, fourth- and sixth-order (and so on) Feynman diagrams. It is essential to calculate higher-order terms in order to keep the accuracy of the theory in step as the measurements become better and better. The series does not necessarily converge as the order goes up, but the contributions of higher orders do in practise become smaller [57].

The $\alpha_{hadronic}$ and $\alpha_{electroweak}$ contributions are small (order $\leq 10^{-12}$). The second- to sixth-order corrections have been calculated analytically, although as the order increases, the number of diagrams and their complexity increases rapidly. There are 9 two-loop (fourth-order) diagrams, but the amount of three-loop (sixth-order) diagrams is already 120, and their evaluation took approximately three decades to analytically evaluate, finishing in the 1990's [58].

Even with automation, correctly evaluating higher-orders is a formidable task, with 891 diagrams to evaluate for the 8th order term and a whopping 12.672 diagrams that had to be evaluated for the 10th order correction term [48, 49, 59, 60].

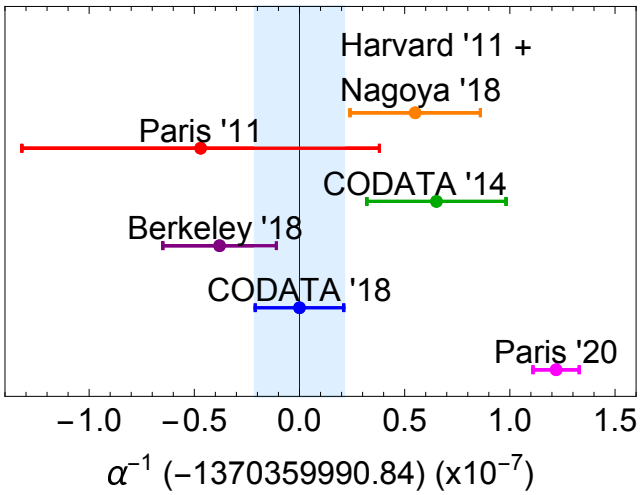

Figure 1.4 – *Current best determinations of the fine-structure constant α [46][47][49][7][50][8].*

Atom interferometry based α determination

The most precise value of α is currently set by the ENS group in Paris [8], reporting $\alpha^{-1} = 137.035999046(27)$ with an uncertainty of 0.08 ppb, by way of rubidium interferometry measurements. The Müller group in Berkeley [7] reported an experimentally determined value of $\alpha^{-1} = 137.035999046(27)$ with an uncertainty of 0.2 ppb in 2018, by way of caesium interferometry measurements.

The principle of these measurements is based on measuring the recoil velocity of an atom as it absorbs a photon

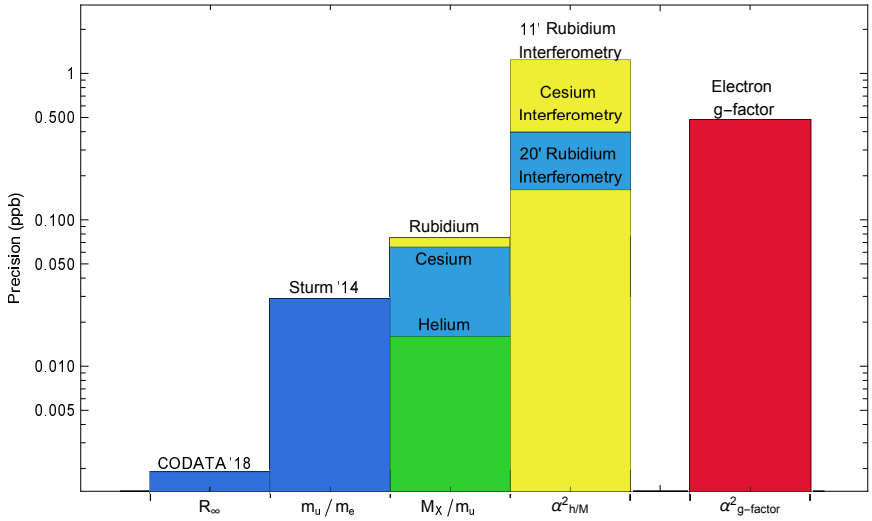

Figure 1.5 – *The three left bars represent the precision of the different factors shown in eq. 1.6 for the atom interferometry experiments. The fourth bar represents the α^2 value from atom interferometry measurements of h/M, whereas the fifth bar shows the α^2 value derived from the electron g-factor measurements and QED. It is clear that the limiting value in the interferometric determination is the precision of the measurement of $\hbar/M$ itself, and not yet any of the other terms in eq. 1.6. The green bar in the M_X/m_u column represents the precision that can theoretically be achieved with a helium measurement, given a better electron mass determination. Figure adapted from [61]. Data from [50],[62],[63],[46],[7],[8],[49].*

$$v_R = \frac{\hbar k}{m_{atom}}, \tag{1.4}$$

with the photon wavenumber k. This measurement provides a value for h/m_{atom}, which in turn can be used to determine α, when writing the fine-structure constant as

$$\alpha = \frac{2R_\infty}{c}\left(\frac{m_p}{m_e}\right)\left(\frac{m_{atom}}{m_p}\right)\left(\frac{\hbar}{m_{atom}}\right), \tag{1.5}$$

with the Rydberg constant R_∞, the proton mass m_p, the electron mass m_e and the mass of the atomic species m_{atom} used for the interferometric measurement. The interferometry is in this case a very precise tool to measure the recoil of the atom, because the induced phase shift by velocity differences can be measured very accurately, making a competitive α determination possible if the values of R_∞ and m_{atom} are known to sufficient precision.

For the experiment discussed in this thesis, we write the fine-structure constant as

$$\alpha = \frac{2R_\infty}{c}(\frac{m_u}{m_e})(\frac{m_{He^*}}{m_u})(\frac{\hbar}{m_{He^*}}), \tag{1.6}$$

with the mass of the metastable helium atom m_{He^*} and the atomic mass unit m_u. In Fig 1.5 the precision of the different terms in equation 1.6 are shown with respect to current measurement precisions.

1.3 Ultracold physics and the helium atom

After a short introduction on the basics of the ^{4}He, this section will describe the advantages of the helium atom for the measurements we intend to perform, specifically the possibility to detect the atoms with a micro-channel plate detector (MCP), the calculability of the helium atom, the low second-order Zeeman shift and its well known mass.

The helium atom has long been used as a testing ground for fundamental physics, with documented references dating back to for example Paschens use of helium spectroscopic measurements to provide a value for Sommerfelds newly introduced fine-structure constant in 1916. The use of helium with the cold-atom techniques began in the 1980's, with Aspects research on cooling metastable helium atoms (He*) below the single photon recoil velocity [64]. In 2001, the first Bose-Einstein condensates of metastable helium atoms were realised [65, 66], and in 2006

Variable	Value	Relative Uncertainty	units	
α^{-1} (g-factor + QED)	137.035 999 150 (33)	$2.4 \cdot 10^{-10}$		[45], [9], [60], [48]
α^{-1} (Exp. (Cs-133))	137.035 999 046 (27)	$2.0 \cdot 10^{-10}$		[7], [48]
α^{-1} (Exp. (Rb-87))	137.035 999 206 (11)	$0.8 \cdot 10^{-10}$		[8]
α^{-1} (CODATA 2018)	137.035 999 084 (21)	$1.5 \cdot 10^{-10}$		[50]
R_∞	10 973 731.568 160 (21)	$1.9 \cdot 10^{-12}$	m^{-1}	[50]
m_p	1.007 276 466 621 (53)	$53 \cdot 10^{-12}$	u	[50]
m_e	$5.485\,799\,090\,65\,(16) \cdot 10^{-4}$	$29 \cdot 10^{-12}$	u	[50], [62]
$(\frac{m_p}{m_e})$	1 836.152 673 43 (11)	$60 \cdot 10^{-12}$		[50]
m_{He} (GS)	4.002 603 254 130 (63)	$1.57 \cdot 10^{-11}$	u	[68]
m_{He^*} (2^3S_1)	4.002 603 275 407 (63)	$1.57 \cdot 10^{-11}$	u	[47], [68], [69], [70]

Table 1.1 – *List of relevant constants for determining α with helium-based atom-interferometry and their values.*

the first degenerate Fermi gas of metastable helium followed [67].

The level structure of helium, schematically shown in Fig. 1.6, shows the metastable 2^3S_1 state, which can be populated by using a helium plasma discharge source. The 1083.3 nm transition between the 2^3S_1 and 2^3P_2 states is a closed cooling transition which is used to laser cool He* atoms towards degeneracy.

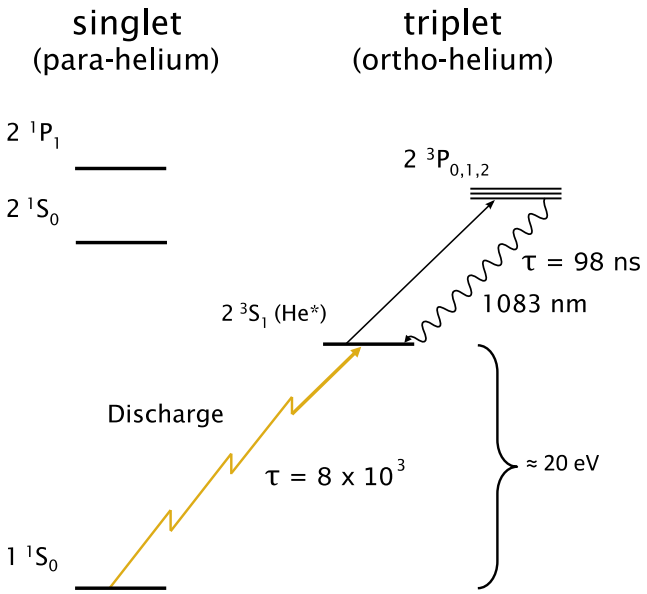

Figure 1.6 – *Helium level scheme, showing the important 1083.3 nm laser cooling transition and the 20 eV elevated metastable state, which can be populated using an electric discharge device.*

Due to the high internal energy of ∼20 eV of the metastable state, it is remarkable that He* can be cooled to quantum degeneracy, where the kinetic energy is approximately 10^{-10} eV. At first sight, the internal energy seems like a disadvantage, since He* is not easily generated and atoms will be mutually destructive, as they tend to de-excite when colliding through a process called Penning ionisation. Collisions of two He* atoms will result in the destruction of the metastable state through

two possible collisional channels,

$$\mathrm{He}^* + \mathrm{He}^* \rightarrow \begin{cases} \mathrm{He} + \mathrm{He}^+ + \mathrm{e}^- \\ \mathrm{He}_2^+ + \mathrm{e}^- \end{cases} \tag{1.7}$$

This loss process seemingly prevents the production of dense clouds of He^* atoms, but can be overcome by spin-polarising the sample [71]. This technique heavily suppresses Penning ionisation because the collisional channel of two atoms in an equal spin-stretched state is forbidden; the initial total spin of the set of atoms equals 2, but this cannot be conserved through an ionising collision, because the outcome products can not add up to a spin larger than 1 (neutral helium atom has spin 0, a He^+ ion, He_2^+ molecule and an electron all have spin $\frac{1}{2}$). This is somewhat analogous to the Pauli exclusion principle and enables cooling a spin-stretched sample towards degeneracy. With this hurdle out of the way, the 20 eV internal energy actually comes an enormous advantage.

1.3.1 MCP detection possibilities

The high internal energy enables detection methods based on electron multiplication techniques, since metastable atoms will decay to the ground state and release the internal energy into the surface they hit. Since 20 eV is higher than any metals work function, a collision will release an electron which can be detected with near unit efficiency [72]. This detection scheme provides both spatial and temporal resolution, when a position sensitive detector is used. An example of this is a study to demonstrate the Hanbury-Brown-Twiss effect with He^* atoms from 2007 [72]. Furthermore, Penning collisions in dense clouds result in production of ions and electrons, which can also be detected with electron multipliers, allowing in-situ measurements of the sample density or size.

1.3.2 Calculability

Due to its relative simplicity, being the second lightest atom after hydrogen, theorists also make grateful use of helium and its properties. The absence of orbital angular momentum in the ground state and its low mass means that relativistic effects are not very important and that electron spin is very nearly conserved in collisions. Combined with

spectroscopy techniques which allow for very accurate measurements of, for example, the Lamb shift, makes helium an excellent candidate for theory-experiment comparisons.

1.3.3 Zeeman shift

Using He* also brings advantages when it comes to systematic effects influencing the measurement error, e.g. due to the magnitude of the energy shift in magnetic fields. This effect is named after Pieter Zeeman who in 1897 described the splitting of spectral lines under the influence of a static magnetic field, earning him and Lorentz, who explained the phenomenon, the 1902 Nobel prize in Physics [73].

The Zeeman shift can cause problems since optical transitions and resonances are influenced in the presence of (stray) magnetic fields, which means a strict control of these fields is needed to perform precision experiments. Luckily, in ^{4}He*, one of the magnetic sub-states is an $m = 0$ level. This means the first-order shift can be completely neglected when the atoms are pumped into this state. Unfortunately, working with atoms in the $m = 0$ state is challenging because Penning ionisation is not suppressed, since they are not in a spin stretched state. There are some tricks to cancel the effect of magnetic fields, for example by combining measurements of $m = +1$ and $m = -1$ samples [74].

The second-order Zeeman shift arises from the diamagnetic term in the Hamiltonian and is non-zero, though with only 2.3 mHz/Gauss^2 [75][76], it is roughly 5 orders of magnitude smaller than the second-order Zeeman shifts in rubidium and caesium [77]. The shift in strontium is roughly twice as large [78]. Experimentally, the second-order shift cannot be negated by using an $m = 0$ sub-state or by alternating $m = +1$ and $m = -1$ measurements, because it is quadratic in B, the magnetic field, and therefore always goes in the same direction. Because the magnitude of the shift is so small for helium, it can usually be neglected.

1.3.4 The helium mass and the 2019 SI change

The mass of the helium atom comes into the α determination with helium-based atom interferometry in two ways, as can be seen in Eq. 1.6. The first entry into the equation is the $(\mathrm{M}_X/\mathrm{m}_u)$ term for which we find in Fig. 1.5 and from Table 1.2 that the precision for helium is better than those of the two other atomic species that are used for α-measurements. In the hypothetical (but intended future) case that the precision of the alpha determination experiments is improved, the limiting factor for rubidium and caesium is given by their respective mass determinations, while for helium it would be limited by the measurement of the electron mass, allowing for a potentially more accurate measurement.

It is interesting to note here that metastable helium has a slightly different mass than ground state helium because the 2^3S_1 state is 20 eV higher in energy. The precision with which we know the energy difference between these states exceeds that of the mass determination of the atom in the ground state, so it does not limit our experiment (see Table 1.3 [68], [69], [70]).

The mass also enters the measurement in the term that is actually derived from the photon-recoil measurement; $(\hbar/m_{He^*})$. This mass is, contrary to the previous entry in Eq. 1.6, not expressed in atomic mass units but in kg. This is exactly why this term previously had to be measured in such an elaborate way, since both the accepted value of Planck's constant and any atomic mass together did not allow an accuracy below that of h. This is because the atomic mass values, expressed in units of kg, were also limited by the definition of Planck's constant, since it is embedded into the conversion methods from amu to kg. Note the past tense here; the new situation is somewhat different.

On May 20th of 2019, the new International System of units (SI from the French Système International d'unités) was implemented. The SI change is a long-planned step in the ongoing transition from using real world objects to fundamental constants as the defining quantities for the system of units. The times of 'le grand K' as the definition of the

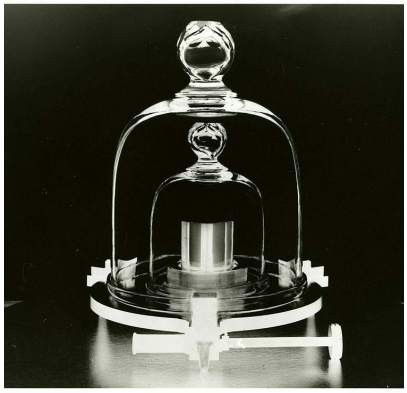

Figure 1.7 – *(A replica of) the International Prototype of the Kilogram, kept under the strict supervision of the Bureau des Poids et Mesures (BIPM). Until the 20th of May, 2019, it was the international standard of the kilogram. It has been superseded by the fixed definition of Planks constant.*

kilogram are over since the 2018 agreement in Versailles[3] to fix the value of Planck's constant to 6.626 070 15 $\times 10^{-34}$ kg m/s^2. This means that the kilogram is fixed by the definitions of the meter and the second, which in turn are interlocked by the definition of the speed of light, c=299 792 458 m/s ,while since 1967 the second has been defined as the duration of 9 192 631 770 periods of the radiation from the unperturbed ground-state hyperfine transition of Cs-133.

Thus, with a perhaps somewhat confusing transformation, at the start of this experimental project the measurement of the ratio of $\hbar/m_{He^*}$ was a measurement of the ratio of two measurable quantities, whereas after the SI change this quantity is purely a mass measurement, since $\hbar$ has been fixed by the 2019 SI definition.

It is now interesting to realize how the macroscopic kilogram is linked to microscopic masses and Planck's constant. In the new SI, the 'master' quantity is the fixed h, and it is linked through a Kibble Balance experiment[4] to the value of the macroscopic kg. The Kibble balance has an

[3] A fitting location, considering history, as France has long been at the leading edge when it comes to adopting and maintaining new standardizations of measurement practices, such as the introduction of the metric system at the end of the French Revolution in 1799 or the 1875 'Convention du Mètre', which established the system that would become the SI.

[4] Originally known as the Watt Balance for the unit of the measured quantities, it was renamed in 2016 in honour of its inventor Kibble.

accuracy of some parts in 10^8. This means that the kg is now defined with an accuracy of some tens of micrograms through this experiment, with h at the base of this determination. Planck's constant enters the determination via measurements of current and voltage, which are linked through the fixed value of the charge of the electron.

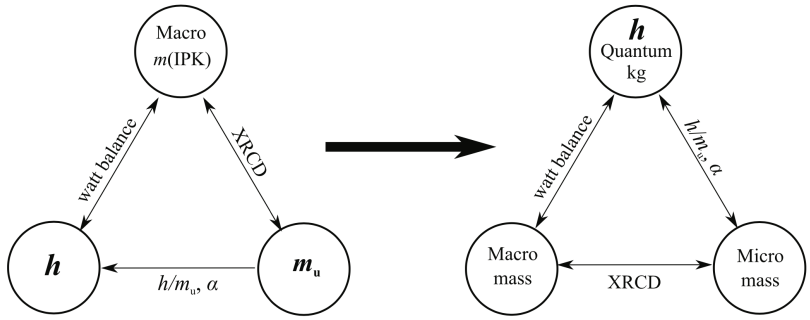

Figure 1.8 – *'Tilting' of the SI system. The old SI referenced to a master kilogram reference, the new SI references to the definition of Planck's constant, h. Figure taken from [79].*

Next to that, the atomic mass unit m_u is connected to h by measurements of the ratio h/m_{atom} by using the available values for m_{atom}/m_u for different atomic species (see Fig. 1.5 and Table 1.2). This means that measuring the photon recoil accurately not only allows α determinations but also provides a direct measurement of mass at the atomic scale.

Finally, the macroscopic kg and microscopic mass unit m_u are linked via the X-Ray Crystal Density method (XRCD), which is a determination of the number of atoms in a (as close to perfect as possible) silicon sphere through a measurement of a lattice constant with the use of x-rays. XRCD also has a $\sim 10^{-8}$ accuracy, which anchors the atomic mass unit to the real-world macroscopic definition of the kilogram. In the new system, XRCD still links the two mass units, but now it helps realise the kg through a measurement of h/m_u [79].

	Rb	Cs	Sr	He*	
Atomic mass number	87	133	88	4	
Atomic mass relative precision (ppb)	0.075	0.07	0.068	0.016	[47, 68]
Laser cooling wavelength (nm)	780	852	461	1083	
Electronic state	$5s\ ^2S_{1/2}$	$6s\ ^2S_{1/2}$	$5s^2\ ^1S_0$	$1s2s\ ^3S_1$	
2nd order Zeeman shift (Hz/G^2)	288	214	0.0055	0.0023	[75–78]
Lattice wavelength (nm)	780	866	532	1557.5	[7, 80, 81]
Lattice recoil velocity (cm/s)	0.64	0.35	0.85	6.40	

Table 1.2 – *Relevant numbers for different atomic species that are used in atom-interferometry.*

Variable	Value	Relative Uncertainty	units	
m_{He} (GS)	4.002 603 254 130 (63)	$1.57 \cdot 10^{-11}$	u	[68]
$Ion.E_{He}$ (GS)	24.587 387 (10)	$4.07 \cdot 10^{-7}$	eV	[70]
$Ion.E_{He^*}$ (2^3S_1)	4.767 774 451 (66)	$1.38 \cdot 10^{-8}$	eV	[47, 69]
$Int.E_{He^*}$ (2^3S_1)	19.819 612 (10)	$5.05 \cdot 10^{-7}$	eV	[47, 69]
$m_{additional}$ (2^3S_1)	0.000 000 021 277 (0.1)	$2.68 \cdot 10^{-15}$ (w.r.t. m_{He})	u	[47, 68–70]
m_{He^*}	4.002 603 275 407 (63)	$1.57 \cdot 10^{-11}$	u	[47, 68–70]

Table 1.3 – *Known values for several key properties of ^4He and He^*.*

1.4 Polarizability of atoms

The study of atomic physics has taken a huge flight after the introduction of the laser, which gave physicists precise control over the motion and internal states of atoms and molecules using resonant laser light. This allowed atoms to be cooled to such low temperatures that new and interesting physics came to light. The key to the improved and precise control of the atoms is understanding the interaction between light and the atoms. Of particular interest when discussing this subject is the dipole polarizability $\alpha(\omega)$ of the atom, which describes the response of an atom to an external electromagnetic disturbance.

When placed in an oscillating electric field, for example a laserbeam, an atom will exhibit an induced electric dipole moment which oscillates at the oscillation frequency of the field[5]. The magnitude of the induced dipole moment is determined by the strength and wavelength of the electric field and the dynamic polarizability $\alpha(\omega)$[6]. For a classical damped harmonic oscillator, with external field oscillation frequency ω, resonance frequency ω_0, and linewidth Γ, the polarizability can be described as

$$\alpha(\omega) = 6\pi\epsilon_0 c^3 \frac{\Gamma/\omega_0^2}{\omega_0^2 - \omega^2 - i(\omega^3/\omega_0^2)\Gamma}. \tag{1.8}$$

The potential energy $U_{dip}(\mathbf{r})$, that is associated with the induced dipole moment, is determined by the real part of the polarizability as

$$U_{dip}(\mathbf{r}) = -\frac{1}{2\epsilon_0 c}\mathrm{Re}(\alpha(\omega))\mathrm{I}(\mathbf{r}), \tag{1.9}$$

where $I(\mathbf{r})$ is the intensity of the radiation field. Complementary to the real part of the polarizability, the imaginary part is associated with the off-resonant scattering rate

$$\Gamma_{scatt}(\mathbf{r}) = -\frac{1}{\hbar\epsilon_0 c}\mathrm{Im}(\alpha(\omega))\mathrm{I}(\mathbf{r}), \tag{1.10}$$

[5] Given that the field strength is much less than the atomic field strength and the electromagnetic wavelength is much larger than the atom size [82].

[6] Note that there is also a static counterpart to the dynamic polarizability that gives the induced dipole response of an atom due to a static electric field.

which is the rate a which photons are absorbed and spontaneously re-emitted. When considering the atom to be a two-level system, the dipole potential can be seen as an effective AC Stark shift, shifting the ground- and excited state, while Γ is equivalent to the line width. In the far off-resonant case, where detuning $\Delta \equiv \omega - \omega_0$, satisfies $|\Delta| \gg \Gamma$, the dipole potential and scattering rate scale as [83]

$$U_{dip}(\mathbf{r}) \propto \left(\frac{\Gamma}{\Delta}\right) \frac{I(\mathbf{r})}{\omega_0^3}, \tag{1.11}$$

$$\Gamma_{scatt}(\mathbf{r}) \propto \left(\frac{\Gamma}{\Delta}\right)^2 \frac{I(\mathbf{r})}{\omega_0^3}. \tag{1.12}$$

Note that the scattering rate decreases faster than the dipole potential as the detuning increases, which is necessary to ensure that a deep enough dipole potential can be realised so that atoms can be nicely trapped, but do not heat up due to a high number of scattering events. A negative dipole potential (requiring positive $\alpha(\omega)$) allows for trapping of atoms, since the gradient of the intensity of the light field forms a conservative trapping force. In our case, the 1557 nm laser that is used for the optical dipole trap (see Chapter 4) is far red detuned from the closed transition at 1083 nm, so He^* can be considered a two-level system. At 1557 nm, the polarizability of He^* is [84]

$$\alpha(\lambda = 1557.3 \text{ nm}) = 604\ a_0^3 = 9.96 \times 10^{-39} \text{JV}^{-2}\text{m}^2. \tag{1.13}$$

Knowledge of the dynamic polarizability is not only useful for finding convenient wavelengths for trapping atoms, the precision of modern optical lattice clocks relies on the precise control of atomic polarizability [85]. The (static and dynamic) polarizability is determined both by the frequencies of atomic transitions, which are routinely measured with a relative accuracy of 10^{-10} and in some cases below 10^{-15}, and the strengths of atomic transitions, which are rarely measured with a precision below 0.1%. Therefore, the polarizabilities of most atomic species are not predicted to better than a few percent from spectroscopic data [86].

The dynamic polarizability can also be determined from the mechanical effect of light on atoms. For example, the polarizability of rubidium at a wavelength of 1064 nm can be deduced by looking at how the atoms velocity is changed while passing through the electric field of a standing wave laser [87]. Several groups have used a Ramsey interferometer to measure the acceleration or deceleration due to near resonant light interacting with the atoms in one of the paths of the interferometer. In this way, the polarizability was determined with a precision on the order of a percent, limited by the uncertainty of the laser intensity *in situ*.

When it comes to polarizabilities, there are several interesting cases that can be distinguished. The first is at an electronic transition of the atom, which is characterised by an increase towards (positive and negative) infinite polarizability at both sides of an infinitely steep zero-crossing of the polarizability on the wavelength-scale. This is not surprising, as an atom will react extremely strongly to a resonant photon. The second case is a so-called magic wavelength, at which the polarizabilities of the two levels of a transition are identical [88]. This means the differential polarizability goes to 0, resulting in a magic wavelength transition that is insensitive to the AC-Stark shift, as both levels shift equally.

A third case occurs when the polariziblity of a given electronic state in an atom, at a specific wavelength between two transitions, goes to zero [89, 90]. This point is called a tune-out wavelength. Tune out wavelengths of He*[91], Li [92, 93], K [94, 95], Rb[96, 97], Dy[98] and NaK[99] have been measured with (sub)ppm accuracy using various techniques, including interferometry and Kapitza-Dirac diffraction, allowing ratios of linestrengths to be determined to sub-percent level. Besides serving accurate determination of atomic parameters, tune out wavelengths are very useful for state, or species, selective manipulation which has applications in quantum computing with neutral atoms [100, 101] and interferometry [102]. Importantly, a comparison between the theoretical and experimental values of certain He* tune-out wavelengths can serve as a test of quantum electrodynamics (QED) [91, 103–105].

1.5 This thesis

This thesis describes the setup that was built to make He* BEC's and perform Bloch oscillations in an optical lattice. This work is divided into 5 chapters, the first of which you have just reached the end of.

Chapter 2 describes the experimental setup that was built, up to the point of the magneto-optical trap (MOT). Details are given on how metastable atoms are generated, slowed down and ultimately trapped in the MOT.

Chapter 3 deals with the cooling of helium atoms, once they are in the MOT. Several trapping and cooling stages are described, as well as the needed equipment. These stages result in an ultracold sample of helium atoms with a temperature of several hundreds of nK.

Chapter 4 shows the optical system that is used to create an optical dipole trap, which is used for the creation of a BEC. The different methods for detecting our ultracold atoms are described as well.

Chapter 5 is dedicated to describing Bloch Oscillations, which involves loading He* atoms into an optical lattice and inducing an acceleration. Here, we also compare our detection methods and demonstrate the high signal-to-noise that can be obtained using an MCP detector for long-term observation of Bloch oscillations. The results establish He* as a promising system for future precision measurements with atom-interferometry, such as the determination of the fine-structure constant α and a proposed next-generation determination of tune-out wavelengths of He* as a precise test of quantum-electrodynamic calculations.

Chapter 6 starts with a demonstration of a novel technique for measuring the polarizability of atoms by measuring deviations of the Bloch oscillation frequency in a vertical optical lattice when a perpendicular laserbeam is introduced. Next, some crucial building blocks for matter-wave interferometry are demonstrated. Finally, some preliminary interferometric signals are shown.

CHAPTER 2

Slowing (a beam of) He* atoms

SINCE Einstein discovered the quantised nature of light, we know that light can be described both as an electromagnetic wave with frequency ν, and as a beam of photons with energy $E = h\nu$ and momentum $p = h\nu/c$. This fundamental insight offers opportunities towards a deeper understanding of the inner workings of atoms, for example by performing spectroscopy. By measuring the wavelengths of the light that are absorbed or emitted by an atom, information about its inner structure can be extracted.

Next to directly probing atoms with light, the concept of photons opens up a whole realm of ingenious and sophisticated techniques that can be used to manipulate and control atomic motion and their internal states. When an atom is subjected to a beam of photons, absorption and re-emission of photons can occur, provided that the frequency matches a resonance in the atom. Due to conservation laws, the absorption of a photon will result in a momentum change of the atom, equal to the momentum of the absorbed photon. If the atom is subjected to a continuous stream of photons, it will result in an effective force on the atom[1]. This provides us with a way to manipulate (and reduce) the velocity of atoms, which can greatly enhance the precision of spectroscopy experiments when for example, the Doppler shift due to atomic motion is

[1] This is recognised already in the early 1600s, when Kepler observed the tails of comets point away from the sun [106], which was explained in 1865 when Maxwell first published the theory that light has momentum and can exert pressure on objects [107].

significantly affecting a measurement.

Around 1980, when lasercooling of atoms began to be investigated thoroughly, pioneers like Chu, Phillips, Cohen-Tannoudji, Ketterle, Metcalf, Wineland and many others paved the way with the invention of techniques still used today. Their research on optical molasses, sub-Doppler cooling, Zeeman slowing and Magneto-optical trapping are still extremely relevant in modern-day physics, and indeed for this research project [108–111].

This chapter first deals with the technical aspects of the atomic beam line and the vacuum system, followed by a description of the techniques used to generate a beam of He* atoms, collimate and slow down the beam and eventually trap the atoms in a magneto optical trap.

2.1 Atomic beam line

In order to use He* in an experiment with a duration on the order of a few seconds, a decent vacuum system is needed, otherwise background gas collisions will cause the He* to decay back to the ground state and be lost from any of the slowing and trapping stages. To minimize this effect, the pressure in the various sections of the experiment should be as low as possible. The vacuum system is schematically shown in Fig. 2.1. Special effort is put into the vacuum of the main chamber, where the atoms remain most of the experimental cycle, necessitating an ultra-high vacuum (UHV). The needed level of vacuum is dependent on the mean free path (MFP) of the helium atoms [112]

$$\lambda_{MFP} = \frac{k_{\mathrm{B}}T}{P}\frac{1}{\sigma\sqrt{1+\frac{m_{\mathrm{He}}}{m_{\mathrm{bg}}}}}, \tag{2.1}$$

with the Boltzmann constant k_{B}, temperature T, pressure P, the respective He*- and background particle masses and collision cross section σ, which is approximated as $\pi(r_{\mathrm{He}} + r_{\mathrm{H_2}})^2$, where r_{He} and r_{bg} are the

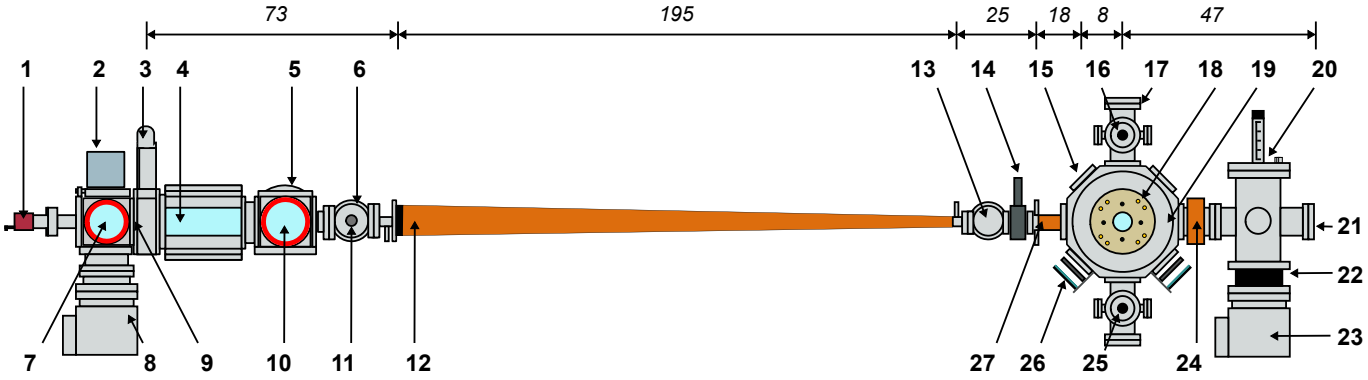

1	Handle for moving He* source
2	Reservoir for liquid nitrogen
3	Manual vacuum valve
4	Collimation section
5	'Chopper' turbopump
6	'FC' turbopump
7	He* Source chamber
8	'Source' turbopump
9	Skimmer position (1 mm ∅)
10	Chopper chamber
11	Faraday cup detector
12	Zeeman slower part 1
13	'ZS chamber' turbopump
14	Pneumatic valve
15	MOT entry window
16	Ion MCP (Ionisation gauge on other side)
17	Vertical lattice in/out window
18	Magnetic trap coil holder
19	Re-entrant flange
20	CEM detector (retractable arm)
21	ITO window/ZS beam entry
22	Vibration dampener
23	'Main' turbopump
24	ZS compensation coil
25	He* MCP
26	MOT $\frac{\lambda}{4}$ + mirror
27	Zeeman slower part 2

Figure 2.1 – *Schematic drawing of the vacuum setup and its components. The indicated lengths in centimeter are, from left to right, skimmer - ZS 1 start - ZS 1 end - ZS chamber - ZS 2 start - ZS 2 end - MOT center - ITO window*

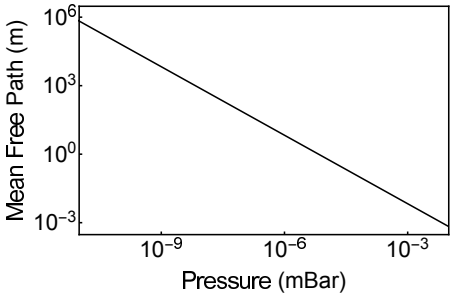

Figure 2.2 – *Mean free path λ_{MFP} of a helium atom in a vacuum system at room temperature as a fuction of the partial pressure of H_2 (this is the most abundant molecule after pumping down). The atoms require over 3 meters of unhindered travel length between source and main chamber [113, 114].*

van der Waals radii of the respective particles. Since the most abundant particle species in the vacuum after pumping down the setup is H_2, Fig. 2.2 was calculated with the assumption that H_2 is the only background gas present. This approximation is justified by the data in Fig. 2.3 which shows the abundance of several molecular gasses in the vacuum chamber. Fig. 2.2 shows the relation between the mean free path of a helium atom in an environment of background particles and the pressure of that background. The distance the atoms need to travel from the source to the main chamber adds up to more than 3 meters, which means that the pressure must remain well below $\sim 1.5 \cdot 10^{-6}$ mbar.

The need for an ultra high vacuum in the main chamber necessitates a large pressure-gradient along the beamline. The different pressures are given in Table 2.1 and are facilitated by a series of turbopumps and differential pumping schemes. The skimmer between the source chamber and collimation section allows for a pressure drop of 2 orders of magnitude.

A 10 cm tube with a diameter of 10 mm separates the 'Chopper' chamber from the 'FC' chamber, which contains a HiPace 80 turbopump and Faraday cup. The tube allows for differential pumping and allows for an order of magnitude of pressure difference between the two stages. The Zeeman slower itself is in essence also a large differential pumping tube, allowing for another order of magnitude pressure decrease.

The pressure in the various sections is monitored using Pfeiffer cold cath-

ode gauges. These can measure pressures between 10^{-2} mbar and 10^{-7} mbar. The main chamber is equipped with a Granville Phillips Ionisation Gauge that can measure pressures from the $10^{-6}-$ to $\sim 10^{-11}$ mbar regime. The pressures in the various sections are given in Table 2.1 for various parts of the setup that is schematically shown in Fig. 2.1.

	Pressure (mbar)	
	Source off	Source on
Source chamber	$3.0 \cdot 10^{-7}$	$5.0 \cdot 10^{-5}$
Collimation section	$4.0 \cdot 10^{-7}$	$3.0 \cdot 10^{-7}$
ZS intermediate	$1.0 \cdot 10^{-9}$	$1.0 \cdot 10^{-9}$
Main chamber	$4.7 \cdot 10^{-11}$	$7.3 \cdot 10^{-11}$

Table 2.1 – *Overview of typical pressures in the setup with the He^* source turned off and on*

A residual gas analyser (RGA200, Stanford Research Systems)[2] was used to study the composition of the gasses left in the UHV chamber after baking. Fig. 2.3 shows a measurement up to atomic mass 65, with the ionisation gauge indicating a maximal partial pressure of $\sim 5 \cdot 10^{-10}$ mbar of H_2 gas. The peak at 28 represents N_2 and CO, the peak at 44 is caused by CO_2. Their partial pressures are quite low and not considered problematic.

An interesting feature is the peak at 19 atomic units, indicating the presence of Fluoride. This later turned out to be caused by a viton O-ring that was used to seal the ITO window (instead of a copper seal) and was accidentally left in the UHV part of the system. This proved not to be a good idea and cost about a year of trying to get the vacuum to stay at UHV pressure, because the viton seal did not seal the chamber at the 10^{-11} mbar level. After a baking procedure, which lasts up to 3 weeks and involves wrapping the entire setup in heating elements and aluminium foil, the pressure would decrease to a minimum of low 10^{-10}

[2]We are very grateful to Dr. M.D. Hoogerland for shipping this equipment all the way from Auckland, New Zealand to Amsterdam for us to use.

mbar level, and slowly rise afterwards over the course of a few weeks to the 10^{-9} mbar level.

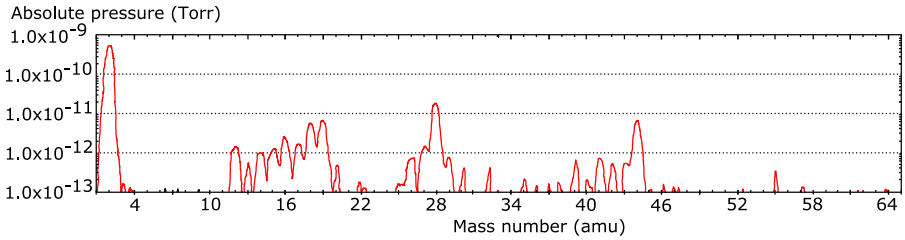

Figure 2.3 – *RGA trace of the main chamber, shortly after a baking procedure, with absolute partial pressure on the y-axis and atomic mass on the x-axis.*

The need for a decent vacuum is illustrated clearly in Fig. 3.10, which shows the lifetime of the atomic sample in the magnetic trap (see Sec. 3.1).

2.2 He* source

To provide a beam of He*, a source based on the design of Fahey et al. [115, 116] was further developed in Amsterdam [117]. Fig. 2.4 shows a schematic view of the discharge source and its components. To create a beam of He* atoms, a voltage of 2.5 kV is applied to a tantalum needle inside a quartz tube. A set of resistors and inductors are connected in series in between the HV-needle and the HV-power supply, in a case which we have dubbed 'the magic box[3]'. The most stable operation of this particular discharge at 10 mA current is found to occur at a resistance of 125 kΩ and an inductance of 2.2 mH.

Helium gas is fed from the back of the tube and flows along the needle, creating a plasma in which helium is excited to many states, including the metastable 2^3S state. Higher states are short-lived and decay back to the ground- or 2^3S state. The products of the discharge then exit

[3] We have several operational sources in our lab, all based on a similar template, yet all of them are unique enough to require a different combination of resistors and inductors for stable operation.

through a boron-nitride nozzle (⌀ 0.25 mm). This material is used because of its good heat conductivity and low electrical conductivity. The nozzle is set inside a copper block, which is cooled by a flow of liquid nitrogen.

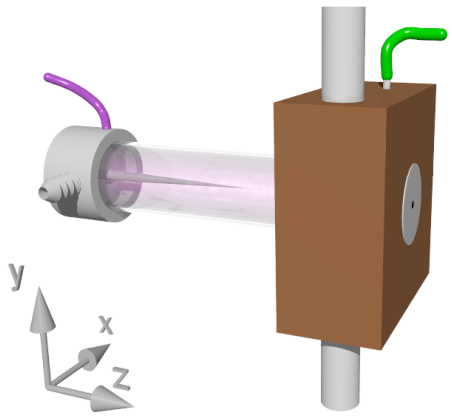

Figure 2.4 – *Schematic view of the He* source. On the left, the helium gas inlet (protruding from the cylinder) and HV-carrying wire (purple) are connected to the tantalum needle inside a quartz tube. The plasma discharge emits atoms towards the nozzle drilled into the boron-nitride cylinder, that is mounted in a copper block and cooled by liquid nitrogen that flows through copper block via bellow. The thermocouple (green) allows temperature monitoring.*

A thermocouple is embedded for temperature monitoring. A skimmer with a radius of 1 mm separates the source chamber from the collimation section. The system shown in Fig. 2.4 is mounted on a retractable arm that makes positioning on the z-axis possible, to move relative to the skimmer. The system can be moved in the x- and y direction by adjusting the flange, sliding on an o-ring on the source chamber, which stays attached to the chamber due to the vacuum pressure.

2.2.1 Time of flight measurements

To analyse the operation of the He* source, TOF measurements were performed using a Channel electron multiplier (CEM). In order to measure the velocity profile of the atomic beam, a chopper was installed in

the third vacuum chamber, which is referred to as 'Chopper chamber' in Fig. 2.1. The chopper consists of a thin plate with a 1 mm slit, rotating at ∼110 Hz, chopping the continuous beam from the source up into packets of atoms, before the atoms enter the Zeeman slower. The detector at the other end will be exposed to a flash of light from the source, followed by a packet of atoms. With the known distance from chopper to detector and by triggering the oscilloscope on the 'light-peak', a velocity profile can be retrieved from the CEM measurements. The chopper was only present during the TOF measurements and was afterwards replaced by an in-vacuum shutter.

CEM detector

The CEM detector is designed to react to impacting high energy particles, charged particles, x-rays and ultraviolet radiation. The inside surface of the CEM is coated with black lead glass. When a potential is applied between the funnel and output end of the CEM, the inside surface forms a continuous electron multiplying surface that has a gain up to $\sim 10^8$. The CEM has a small entrance funnel of 2 mm by 10 mm and the output is amplified by a preamplifier PAD06 (Dr. Sjuts Optotechnik GmbH).

There are two modes of operation. In 'negative mode', a large negative potential is applied to the front of the CEM and a ground potential at the back, pushing the cascading electrons towards the anode and making direct observation of the atomic beam possible. However, this mode blocks the laser beam that is needed to slow down the atoms. To circumvent this issue, in 'positive mode' the CEM faces the window through which the laser light enters the vacuumsetup and is retracted upwards, so it does not block the atomic beam or the Zeeman-laser beam. The window is coated with a Indium Titanium Oxide (ITO) layer, which has a high transmittance in the visible regime. The internal energy of the He* atoms is more than sufficient to cause release of electrons from the ITO surface, which can then be detected by tilting the CEM such that the entrance funnel faces the ITO window.

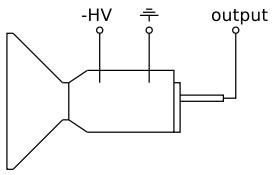

Figure 2.5 – *Schematic diagram of the negative mode of operation of the CEM. The -HV denotes the negative high voltage of about -2500 V, the back potential plate is grounded. The output is connected to an oscilloscope though the PAD06 amplifier/discriminator.*

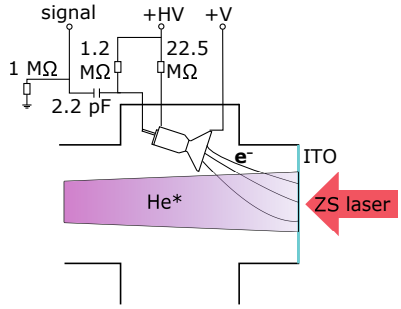

Figure 2.6 – *Schematic diagram of the positive mode of operation of the CEM. The +HV denotes the positive high voltage of ∼2600 V, the +V denotes a +100 V potential. The anode is connected via a capacitor because the back of the CEM is at high voltage.*

2.2.2 Source behaviour

The output intensity and velocity distribution of the beam strongly depend on the conditions inside the source. The temperature of the boron-nitride, the helium gas pressure, the applied voltage and current need to be tuned carefully to achieve a stable discharge. According to a temperature gauge mounted on the source, the LN2 cooling reaches approximately -160°C in steady-state operation. The cooling reduces the velocity distribution of the atomic beam by a factor of 2 [118]. The current that the source draws can be modified by changing a set of resistors that is in 'the magic box'; the resulting behaviour is shown in Fig. 2.7.

Tuning the current mostly determines the mean velocity of the atomic beam, which is an important parameter for the amount of atoms which end up below the capture velocity of the Zeeman slower (a little over 1000 m/s). The atoms with a higher velocity are not slowed down, which

is a bit of a nuisance because they can collide with the slowed atoms and cause losses in the MOT.

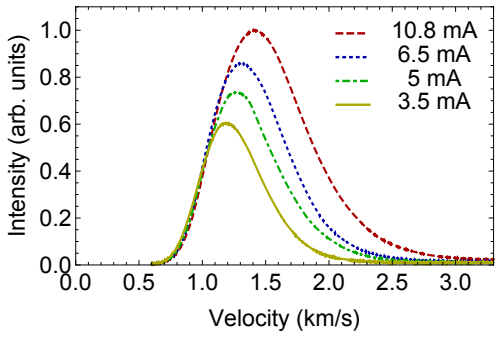

Figure 2.7 – *Intensity profile of the atomic beam as a function of the atoms' velocity, when varying the current through the source. The gas pressure in these measurements was $21{\cdot}10^{-5}$ mbar.*

For stable operation at a certain voltage and current, the helium gas pressure is also important. The behaviour of the source output versus pressure is shown in Fig. 2.8. To ensure a stable daily operation of the source, a pressure of $5{\cdot}10^{-5}$ mbar at 10 mA is chosen. Higher pressures are minimally beneficial for the amount of trappable atoms and are detrimental to the turbo-pump that maintains the pressure in the source chamber. Higher currents were found to be difficult to achieve in combination with a stable plasma-discharge.

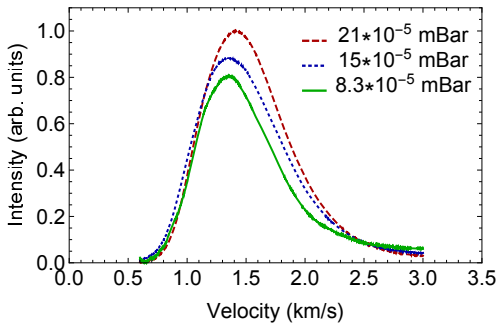

Figure 2.8 – *Intensity profile of the atomic beam as a function of the atoms' velocity, at various helium gas pressures in the source. In these measurements, the current drawn by the source was 10.8 mA.*

2.3 Zeeman slower

In 1982, Phillips and Metcalf came up with a scheme to continuously slow down atoms, using the Zeeman effect [119] (for his contributions to laser cooling, Phillips shared in the 1997 Nobel Prize with Cohen-Tannoudji and Chu). They used a magnetic field to compensate for the Doppler shift that a moving atom experiences, thereby keeping the atomic transition on resonance with a counter-propagating laser-beam, allowing continuous deceleration of the atoms to take place.

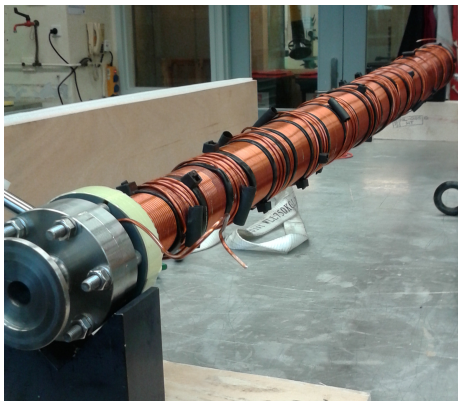

Figure 2.9 – *Picture of the first part of the Zeeman slower, which is made of ∼3.1 km of 2 mm diameter copper wire. The black tie-wraps prevent layer endings from unwinding. Every other solenoid ends in an outspiralling manner to make the B-field transition between the layers less abrupt.*

Manipulating atoms using resonant laser light is based on absorption and re-emission of photons. Incoming photons are absorbed, transferring their momentum onto the atoms. Since the re-emission process has a random orientation, the re-emission kicks will average out and the net force will be in the direction of the laser beam. This is called the scattering force [120] and it is equal to

$$F_{scat} = \hbar k \frac{\Gamma}{2} \frac{I/I_{sat}}{1 + I/I_{sat} + 4\delta^2/\Gamma^2}, \tag{2.2}$$

with wavenumber $k = 2\pi/\lambda$, with parameters for the He* 2^3S_1 - 2^3P_2 transition: $\lambda = 1083.3$ nm, natural line width $\Gamma = 2\pi{\cdot}1.6$ MHz, sat-

uration intensity I_{sat}=0.16 mW/cm^2, used laser intensity I and the difference δ between the laser frequency and the resonant absorption frequency. A brief explanation of the Zeeman effect is given in section 1.3.3. A description of the setup to generate the laserlight that is used to run the Zeeman slower is given in Sec. 3.5.2. Here, specific design-considerations and results of the Zeeman slower are given.[4]

2.3.1 Zeeman effect for slowing He* atoms

In metastable helium, which has spin *S=1* and orbital angular momentum *L=0*, a magnetic field splits the energy levels due to the coupling of the total angular momentum J to the magnetic field. The first order Zeeman shift equals

$$\Delta\omega_{Zeeman} = \frac{g\, m_J \mu_B\, B}{\hbar}, \tag{2.3}$$

where m_J denotes the magnetic sublevel of the state, with J as the total angular momentum of the state, the Bohr magneton μ_B is equal to $(e\,\hbar)/(2\,m_e)$. g is the Landé g-factor, equal to +2 for the 2^3S_1 state and +1.5 for the 2^3P_2 state. Since the resonant cooling transition transfers electrons from an $m_J = 1$ to an $m_J = 2$ state, the driven transition is a closed cycle and has an effective differential value of $\Delta g \cdot \Delta m_J = 1$, making the effective shift of the energy level equal to approximately 1.4 MHz/Gauss.

In Fig. 2.10, the 2^3S_1, 2^3P_1 and 2^3P_2 magnetic sublevels are shown as a function of the magnetic field strength. To slow down atoms, we drive the closed 2^3S_1 m_J=1 to 2^3P_2 m_J=2 transition, shown with the black arrow.

As shown in Fig. 2.10, a crossing of the 2^3P_1 m_J=0 and the 2^3P_2 m_J=2 states occurs at ∼540 Gauss. At this crossing, a loss mechanism for the slowing process occurs; atoms could unintentionally become excited to the 2^3P_1 m_J=0 level, from which they could decay to the 2^3S_1 m_J=0

[4]The description of the design and construction of the Zeeman slower is based on the master thesis of the author [121].

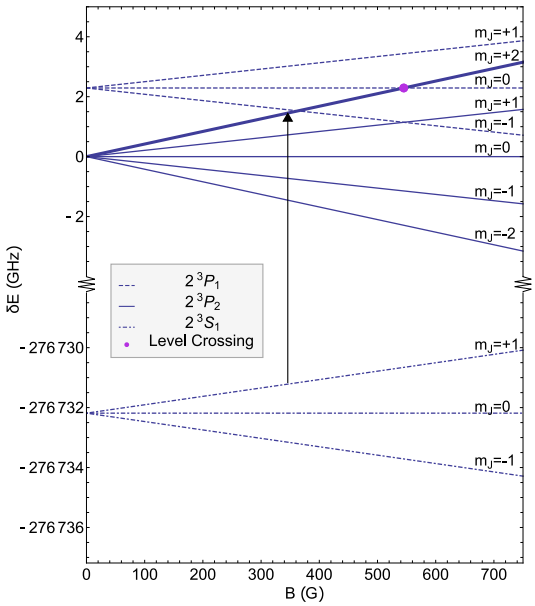

Figure 2.10 – *Energies of the 2^3P_1, 2^3P_2 and 2^3S_1 Zeeman-splitted levels, relative to the 2^3P_2 m_J=0 level. The arrow indicates the 1083.3 nm cooling transition. The transition effectively shifts with 1.4 MHz/Gauss. The level crossing (indicated by the purple dot) marks the value of the B-field where the light can drive transitions to the 2^3P_1 $m_J = 0$ state.*

level. Once in that state, an atom would no longer take part in the closed transition cycle. The maximum possible B-field for our slower is thus limited to 540 Gauss.

The other crossings that are shown in Fig. 2.10 are the 2^3P$_2$ m_J=1 and m_J=2 crossings with the 2^3P$_1$ m_J=−1 state. These do not cause such a loss process, since the transitions from the 2^3S$_1$ m_J=+1 level to an m_J=−1 level are forbidden by the $\Delta m_j = 0, \pm 1$ selection rule.

2.3.2 Zeeman slower magnetic field profile

In the MOT, the atoms are ideally trapped around $\|B\|$=0. Since the Zeeman-slower beam has to pass through the MOT volume, the laser-light used to slow down the He* beam is detuned from resonance by $\Delta = -2\pi \cdot 250$ MHz to minimize its effect on the atoms trapped in the MOT. From this follows the resonance condition

$$\delta = \Delta + (\omega - \omega_0) + kv - \delta\omega_{Zeeman}, \tag{2.4}$$

where δ is the resulting detuning from resonance, ω is the laser frequency in the lab frame, ω_0 is the transition frequency in the atoms rest frame and kv is the resulting shift from the Doppler effect. Solving for δ=0, we obtain a function for the desired B-field

$$B(z) = \frac{\hbar\Delta}{\mu_B} + \frac{\hbar k\sqrt{2\,a\,z + {v_0}^2}}{\mu_B}, \tag{2.5}$$

where a is the induced acceleration, z is the position along the slowing axis and v_0 is the maximum capture velocity of the Zeeman slower. Given the previously mentioned constraints on the maximum B-field, the minimum B-field has to be -140 G, to arrive at a final velocity of approximately 50 m/s. Combined with -250 MHz detuned 1083.3 nm light, a capture velocity of ∼1090 m/s is possible. The velocity at B=0 then becomes 270 m/s, which necessitates the Zeeman-slower to be divided into two pieces, the second part ending up at a negative B-field value, as shown in Fig. 2.11.

For continuous slowing of the atomic beam, atoms need to adiabatically follow the field profile while their velocity is reduced through the absorption of photons. To prevent loss of atoms through gradients in the magnetic field that are too steep to follow, an adiabatic condition can be formulated. [122].

Effectively, the derivative of the magnetic field should not exceed a certain value, otherwise the induced Zeeman shift will no longer be on resonance. This could happen at the discrete field steps where the solenoids that form the Zeeman slower start or finish, i.e., at the transition of the different layers.

From Eq. 2.2 at $\delta = 0$ follows the maximally achievable acceleration

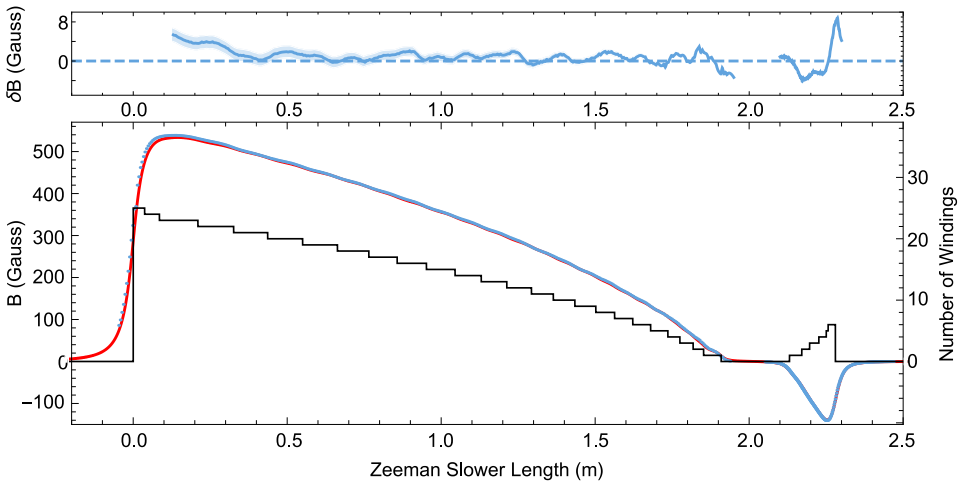

Figure 2.11 – *The magnetic field plotted as a function of the length of the Zeeman slower. In red, the model based on the design of the Zeeman slower is displayed. The measured magnetic field produced by the Zeeman slower is shown in blue. The points were measured using a Hall probe at half-centimeter intervals. The black line is a schematic view of the shape of the slower (see right vertical axis). During the measuremnt, the current were set to 3.96A in ZS part 1 and 3.03A in ZS part 2. The difference between the model and the measurement is shown above, the shaded area shows the Hall Probe uncertainty of 0.25%.*

$$a_{max} = \frac{\hbar\, k\, \Gamma}{2\, m_{He}} \frac{I/I_{sat}}{1 + I/I_{sat}}. \tag{2.6}$$

We can also calculate the acceleration that is induced in the Zeeman slower, by assuming we have the field that is defined by Eq. 2.5,

$$a_{res}(z) = \frac{\mu_B}{\hbar^2 k^2}(\hbar\,\Delta - \mu_B\, B(z)) \frac{\delta B(z)}{\delta z}. \tag{2.7}$$

The actual acceleration may not exceed the maximum achievable acceleration, so the adiabatic condition reads

$$a_{res} < a_{max}. \tag{2.8}$$

The counterpropagating laser does not only slow down the atoms. Due to the random nature of re-emission, the beam will also heat up and expand in the radial direction, so the beam diameter will be larger near the end of the slower. To prevent atoms from hitting the walls and decaying from the metastable state, the inner vacuum tube must have a diameter that is as large as possible and the length should be as short as possible.

The length of the deceleration section is 2.13 m in total, which, assuming constant deceleration, leads to atoms spending approximately 2 ms being slowed down. The number of absorptions needed to reach the desired end velocity is $\sim 12.5 \cdot 10^3$. Since the radiative transition rate for the slowing transition is $102 \cdot 10^5$ Hz, the possible number of transitions is a factor 1.7 higher than required. Because of this, there is a margin in the slowing process. Atoms are not immediately lost from the slowing process if they emit a few unfavourably directed photons, because they can absorb more photons to make up for this in their time spent in the Zeeman slower.

On close inspection of Fig. 2.12 it can be seen in the measurement line that every other peak is less intense than the model. The peaks signify the steeper gradient parts of the field where the stacked solenoids consecutively end. Every other layer ends in an outspiraling manner instead of an abrupt stop, causing the magnetic field gradient to decrease less steep. This was not possible for every step due to construction technicalities, and the effect is visible. The induced deceleration that is calculated from the magnetic field measurement is slightly lower in every second step, as compared to the model. A picture of the outspiraling solenoids can be seen in Fig. 2.9.

Compared to the measurement of the magnetic field in Fig. 2.11, the deviations of the adiabatic condition from the model in Fig. 2.12 seem quite large. The large discrepancies are not a problem for the slowing process, since the calculated deceleration nonetheless adheres to the adiabatic condition, as expected. Small shifts of the position where the magnetic field has a high slope, cause large discrepancies when comparing the data to the model. This is partly due to the layer-density

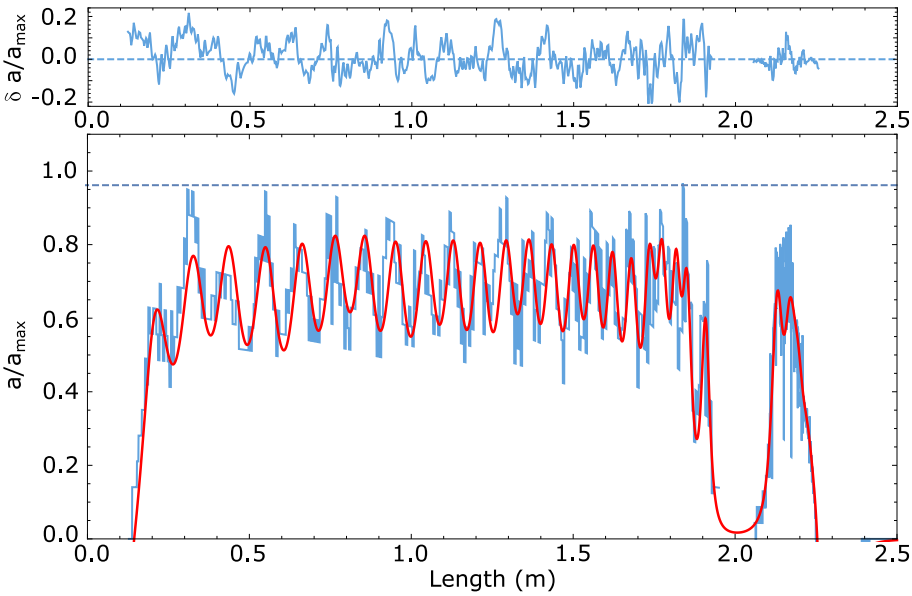

Figure 2.12 – *The acceleration a_{res} along the direction of the slower, relative to a_{max} with infinite laser intensity. The dotted line indicates the adiabatic limit, which the model (red) and the measured field (blue) do not exceed. The deviation from the model is depicted above. The oscillating behaviour of the red curve is explained by the steps in the windings of the coil, while the difference with the model is due small position deviations of these steps compared to the model.*

difference and partly due to the limited resolution of the measurement; the B-field was measured every 5 mm.

By using the CEM in positive mode, the operation of the Zeeman slower can be demonstrated. Fig. 2.13 shows various peaks of increasing arrival time (decreasing velocity), as the current through the slower increases. In this figure, the collimation section was not used. Since the vacuum has to be opened to switch the CEM detector from negative to positive mode, the Zeeman slower was shown to work properly by loading a magneto optical trap.

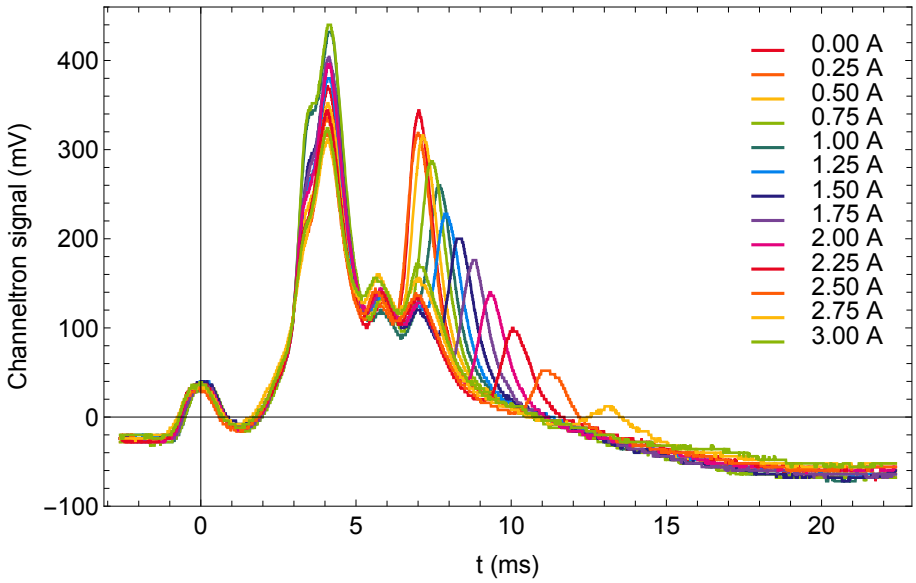

Figure 2.13 – *Arrival time of slowed atoms as the current through the second part of the Zeeman slower increases. The first peak is caused by UV light from the source and is used as t=0. The second peak at 4 ms are non-slowed atoms, the consecutive peaks are succesfully slowed atoms at increasing current through the Zeeman slower.*

2.4 Collimation section

In order to maximise the number of He* atoms reaching the end of the machine, 2D collimation of the atomic beam is implemented in the form of the curved wavefront technique [123]. The method involves the application of two broad, retroreflected, slightly focussed laserbeams, perpendicular to the propagation direction of the atomic beam. The scheme to generate the laserlight that is used to run the collimation section is shown in Sec. 3.5.2.

Since the atomic beam is diverging when it exits the skimmer, the direction of the collimation beams must be matched to be perpendicular to the trajectory of the atoms deviating most from the required direction, in order to provide a maximum deflection of those atoms. As the

atoms change direction due to the radiation pressure, the Doppler shift will change accordingly. By matching the k-vectors of the photons by focussing the laser beam, the atoms are 'guided' along the curvature of the laser beam. This enables focussing of the atomic beam. Since the resonant radiation pressure only works for He* atoms, the number of background atoms in the beam is not increased.

The collimation section consists of a vacuum chamber with four AR-coated windows of 18 x 2.5 cm. The laserbeam is expanded to this size by a large cylindrical telescope that is mounted in front of both entry windows, resulting in a radius of curvature R of ∼6.8m for the beams propagating in the horizontal and vertical direction. Adjustable mirrors on the opposing sides of the chamber retro-reflect these beams, resulting in an increase in signal on the CEM detector of a factor 11 by a combination of the horizontal and vertical collimation, as can be seen in Fig. 2.15. Note that the configuration of the setup was without the second part ZS and main chamber in this measurement.

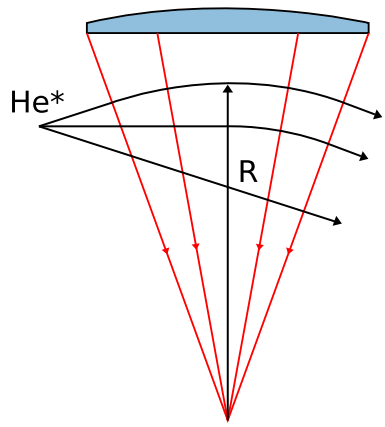

Figure 2.14 – *Schematic view of the effect of a 1D, non retroreflected and focussed laser beam on an atomic beam. The radius of curvature, R, is the distance from the atomic trajectory to the focus of the laserbeam.*

The first peak at 0 ms in Fig. 2.15 shows the light peak from the light coming through the chopper. The double peak structure that follows around 3 ms shows the unslowed atoms. Without the Zeeman slower, this would be a single peak, but the successfully slowed atoms now show up as the signal around 7 ms. A clear increase of this signal is observed when the collimation section is turned on, up to a factor of 11 in surface area under the peaks. The double-peak structure between 1 and 6 ms

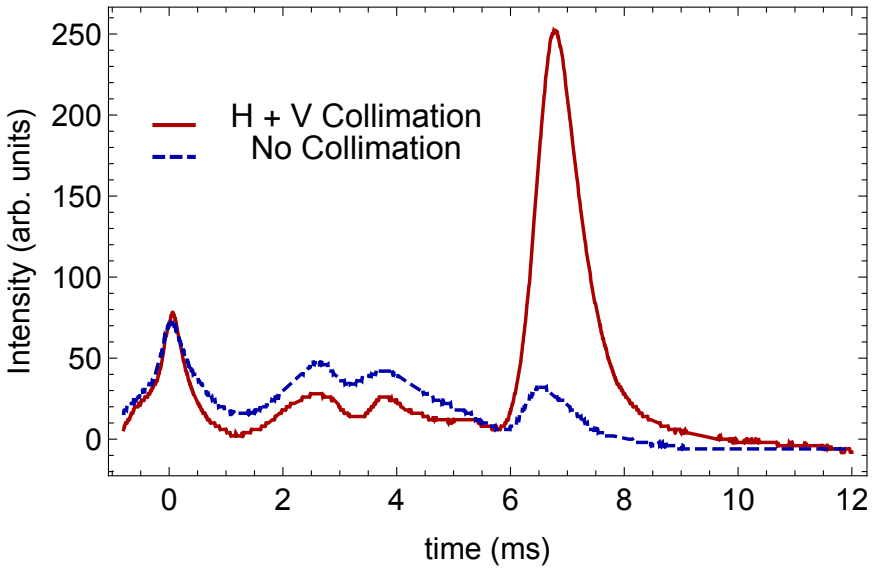

Figure 2.15 – *CEM signal (Positive mode) of a slowed helium beam without (dashed blue line) and with full (solid red) collimation light. Only the first part of the Zeeman slower was used in this measurement. An increase of a factor 11 is achieved in surface area of the horizontal + vertical collimation with respect to the uncollimated beam.*

decreases after turning on of the collimation section because some of the atoms that would not have been captured by the Zeeman slower, are now captured after all. Additionally, some of the atoms may be defocussed by collimation light asymmetry and never reach the detector.

Note that the measured time of flight profiles in Fig. 2.15 looks rather different from the ones presented in Fig. 2.13 due to a different setting of the frequency filter. The profiles in Fig. 2.13 were measured later and more closely resemble the true time of flight distributions.

2.5 Magneto-optical trap

First demonstrated by Raab et al. [124], the magneto-optical trap (MOT) has become a commonplace technique, since it has proven itself to be very robust and applicable as a starting point for many cold-atom experiments.

The optical part of the MOT is formed by directing red-detuned counter-propagating laserbeams onto a cloud of atoms in three dimensions, the atoms can be trapped in the light field. This is called optical molasses and was first demonstrated by Chu in 1985 [125]. The diagonal beams enter the setup from above and are retro-reflected by sets of $\lambda/4$-plates and mirrors. The beams are slightly focussed to compensate for losses caused by passing through the vacuum-windows and optics. These losses are quite small (few % level) since all windows and optics are anti-reflection coated for 1083 nm. The setup that is used to generate the laser light to operate the MOT is shown in Sec. 3.5.2.

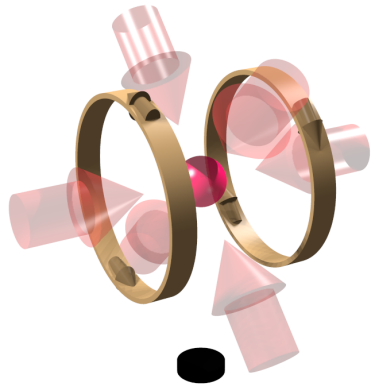

Figure 2.16 – *schematic of the MOT components. The coils for the magnetic field are a part of the Cloverleaf trap, explained in Chapter 3*

Atoms moving away from the center of the overlapped beams will experience a force that is proportional and opposite to their velocity, pushing them back to the center. If we assume $I/I_{sat} \ll 1$, we can treat the beams individually and neglect this term in the denominator in Eq. 2.2, the force an atoms feels from two counter-propagating beams can be written as:

$$F_{molasses} = 4\hbar k \frac{I}{I_{sat}} \frac{kv(2\delta/\Gamma)}{(1+(2\delta/\Gamma)^2)^2}. \tag{2.9}$$

If $\delta < 0$, the beams are red-detuned and this force is opposite to the velocity and acts as a friction force, hence the name; 'optical molasses'. The magnetic part of the MOT is a quadrupole magnetic field, created by two coils in anti-Helmholtz configuration. The field is zero at the center of the trap and increases radially outward. As atoms move out of the center, the transition is Zeeman shifted such that the laser beams become resonant again. The presence of the field of the second part of the Zeeman slower at the center (∼4 G) is compensated by a designated compensation coil that is placed behind the main chamber (also shown in Fig. 2.1).

In the setup, a high light intensity is used, so the simplification in Eq. 2.9 can not be applied. One should also realise that with a magnetic field gradient, the restoring force is not limited to particles in velocity space, but also in real space. Two coils with opposite currents create a magnetic field gradient that adds a position dependent Zeeman shift to the trap. This then shifts the atoms into resonance with the detuned laserbeams when they move too far out of the trap, independent of their velocity. The full restoring force in a MOT is given by

$$F_{MOT} = \hbar k \frac{\Gamma}{2} \frac{I}{I_{sat}} \left(\frac{1}{1 + \frac{4}{\Gamma^2}(\delta - kv - \frac{\mu_B}{\hbar}\frac{\delta B}{\delta x}x)} - \frac{1}{1 + \frac{4}{\Gamma^2}(\delta + kv + \frac{\mu_B}{\hbar}\frac{\delta B}{\delta x}x))} \right). \tag{2.10}$$

A MOT for He* is somewhat different from other typical alkali-metal MOTs in the sense that helium is very sensitive to Penning ionisation and therefore requires low densities in order not to suffer from high collisional losses. This translates into large, 3 cm FWHM MOT beams and a large frequency detuning of 37 MHz, which is roughly 23 linewidths. We operate the diagonally crossing beams at 0.2 mW/cm^2 and the axial MOT beam at 0.4 mW/cm^2, combined with a magnetic field gradient at 43 A of 22 G/cm. This allows us to capture ∼5×10^9 atoms in 5.5 seconds, at a temperature of ∼0.8 mK.

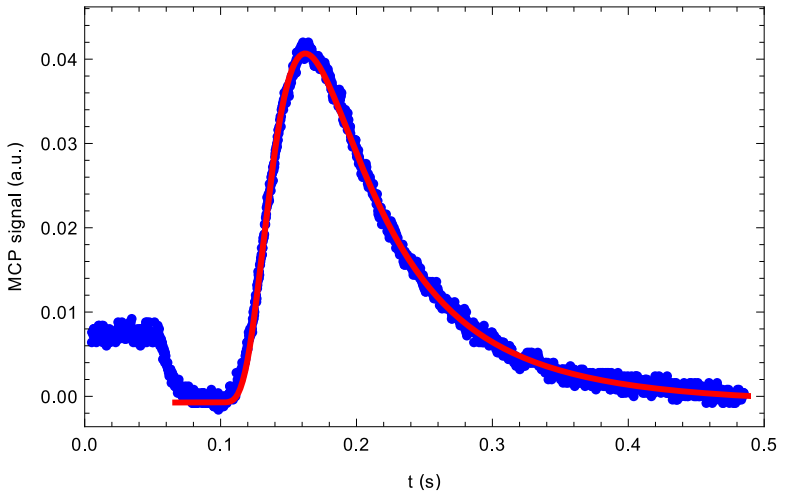

Figure 2.17 – *Time of flight signal of a typical MOT cloud on the MCP detector. The red fit yields at temperature of 0.85 mK and* 3×10^8 *atoms. The constant level before 60 ms is caused by a continuous loss from the steady state MOT loading, which is turned off at t=0. The atoms that were already accelerated towards the detector cause the signal at the start of the trace.*

In our experiments, the He* atoms can be detected by either absorption imaging or time-of-flight flux detection of a cloud of atoms that is released from the trap and falls onto a micro channel plate detector. Both measurement techniques are destructive. The MCP method is convenient for temperature and atom number determinations, but it does not allow for in-situ measurements. Combined with absorption imaging, the atoms' behaviour and properties can be investigated from different perspectives. More details on the detection techniques are given in Sec. 4.3.1 and Sec. 4.3.3.

A typical MOT MCP signal can be seen in Fig. 2.17, where the Maxwell-Boltzmann fit gives us an estimate of the number of atoms and the temperature of the cloud. The MOT performance is determined by the light intensity and strength of the magnetic field, but also by the loading rate,

which is determined by the number of atoms that are successfully slowed down by the Zeeman slower.

As the MOT is being loaded, atoms are continuously accelerated from the trap in all directions due to incomplete capture and deflection by the MOT beams. This causes a continuous background signal on the MCP, as can be seen in the first 50 ms of Fig. 2.17. When the trap is shut off and the loading stops, the atoms that were already moving towards the detector still cause some 50 ms of signal, after which the actual MOT cloud falls on the detector.

2.5.1 Compressed MOT

After the MOT loading stage, we close the in-vacuum shutter placed in front of the Zeeman slower and ramp down the Zeeman slower and compensation coil currents to 0 A in 30 ms, followed by a MOT compression step to improve transfer to the magnetic trap. The compression step consists of a ramp-down of the MOT detuning and power, and a simultaneous ramp-down of the current to 9.5 A, all taking place in 10 ms. The first process cools the cloud by reducing the velocity spread and pushes the atoms towards the center of the trap, compressing the cloud. The decreasing current relaxes the magnetic gradient, which increases the trapping volume. The combination of these steps both cools and compresses the cloud.

Because the magnetic trap has a smaller trap volume than the MOT, this additional compression step results in a better transfer to the magnetic trap. Because the step only takes 10 ms, the increase in losses due to collisions is only minimal compared to the advantageous compressing effect. An example MCP measurement is shown in Fig. 2.18, where the clear increase in signal is caused by the decrease in temperature from 850 μK to 730 μK, because a hotter cloud expands faster and the atoms largely miss the detector. An additional cause for the signal increase is an effective acceleration towards the detector due to a small residual imbalance in the intensity between the incoming and retro-reflected diagonal MOT-beams.

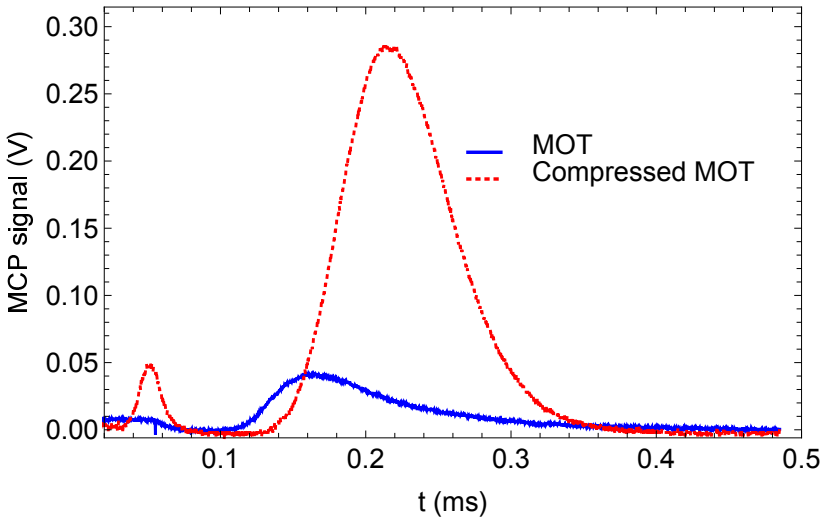

Figure 2.18 – *Comparison of normal MOT and Compressed MOT. The increase in signal is caused by a decrease in temperature from 850 to 730 μK, combined with a slight acceleration towards the detector due to a residual power imbalance in the beams.*

Summary

In this chapter, the basics of the beam line have been explained. We have dealt with the helium plasma discharge, which is used to generate a beam of metastable helium atoms. This beam is 2D-collimated and slowed down with a two-part Zeeman slower, so that the magneto-optical trap can capture about 3×10^8 atoms. After the MOT is completely filled, we compress the atomic cloud in the MOT to further cool the atoms and to better shape the cloud to fit the potential of the next trapping stage, the magnetic trap.

In the magnetic trap, we continue the cooling our sample towards degeneracy with various tricks and techniques, which are the subject of the next chapter.

CHAPTER 3

Trapping He* atoms

This chapter deals with the various trapping stages that are employed to cool He* towards degeneracy [126, 127]. It describes a large portion of the setup and various elements needed to control the light and the atoms. In the previous chapter, the MOT was described. Here, the cooling sequence towards a BEC is continued with the transfer of the atoms to the magnetic trap. First, the magnetic trap is explained and several cooling steps are demonstrated. Next, some general elements of the setup are described, such as the control software and the laser-setup.

3.1 Cloverleaf magnetic trap

3.1.1 Magnetic traps

Trapping atoms using light fields is something one can imagine quite intuitively; by absorbing photons from beams coming from all directions, an atom can be held against gravity and is continuously pushed towards a trap center. The downside of using optical traps is photon heating; by continuously absorbing and re-emitting photons, an atomic sample can never be cooled below the recoil limit of 2 μK, and in practical situations it is hard to cool below the Doppler limit (38.4 μK for helium). As an alternative to light-based traps, magnetic traps can be used to trap neutral atoms that possess a magnetic moment. In the presence of a

magnetic field B, the atom will feel a potential

$$U = \mu_{\mathrm{B}} g_J m_J B, \tag{3.1}$$

where μ_{B}=1.4 MHz/Gauss is the Bohr magneton and $g_J \approx 2.002$ is the Landé factor for the metastable state in ^{4}He*.

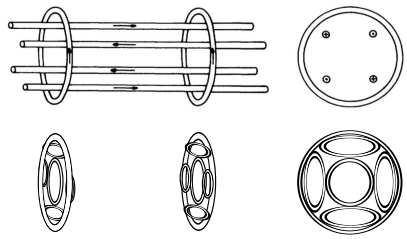

Figure 3.1 – *Drawing of the Ioffe-Pritchard trap taken from [128], with the new configuration below. In our case, the horizontal wires are replaced by cloverleaves and centered in the large axial coils a smaller set of axial coils is added.*

With a well chosen magnetic field configuration, a ^{4}He* sample in the appropriate m=+1 low-field seeking state can be held in the minimum of a magnetic field using a pure magnetic trap (MT) and can then be cooled to quantum degeneracy. The straightforward magnetic trap is an extension of the MOT field: a quadrupole magnetic trap. It consists of a set of anti-Helmholtz coils that creates a magnetic field gradient on the coil axis with a minimum of the absolute field at the center of the coils axis. In the region around the trap center the absolute field is small, leading to a small Zeeman-splitting of the magnetic sublevels, which enhances the probability of a transition to a non-trapped state. This effect is called a Majorana spin-flip transition and it limits the lifetime of a trapped atomic sample significantly. A cloud of metastable helium is particularly sensitive to this effect, since an atom which spin has flipped, can then also undergo Penning ionising collisions and knock another helium atom out of the trap with it. The rate at which the non-adiabatic Majorana spin-flips occur depends on the velocity, leading to a rate that is inversely proportional to the mass of the atom. This means helium atoms that are trapped in a quadrupole trap are severely affected [129].

A different kind of trap, originally designed by the groups of Ioffe [130] and Pritchard [131], circumvents this problem by adding an additional

set of coils within the first set. By letting the same current run through both sets of Helmholtz coils, the B-field value at the center of the trap becomes a design parameter. Moreover, by adding a small current to one of the sets of coils, the center B-field value becomes tunable, while keeping the trap in the center harmonic. The combination of these sets of coils produces a saddle-shaped field and does not provide trapping in the radial direction. To compensate, wires that run in the z-direction are added that create a radial field. This makes the depth and aspect ratio of the trap more readily accessible design parameters than for a quadrupole trap.

The cloverleaf design is based on the original Ioffe-Pritchard trap and was first adapted for a helium BEC machine by Tychkov [132]. A thorough re-design was done for the setup described in this work to allow changes in the size of the re-entrant windows and flanges. The re-entrant flanges are designed in such a way that they resemble 'buckets' that have a window at the bottom, as schematically shown from the side in Fig. 5.2. In this way, the volume of the inside of the vacuum chamber is small, and the coils can be moved very close to the trap center, without having to put them in the vacuum itself. To enhance the optical access, and again mostly to circumvent having to put objects into the vacuum, the four wires that create the radial trapping field in the original design of Ioffe and Pritchard are replaced by eight so called cloverleaf coils. These are also able to create the needed radial field, while conveniently fitting into a box that holds all the coils outside the vacuum [133].

3.1.2 Trap field geometries

Using cylindrical coordinates, the field near the center of the magnetic trap can be approximated by

$$\begin{aligned} B_\rho &= \alpha\rho\sin 2\varphi - \beta z\rho, \\ B_\varphi &= \alpha\rho\cos 2\varphi, \\ B_z &= B_0 + \beta z^2 - \frac{\beta}{2}\rho^2, \end{aligned} \tag{3.2}$$

where α is the radial gradient, β is the axial curvature and B_0 is the magnitude of the magnetic field at the center of the trap [132, 134]. The magnitude of the field is given by

$$|\mathbf{B}| = \sqrt{(\alpha^2 - B_0\beta)\rho^2 + (B_0 + \beta z^2)^2 - 2\alpha\beta z\rho^2 \sin(2\varphi) + \tfrac{1}{4}\beta^2\rho^4}. \quad (3.3)$$

The second-order expansion of Eq. 3.3 yields a harmonic appoximation, which is valid as long as $(|\mathbf{B}| - B_0)/B_0 \ll 1$. The trap center is considered to be harmonic in a region set by B_0/α. Outside this region the potential starts to become linear. The approximation allows Eq. 3.1 to be expressed as

$$U \approx 2\mu_B B_0 + \frac{1}{2}m(\omega_z^2 z^2 + \omega_\rho^2 \rho^2), \quad (3.4)$$

with axial and radial trap frequencies

$$\begin{aligned} \omega_z &= \sqrt{4\mu_B \tfrac{\beta}{m}}, \\ \omega_\rho &= \sqrt{2\mu_B \tfrac{(\alpha^2/B_0) - \beta}{m}}. \end{aligned} \quad (3.5)$$

The trap frequencies can be tuned by changing the axial curvature and radial gradient, which is done by changing the currents in the coils. The large and small axial coils are in series, and designed such that B_0 can be tuned to tens of Gauss, as well as a value close to zero. The current in the cloverleaf coils independently determines the radial gradient, while the axial curvature can be tuned by adding a small current to the small coils. This then enables starting with a shallow axial trapping field, which enhances the transfer from the MOT, after which the trap can be compressed by reducing the added current to the small coils.

3.1.3 Design of the cloverleaf trap

For the experiment, a new magnetic trap was designed, based on the design from [132]. The design constraints were the size of the re-entrant windows, the distance in between the windows of the re-entrant flanges, the need for optical access through the coils and sufficient B-field strength.

A piecewise evaluation of the Biot-Savart law over programmable coil segments was used to optimise the sizes and number of windings in the trap, while keeping the needed currents to acceptable levels (below 200 A). A peek (Polyether ether ketone) coil holder was designed to mount the coils while keeping as much space around them as possible for watercooling purposes. This is much needed as one set of six coils at the peak of its operation dissipates up to 2.1 kW. To cool this away, a stand alone chiller (Lytron - Kodiak RC045) is dedicated to the two sets of coils, supplying one bar of pressure of distilled water at 16 °C (at lower temperatures, condensation will form on the outside of the water pipes).

Figure 3.2 – *Assembly of the coils in the peek box. The cutouts and grooves for water cooling access are clearly visible on the wall of the inner cylinder, as well as in the center of the cloverleaf holders. An o-ring sealed cap (not shown) is placed over the assembly, allowing water cooling all around the coils.*

The cloverleaf trap consists of 12 coils, 6 on each side of the trap center. All coils are wound with 2x3 mm square wire (radial x axial direction) to facilitate easier winding and efficient filling of the limited space. To ensure the coil will retain its shape after winding, the coils were dipped in epoxy and left to harden. The two large axial coils (MOT coils) are made of 25 windings each (5 axial layers by 5 radial windings), with an inner radius of 5.2 cm and a distance of 5.8 cm from the center of the trap. The small axial coils (pinch coils) are 42 windings each (7 axial layers by 6 radial windings), with an inner radius of 2.9 cm and a distance to the center of the trap of 5.8 cm. With a wall thinness of 5 mm, this leaves a 46 mm ∅ access for horizontal optical access through the coil assembly.

The cloverleaves are placed closest to the trap center, since they are smaller and require high current to reach sufficient field strength. Each leaf consists of 16 windings (4 axial layers by 4 radial windings) that are wound around an ellipse with radii of 0.9 cm and 2.8 cm. The leaves are radially placed 4.8 cm from the central axis of the trap and 3.3 cm from the trap center (axially). The cloverleaves are connected to each other such that the current direction flips from leaf to leaf.

3.1.4 Compressing the magnetic trap

The above described coil sets are capable of producing the various magnetic field configurations needed in the experiment, starting with the large axial coils in anti-Helmholtz configuration to produce a quadrupole field for the MOT stage. The magnetic trap stage requires strong trapping fields where, as mentioned before, the trap curvature and B_0 are tunable parameters. The B_0 needs to be high during transfer of the MOT to the MT and during the consecutive 1D Doppler cooling stage, to prevent high atom losses due to the Majorana effect. During the transfer, the curvature of the MT has to be low to better match the shape of the cloud when it is captured from the MOT stage.

The following evaporative cooling stage requires a low and stable B_0. It is reduced to near 0 Gauss to increase the gradient of the trap walls in order to make precise cutting with the RF-knife for evaporative cooling possible. Because fluctuations of B_0 can greatly affect the efficiency and

heating of the sample, as the trap depth is dependent on this parameter, stability is an important concern.

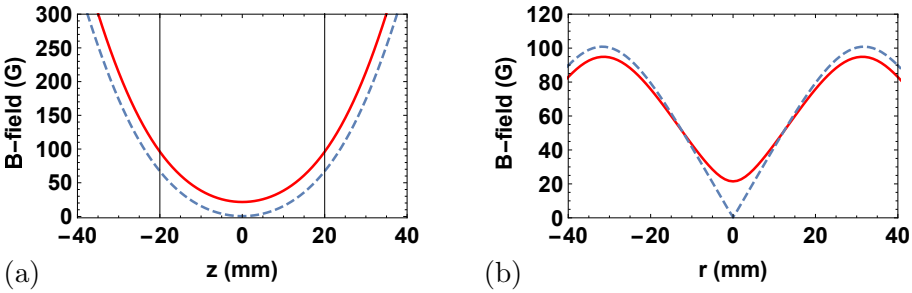

Figure 3.3 – *(a) Magnetic field on the axial direction of the trap coils at r=0. The vertical black solid lines show the edges of the vacuum system at the re-entrant windows. (b) Magnetic field in the radial direction at z=0. For both graphs, the red solid lines show the uncompressed field, the dashed blue lines show the field after compression.*

The circuit used to switch between different trap geometries is drawn in Fig. 3.4. It consists of three current supplies to power the coils and various switches that can open and close different paths for the currents. The main feature is the H-bridge that reverses the direction in one of the MOT coils.

Supply 1 (Delta Elektronika SM30-200) is connected to the MOT coils (and pinch coils in MT mode), and is specified to have a 20 mA rms current ripple. Since in MT mode the two sets of coils are operated in opposite current direction, any current imbalances are largely canceled out. Supply 2 (SM15-400) is connected to the pinch coils through a power diode and is used to control the B_0 offset field by adding an additional current through the pinch coils in MT mode, which linearly changes B_0 with ∼2 G/A. It is operated at 30 A (∼25.4 G) during the MOT-transfer and 1D-Doppler cooling. Before the evaporative cooling, it is ramped down to 17.5 A, which brings the B_0 to ∼2.4 G. Current supply 3 (SM15-200 D) is connected to the 4 cloverleaf coils, which are connected in series and which are supplied with 170 A throughout the MT stage.

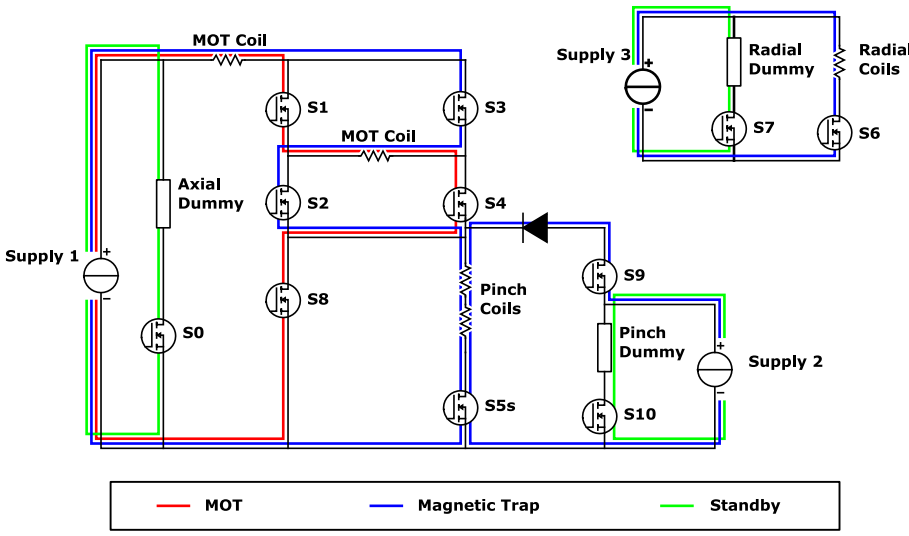

Figure 3.4 – *Electric circuit used to control the currents for the different configurations of the magnetic trap. The colors denote the various modes of operation (see legend).*

The switches S0-S10 consist of sets of parallel MOSFETs (IXFN 340N07). The current supplies for the magnetic coils can be damaged by fast switching of the MOSFETs, as well as a sudden change of load due to the switching. To prevent damaging the supplies, dummy coils were added to the electrical circuit to allow the supplied currents to extinguish externally, instead of inside the supplies themselves. The resistances of the dummy coils are matched to the resistances of the trap coils in each current loop in MT mode. The dummy coils are made of copper wire wound in a tight helical manner and are contained in plastic tubing, connected to an external water cooling system. They are mounted on the floor, underneath the Zeeman slower, over 2 meters away from the main vacuum chamber, to prevent the presence of unwanted magnetic fields in the magnetic and optical traps. The different modes of the operation are as follows:

MOT During this stage, switches S1, S4 and S8 are on, allowing supply one to deliver current to the MOT coils in the anti-Helmholtz direction. S7 and S10 are also on, to connect the other supplies to the corresponding dummy coils.

Magnetic trap loading During this stage, switches S2, S3, S5, S6 and S9 are on, allowing supply 1 to power both the MOT coils and the pinch coils in the same loop. Supply 2 adds 30 A to the pinch coils in order to raise the B_0 to $\sim$ 26 G. Supply 3 delivers a constant 170 A to the cloverleaves.

Magnetic trap compression Here, the variable current delivered by supply 2 is lowered to 17.5 A, reducing B_0 to $\sim$ 1 G.

Standby During this stage, switches S0, S7 and S10 are on, routing all currents through the dummy coils.

3.2 Spin polarisation

As explained in Chapter 2, magnetic fields lift the degeneracy of the metastable 2^3S_1 state. The behaviour of atoms in a magnetic field will now depend on which magnetic substate it is in, as it will seek to minimize the energy in the system. This creates the so-called high-field seeking states ($m_J = -1$) and low-field seeking states ($m_J = +1$). Since the trap has a positive B-field, the $m_J = +1$ atoms will collect at the potential minimum, i.e. the center of the trap, whereas the $m_J = -1$ atoms will be anti-trapped and expelled from the trap.

To capture as many atoms as possible, a spin-polarising step is added during transfer to the magnetic trap, which should roughly increase the trapped number of atoms by a factor of 3. This is achieved by flashing a very weak, circularly polarised 1083 nm beam on the atoms for 3 ms at a detuning of 1.8 MHz, with an intensity of 6 μW/cm^2. The beam intensity is reduced by enlarging the diameter to 7 cm, to avoid photon heating. This is convenient, as this allows us to also use this beam for horizontal imaging at higher powers.

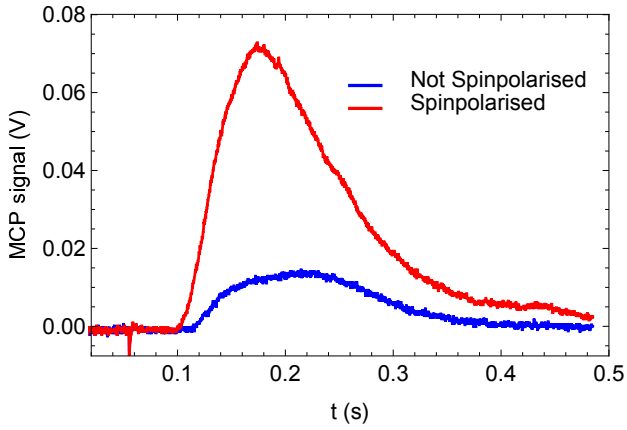

Figure 3.5 – *MCP time-of-flight signal of a spin-polarised cloud and a non-spin-polarised cloud. The fitted temperature of the spin-polarised cloud is 400 μK, and the number of atoms is increased by a factor of 5.*

The spin-polarisation beam optically pumps the $m_J = -1$ atoms to the $m_J = +1$ state. The m=0 atoms can in principle only be pumped to the $m_J = +1$ state with circularly polarised light, but as the windows are slightly birefringent, there is most likely some linearly polarised light present. To minimise this effect, the used $\lambda/4$ plate was rotated to optimise the signal and not to perfect the circular nature of the beam. We observe an increase in signal of about a factor of 5. Note that we attribute this high increase to the high losses in the non-polarised signal, which suffers from Penning losses. Therefore, the increase in signal seems higher than expected.

3.3 1-Dimensional Doppler cooling

After being captured in the magnetic trap, the atoms are cooled further using 1D Doppler cooling. This process consists of absorption and re-emission of photons that are slightly red-detuned with respect to the resonance frequency at the B_0 of the trap. The trapped cloud has a temperature of approximately 500 μK, translating to a thermal velocity of about 1.7 m/s. The circularly polarised cooling beam is directed into the chamber at an angle of $\sim 5°$ from the axial direction of the long magnetic trap axis, through the re-entrant windows. The kick an atom will recieve from the 1D-Doppler light will reduce the atomic velocity by

9.2 cm/s. When the photon is re-emitted, this will happen in a random direction, so that the velocity effectively decreases [135].

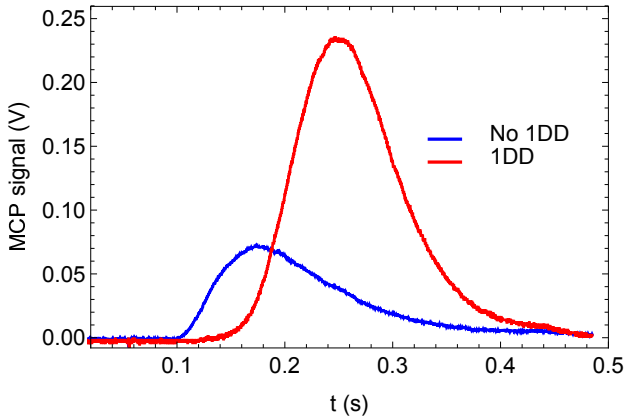

Figure 3.6 – *MCP time-of-flight signal of a cloud cooled by 1D-Doppler light (red) and a non-cooled cloud (blue). The fitted temperatures are 150- and 400 μK, respectively. (fits not shown)*

There are a few crucial requirements for this technique to work. Firstly, the frequency of the light has to be tuned to just below the effective resonance frequency. The empirical optimal value in our case is 2 MHz. Secondly, the power of the laser beam must be very low to avoid heating (we use less than 1 nW/cm^2). Since the power of the beam is very low, it takes some time for the ensemble to scatter sufficient photons to cool down; we use 4.5 seconds for this cooling stage. Lastly, the density of the atomic cloud has to be sufficient to make it opaque to the photons. The re-emitted photon can then be absorbed by other atoms that move towards the photon, now no longer only in the axial direction of the trap.

The frequency change due to one absorption and re-emission is approximately 85 kHz towards the blue, but since the detuning is approximately -2 MHz from resonance, this is negligible and keeps the photon red detuned for the atoms in the trap, allowing further cooling in 3D. The temperature is reduced to approximately 150 μK, or 1 m/s rms velocity, as is inferred in Fig. 3.6.

3.4 Evaporative cooling

After compressing the magnetic trap, the atomic sample is further cooled by using RF-induced evaporative cooling. This cooling step consists of selectively removing the most energetic atoms from the ensemble and allowing the remaining atoms to re-thermalise to a lower temperature. By slowly removing more and more of the hottest atoms of the sample, the cloud cools down to the critical temperature. An often used analogy is a coffee cup in which the hot atoms evaporate from the surface and the coffee slowly cools down.

The removal of the high-energy atoms is realised by inducing spin-flip transitions between trapped and non-trapped states of the metastable helium atom, through the use of an RF-field. The RF-field is applied by sending high-power RF through a small coil near the atoms, mounted on the end of the second part of the Zeeman slower, inside the main experimental chamber, as shown in Fig. 3.7. As is mentioned in Sec. 3.1.1, a neutral atom will feel a potential in the presence of a magnetic field. The associated Zeeman shift between the magnetic substates has a magnitude of $\sim$ 2.8 MHz/Gauss for the m_J =+1 level, which means that at the appropriate RF-frequency ω_{RF}, atoms are removed from the trap when they probe a magnetic field that satisfies

$$\hbar\omega_{RF} \approx 2\mu_B B. \qquad (3.6)$$

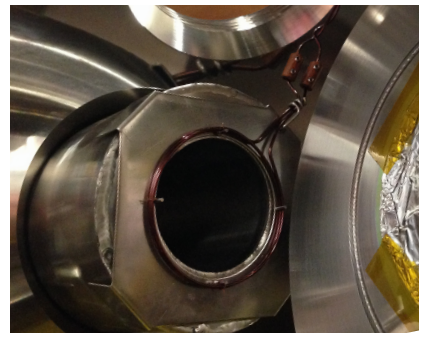

Figure 3.7 – *RF coil inside the vacuumchamber, mounted on the second part of the Zeeman slower which protrudes into the vacuum. On the left, one of the re-entrant windows is visible, with protective foil over the window (photograph taken during the assembly of the setup), and one of the MOT windows can be seen above the Zeeman slower end.*

Since only the most energetic atoms reach the high magnetic field regions of the magnetic trap, choosing an initial RF-frequency that corresponds

to a high B-field value will cut these hot atoms from the sample. This is why this technique is also commonly referred to as an RF-knife. By slowly cutting deeper with the knife, i.e. lowering the RF-frequency, the atomic sample will continuously loose hot atoms and re-thermalise to lower temperatures.

In the optimised experimental sequence, the evaporative cooling step takes 6 seconds, in which the RF frequency sweeps from 78 MHz to 4.1 MHz in an exponential sweep (τ=1.2 sec). The RF is supplied by an AWG (Agilent 33250A, 80 MHz) and amplified to 10 W (by a Mini-circuits LZY-22+), before it it sent to the RF coil. Fig. 3.8 shows the resulting time-of-flight signals on the MCP near the end of the RF-sweep. The peak that emerges at $\sim$260 ms clearly exhibits an inverted parabola shape, a telltale sign of Bose-Einstein condensation. Scanning the RF-frequency down is also a measurement of the B-field value of the bottom of the magnetic trap, which appears at 3.3 MHz, corresponding to a B-field of 2.4 G. A simple model gives a value of 4 G [136].

As Fig. 3.8 shows, the last part of the frequency ramp of the forced evaporative cooling changes the signal drastically. One has to be very careful, because, when cutting to a frequency that is close to the trap bottom, 0.1 MHz can make the difference between a large condensate and no signal at all. Due to small fluctuations of the magnetic field at the center of the trap, the end value of the RF-ramp is chosen such that does not reach all the way to the optimal value for the largest BEC, but to the value that ensures a BEC even if the B-field increases slightly. Furthermore, due to the high sensitivity to small frequency steps of the last stage of the evaporative cooling, the RF-frequency has to be finely tuned in this part of the cycle. For technical reasons we are limited by the inherent 'coarseness' of the RF knife, which is determined by the control voltage steps and the range of the AWG. The issue can be solved by implementing a second AWG with a smaller range (say 20 MHz) and an RF-switch, but we chose to continue the evaporation in the optical dipole trap (which does not have this problem), which is described in Chapter 4.

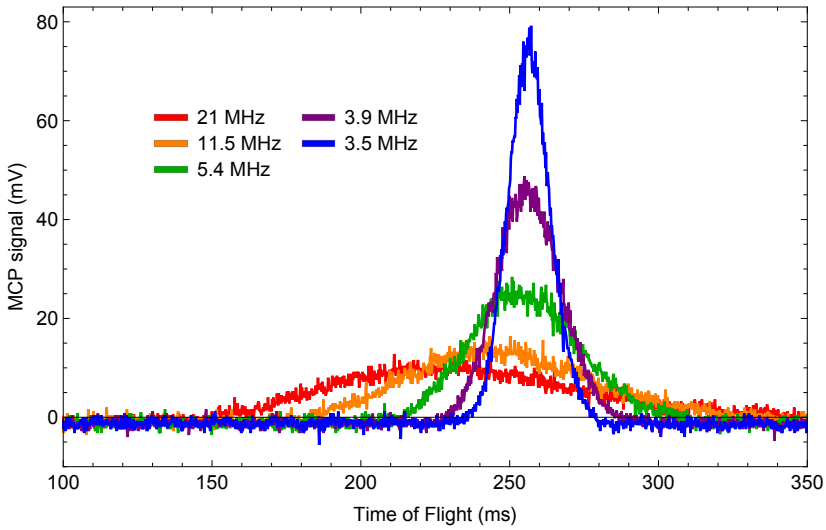

Figure 3.8 – *MCP TOF signal of the atomic sample resulting from various endpoints of the evaporative cooling sweep. The figure clearly shows an increase in signal and change in shape as the RF-frequency is reduced. The final signal (blue) shows the characteristic inverted parabola shape associated with a BEC (Note that these MCP traces are amplified with a different amplifier than the data that is shown in chapter 4, due to improvements made in-between the measurements).*

3.4.1 Characterising the magnetic trap

Besides demonstrating the different cooling stages in the magnetic trap, the behaviour of the trap was checked also by measuring the trap frequencies. These play an important role in the properties of the produced ultracold clouds, as well as in the analysis of the signals with the MCP detector. This is because the trap frequencies determine the radii of the trapped sample, and thereby also influence the chemical potential of the cloud (see Sec. 4.3.1).

To measure the trap frequencies of the MT, a cold sample of atoms is prepared in the trap using evaporative cooling. The atoms are then 'kicked' by briefly (up to 10 ms) flashing on a magnetic offset field coil (5/10 A),

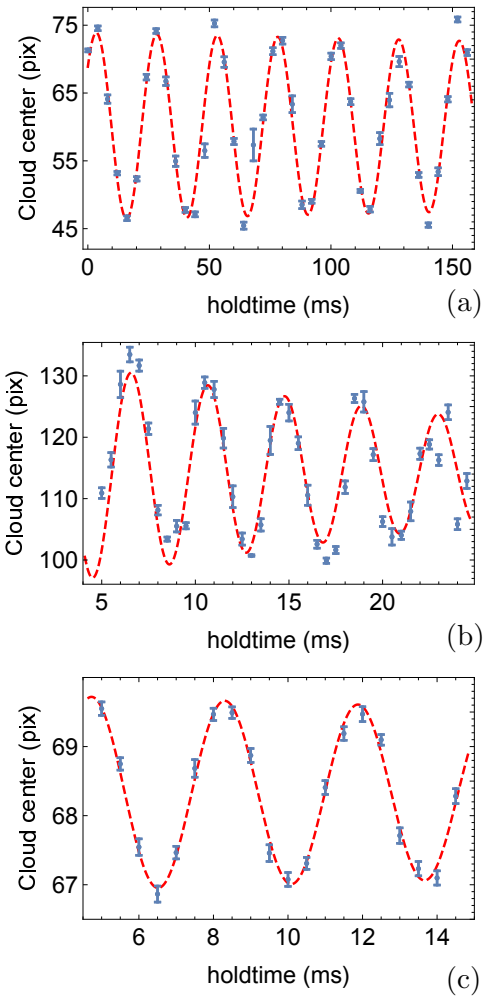

Figure 3.9 – *Magnetic trap trap frequency measurements taken with absorption imaging after pushing the atomic sample out of the trap center with a 10 ms magnetic field pulse, using 5 A for the vertical and axial measurements (through the vertical and axial compensation coils), and 0.5 A for the horizontal measurements (through the ZS compensation coil). The blue datapoints show the fitted center position on the camera, the red dashed lines show a sinusoidal fit with an exponential decay.*
(a) Axial freq. 40±0.2 Hz.
(b) Horiz. freq: 244±2 Hz.
(c) Vert. freq: 280±2 Hz.
The damping in (b) is caused by pushing the sample too hard, forcing the atoms to probe outside the approximately harmonic trap center. For all orientations, one pixel corresponds to 21 μm.

and left to oscillate in the trap. By scanning the turn-off time, the trap frequency can be retrieved from absorption images after some time of flight, or from the MCP signal. By retrieving the center of the cloud from absorption images after 5 ms time of flight, the trap frequencies at the compressed trap setting were measured, as can be seen in Fig. 3.9.

The fitted frequencies are 40 Hz, 280 Hz and 244 Hz in the axial, vertical and horizontal direction, respectively. The noticable damping in

Fig. 3.9b is likely caused by the atoms probing the an-harmonic region away from the trap center. We estimate the radius of the harmonic region to be about 750 μm from the axial gradient of $\sim$10 G/cm^2 (see Sec. 3.1.2). The center of the atomic sample (FWHM of $\sim$12 pixels, or 252 μm) oscillates with an amplitude of more than 15 pixels, or 315 μm. Although it would seem that the sample oscillates within the range where the potential should be harmonic, we have observed in measuring the vertical trap frequency that the damping effect is present with a 10 A magnetic push current, and absent when a 5 A push current is used. Since the coil assembly is symmetric, the horizontal and vertical trap frequencies should be identical and we use 280 Hz as our radial frequency.

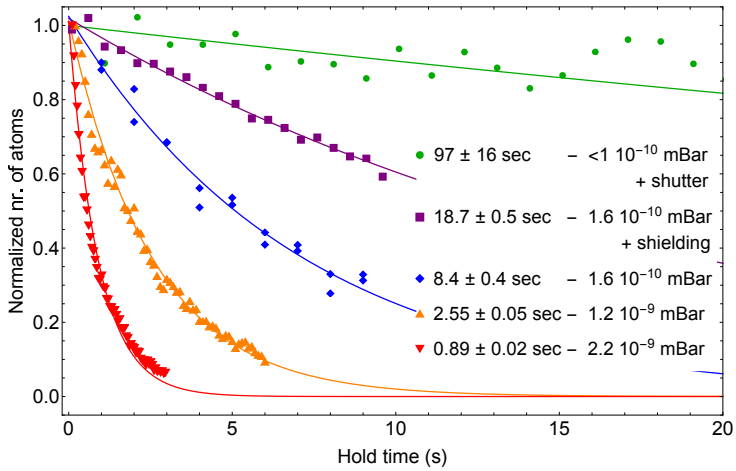

Figure 3.10 – *Lifetime of atomic cloud in the magnetic trap at various pressures and with added shielding to the optical tables. The red upside-down triangles, orange triangles and blue diamonds show lifetime measurements at various pressures. The purple squares show measurements that were performed with shielding added around the setup, to prevent resonant laser light from reaching the atoms in the main chamber. The green circles show measurements after addition of a shutter on the laser table, to completely block the laser light from a large part of the optical setup. (Upper-right shutter in Fig. 3.12.)*

A separate characterisation that is of importance is the lifetime of a

cold sample in the magnetic trap. As our cooling stages take up several seconds, the loss rate from the trap must be low compared to this time. By varying the hold time of the sample in the trap, the lifetime of the trap is tested. Several runs of this experiment are shown in Fig. 3.10. The orange triangles show the decrease of the number of atoms in the trap at a pressure of $2.2{\cdot}10^{-9}$ mBar, and were recorded just after the first baking campaign (which involves wrapping the entire setup in heating tape and aluminum foil and literally baking the hydrogen out of the inside of the walls). The red upside-down triangles show data of one month later, when the pressure had unfortunately risen due to vacuum issues, and the lifetime clearly decreased.

After fixing the vacuum issues and more baking, an order of magnitude was won in pressure, and the lifetime increased to 8.4 seconds (blue diamonds). An important step turned out to be shielding from resonant 1083 nm light. With diligent placement of screens on the laser table and curtains between our setup and the neighbouring helium experiment that is used for Helium spectroscopy [88], a lifetime of about 100 seconds was obtained (green circles).

3.5 Experiment control

In order to reproducibly and reliably create cold clouds and perform measurements that take place on microsecond time scales, accurately timed experimental control is key. The setup is managed by homebuilt software originally designed for the neighbouring helium spectroscopy setup [137].

The control program is based on Python 2.7 and controls a NI analog card (PCIe-6738) with a 32 channel breakout board (SCB-68A) that has a -10 V to +10 V span, programmable at 16-bit depth (roughly 0.4 mV resolution). Next to that, a digital card (PCIe-6536B) with a 32 channel, 3.3 Volt TTL output board (SMB-2163) is used to control a range of shutters, switches and FET's. Once the appropriate experimental parameters are put into the program, a timetable is buffered onto the analog card, which is triggered by the digital card for synchronization.

This triggering mechanism effectively allows a temporal resolution for the analog lines of 3 μs.

The required timing for experiments with the optical lattice, which is described in Chapter 5, is achieved with a separate DDS system and a fast RF-switch, combined with homemade software, that works in parallel with the old system. It allows implementation of fast ramps and short RF pulses on the order of 5 ns.

3.5.1 Locking to the transition

To generate light resonant with the 1083 nm cooling transition, we have an ytterbium-doped fiber laser system (Koheras Adjustik Y10 by NKT Photonics) that is shared with the neighbouring helium setup. The saturated absorption locking mechanism (shown in Fig. 3.11) consists of a glass rf discharge cell filled with He at around 1 mBar. The rf is generated at 27 MHz by an RF resonator[1], and is transferred to the glass cell by two loop antennas around the ends of the cell. This creates a discharge in the gas in which the atoms are excited to i.a. the metastable state, causing a characteristic blue-purple-ish glow.

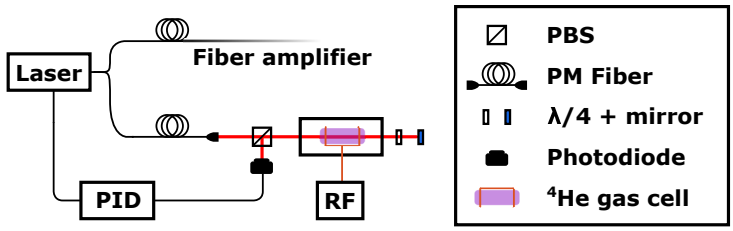

Figure 3.11 – *Schematic of the 1083 nm laser-saturated-absorption-spectroscopy-lock setup. By retroreflecting part of the laser output through a helium plasma discharge with He* atoms, a saturated absorption signal (Lamb dip) can be detected on a photodiode with a lock-in amplifier system (EG&G 5209), and the laser is locked to the 2^3S_1 - 2^3P_2 transition. The other part of the laser light is sent to the fiber-amplifer on the optical table (see Fig. 3.12).*

[1] Designed by the in-house electronic workshop at the VU.

The laser frequency is modulated at 2 kHz using a lock-in-amplifier system (EG&G 5209). The Lamb-dip signal is measured with a photodiode and demodulated by the lock-in amplifier system to generate a dispersive error signal. The error signal is fed into a digital PID system[1] to provide a feedback signal. This feedback signal is linearly amplified to 0-140 V by a voltage amplifier[1] and sent to the piezo transducer of the fiber laser.

3.5.2 1083 nm lasersystem

Part of the resonant light from the laser is split off and sent to a fiber-amplifier (Keopsys), to produce up to 2 W of light. The resulting beam is split up into several paths to be detuned by acousto-optical modulators (AOM's, various models by AA Opto-Electronic and Gooch & Housego) for the various trapping and cooling stages.

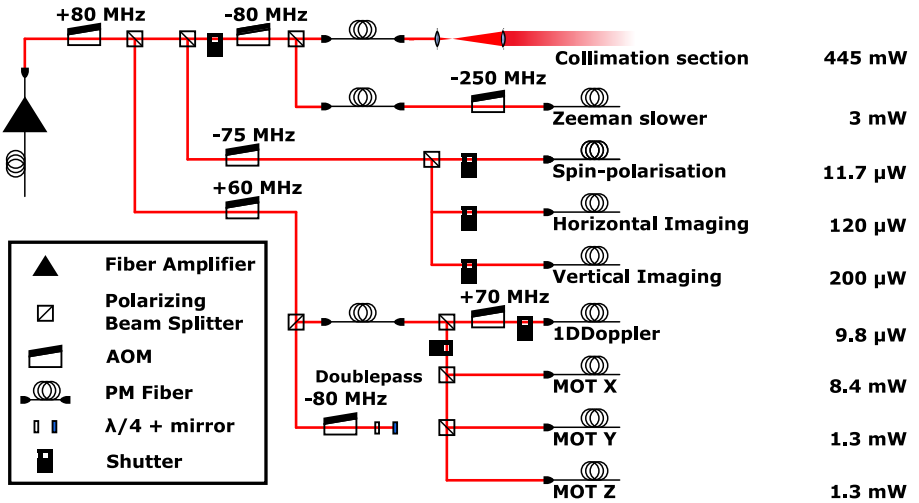

Figure 3.12 – *Schematic of the 1083 nm AOM scheme to produce the variety of detuned beams for the experiment. Only detuned beams are shown, zero orders are left out for clarity. On the right, the out-of-fiber powers at the experiment are listed per beam.*

Fig. 3.12 shows a schematic overview of the resulting beams and their detunings with respect to the resonance frequency at 0 Gauss. The system is designed in such a way that most beams that enter the setup are tunable in both frequency and power, for example to allow ramping of the MOT-light frequency and power for compression or easy small tweaks of the powers to optimize the setup on a weekly basis.

The first AOM at 80 MHz is added to the scheme to detune the resonant light as early on in the optical path as possible to reduce the amount of resonant light that leaks from the table to the main chamber, as stray light significantly disturbs the cooling process to BEC (see Fig. 3.10). For the same reason, a series of laser shutters (Stanford Research Systems) are added to the beam paths. The MOT light is produced by a double-pass AOM that enables frequency tuning of the MOT light over a wide range without loss of AOM efficiency, and thus power. This is actively used in the compression of the MOT, explained in Sec. 2.5.

The AOM's are controlled by a home-built system of voltage controlled oscillators (VCO's) and RF-amplifiers to generate up to 1W of RF at the various used frequencies. For a typical 80 MHz system, the frequency range is approximately ± 15 MHz around the center frequency and both the power and frequency outputs can be controlled by analog input channels (0-5V).

Summary

In this chapter, the design of the magnetic trap has been explained, followed by a description of several trapping and cooling steps. We have seen how a cold cloud is transferred from the MOT to the magnetic trap, with a spin-polarising step in between, to increase the trapped number of atoms. The cloud is 1D-Doppler cooled, decreasing the temperature from 400 μK to 150 μK in 4.5 seconds.

After the 1D-Doppler cooling, the current through the small axial coil set is reduced. This lowers the magnetic field in the center of the trap and makes the magnetic field gradient around the center steeper, effectively compressing the trap. In the compressed magnetic trap, 6 seconds of

forced radio-frequency evaporative cooling is applied to further reduce the temperature of the sample towards degeneracy, of which we have seen signs in Fig. 3.8.

These steps are all crucial for the production of an ultracold sample of atoms, which we want to use in our experiment. The next step is to transfer the atomic sample into an optical dipole trap, in order to be able to do experiments in a magnetic-field-free environment. This is described in Chapter 4.

CHAPTER 4

He* Bose-Einstein Condensate in an Optical Dipole Trap

In 1995, a major breakthrough in ultracold physics occured when the group of Cornell and Wieman and the group of Ketterle achieved Bose-Einstein Condensation with their respective atomic samples. The Jila group managed to cool Rubidium sufficiently deep so that it reached quantum degeneracy [138] and the MIT group achieved this for Sodium [139]. For these achievements, Cornell, Wieman and Ketterle shared the 2001 Nobel prize in Physics. The demonstration of the existence of this ultracold state of matter was proof of Einsteins predictions [140], which were based on work of Bose [141].

The often used terms 'ultracold-' and 'quantum degenerate' physics both represent key features of the field, which is built on the quantum statistics that come into play when a sample of atoms is cooled down to near absolute zero temperature. When reaching a 'temperature'[1] so cold that classical statistics no longer govern the sample's behaviour but quantum statistics takes over, we speak of quantum degenerate gasses. Specifically, at low temperatures, the quantum mechanical property 'spin' starts to matter [142].

[1] At these low temperatures, the concept of temperature loses its meaning, and we speak of phase space density instead. The limit at which Bose-Einstein condensation occurs is the critical temperature, T_c. See Sec 4.3.1 for more details.

When working with bosonic atoms[2], such as ^{4}He*, atoms can occupy a collective ground state of a potential, for example the potential of a dipole trap. This behaviour is governed by Bose-Einstein statistics, which describes indistinguishable particles that can 'condense' into a collective state.

An important and perhaps intuitive approach to understanding the basics of ultracold clouds involves the de Broglie wavelength. In 1924, de Broglie postulated that matter has an associated wavelength

$$\lambda_{dB} = \frac{h}{mv}, \tag{4.1}$$

which we can use as a length scale. If, in a gaseous sample of particles, λ_{dB} is much smaller than the inter-particle distance, the sample is considered classical and the thermal Maxwell-Boltzmann description holds. When the sample cools down and the particles' velocities decrease, λ_{dB} increases. When the de Broglie wavelength becomes comparable or larger than the inter-particle distance, quantum behaviour will be dominant and the behaviour of the gas must be described by the appropriate quantum statistics.

Besides λ_{dB}, another important parameter when it comes to Bose-Einstein condensation is the chemical potential μ, that is a measure for the energy that is required to add a particle to the condensate. This parameter enters the Bose-Einstein distribution function [142]

$$n_{BE}(E,T) = \frac{1}{\exp(E-\mu)/k_B T - 1}, \tag{4.2}$$

which describes the number of particles n_{BE} in quantum state E at temperature T. Since the occupancy for any given state can only be positive, the chemical potential must be negative for $E \geq 0$. If we

[2]Bosons are particles with integer total spin, such as ^{4}He* with S=0. Particles with total non-integer spin are called fermions (such as ^{3}He*) and obey Fermi-Dirac statistics, which is fundamentally different from Bose-Einstein statistics.

assume a fixed number of atoms in a fixed volume, decreasing T is compensated by increasing μ to the limiting case where μ approaches 0. The critical temperature T_c is the boundary where μ hits this limit; at this point Bose-Einstein condensation sets in and a macroscopic fraction of the sample will condense into the lowest energy state.

Bose-Einstein condensation of ^{4}He* was achieved for the first time in the early 2000's at the Institute d'Optique [66] and at the ENS in Paris [65], and later at the VU in Amsterdam [143], ANU in Canberra [144], and MIT in Cambridge [145]. In the recent past, helium BEC experiments were performed at the IQOQI institute at the University of Vienna [146], Institute d'Optique [147], and Amsterdam [74, 88, 148, 149]. For the fermionic isotope ^{3}He*, only in Amsterdam quantum degeneracy was achieved [67, 84]. An overview of the experimental techniques and investigations with He* is given in Ref. [150].

In our experimental scheme, Bose-Einstein condensation occurs at the last stages of the forced evaporative cooling in the magnetic trap, as is shown in Fig. 3.8. Because the last part of the RF-cooling stage is very sensitive to B-field fluctuations, further evaporative cooling is performed after the atoms are transferred to a far off-resonant crossed optical dipole trap (ODT). This trap has several advantages over the magnetic trap, the most important one being the absence of magnetic fields. It allows tuning of bias fields without affecting the trapping potential and allows for rapid turn-off of the trap without decaying magnetic field gradients that can affect the expansion of the atomic sample.

This chapter continues the description of the experimental cycle with the optical dipole trap, the trapping stage after the magnetic trap. First, an explanation of optical dipole trapping is given, along with some characterisations of the ODT. Next, the optical setup for the ODT and the optical lattice is described. Then the detection methods that are employed in our experiment are explained, along with a calibration of the MCP. The chapter ends with a demonstration of our realisation of a He* BEC in the ODT.

4.1 Optical dipole trap

Single beam optical dipole trap

The most straightforward example of an ODT is the single focussed beam geometry. The intensity profile of a Gaussian TEM_{00} mode beam with power P propagating along the z-axis is

$$I(r,z) = \frac{2P}{\pi\omega^2(z)}\exp\left(-\frac{2r^2}{\omega^2(z)}\right), \tag{4.3}$$

where r is the radial coordinate and $\omega(z) = \omega_0\sqrt{1+(z/z_R)^2}$ is the $1/e^2$ intensity radius, with beam waist ω_0 and Rayleigh length $z_R = \pi\omega_0^2/\lambda$. The peak intensity is then $I_0 = 2P/\pi\omega_0^2$, which in combination with Eq. 1.9 results in trap depth

$$U_0 = \alpha(\omega)I_0/2\epsilon_0 c. \tag{4.4}$$

Close to the center, the potential is approximately harmonic and can be described as

$$U_{dip} \approx -U_0\left[1-2\left(\frac{r}{\omega_0}\right)^2-\left(\frac{z}{z_R}\right)^2\right], \tag{4.5}$$

with corresponding trap frequencies

$$\omega_z = \sqrt{\frac{2U_0}{mz_R^2}}, \tag{4.6}$$

$$\omega_r = \sqrt{\frac{4U_0}{m\omega_0^2}}. \tag{4.7}$$

For the parameters of our ODT, where the beams are focussed to $\omega_0 \approx$90 μm and $\lambda = 1557.3$ nm, this would mean that the aspect-ratio of a single beam ODT would be $\sim$260. The Rayleigh length of the beam $z_R \approx$1.6 cm, which is uncomfortably similar to the distance from the center of the vacuum chamber to the re-entrant windows. This means atoms in a single beam ODT are likely to hit the windows, making this an inconvenient geometry to work with.

Crossed optical dipole trap

The solution to the above mentioned issue is the crossed ODT, consisting of two focussed beams at an angle θ (11° in our case), overlapping at their respective foci. This increases the strength of the axial confinement in the region of overlap and alters the axial trap frequency to

$$\omega_z = \sqrt{\frac{4U_0}{m\omega_0^2}}, \tag{4.8}$$

where U_0 is, in this case, the potential created by two beams, so twice as large compared to Eq. 4.6, and the z-axis is now defined along the effective long axis of the trap. The radial directions are no longer completely identical in this geometry, and their trap frequencies can be described by

$$\omega_x = \omega_z \cos[\theta/2], \tag{4.9}$$

$$\omega_y = \omega_z \sin[\theta/2]. \tag{4.10}$$

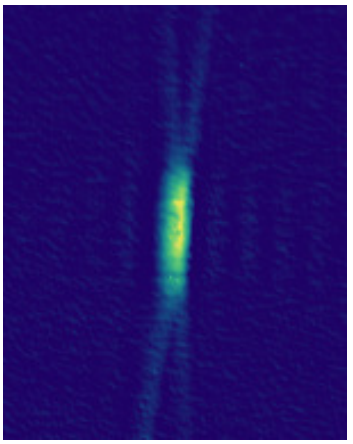

Figure 4.1 – *In-situ absorption image of atoms in the Crossed ODT, taken along the vertical direction. Atoms leaking into the arms of the ODT are faintly visible, extending from the center of the trap.*

This approximation holds as long as $\theta \gg \lambda/\omega_0$ and the beams are of equal size and intensity, which is the case in our experiment. Additionally, the beams are detuned from each other by 160 MHz to prevent interference effects. The aspect-ratio changes from a single-beam ODT value of 260 to $\omega_y/\omega_z \approx 10.5$.

The ODT trap frequencies are of great importance to the behaviour of the atomic sample, both in the trap and after release. It is therefore important to measure them, in order to better understand our trapping conditions and to allow a calibration of the number of atoms in the sample. Fig. 4.2 shows measurements for the axial and vertical trap frequencies, yielding 17.4±0.1 Hz and 226.9±0.2 Hz, respectively. This

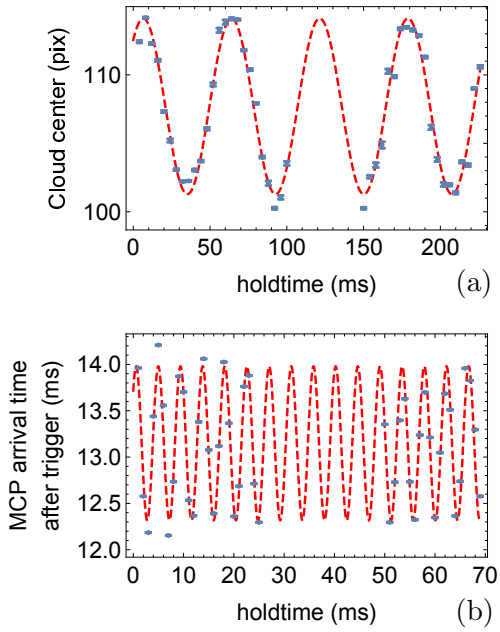

Figure 4.2 – *ODT trap frequency measurements after pushing the atomic sample out of the trap center with a magnetic field pulse.*
(a) Axial freq. 17.4±0.1 Hz, measured with vertical absorption imaging, where the blue datapoints show the fitted center position on the camera.
(b) Vert. freq. 226.9±0.2 Hz, measured with the MCP, the traces are fitted with a Gaussian profile and the center value is taken as the arrival time of the sample (blue points). The red dashed lines show sinusoidal fits.

amounts to an aspect-ratio $\omega_y/\omega_z \approx 13$, slightly higher than expected from Eq. 4.8 and 4.10, indicating that the angle at which the ODT beams cross may be slightly smaller than the measured 11 degrees.

As discussed in Sec. 3.4, the evaporative cooling in the magnetic trap is very sensitive to B-field fluctuations at the final part of the evaporation process. This is why we choose to continue the evaporation in the ODT. We transfer the atomic sample from the magnetic trap to the optical dipole trap by turning on the ODT beams at 450 mW each, before the evaporative cooling in the MT starts. After applying the RF-knife, we gradually turn off the magnetic trap in 200 ms, as to not disturb the condensate in the ODT. The atoms are evaporatively cooled further, by exponentially ramping down the power in both ODT beams to about 80 mW within 500 ms, followed by a hold time of 100 ms. This produces a BEC of about 5×10^6 atoms, which is shown in Sec. 4.3.1.

4.2 1557 nm lasersystem

The 1557 nm lasersystem is used for creating both the optical dipole trap beams and the lattice beams for the experiments described in Chapter 5. The light is generated by a Scorpio laser system from NP Photonics containing an erbium-doped seed and amplifier module with a total output of over 2 W. The laser is used in a free running mode at a wavelength of 1557.3 nm, and part of the light (∼10 mW) is picked off to seed an erbium-doped Nufern amplifier that we operate at ∼7 W, while the remainder is used for the neighbouring helium spectroscopy setup. We employ a 'mirrored' system of AOMs to generate both the ODT beams and the lattice beams from the same laser output, shown in Fig. 4.3.

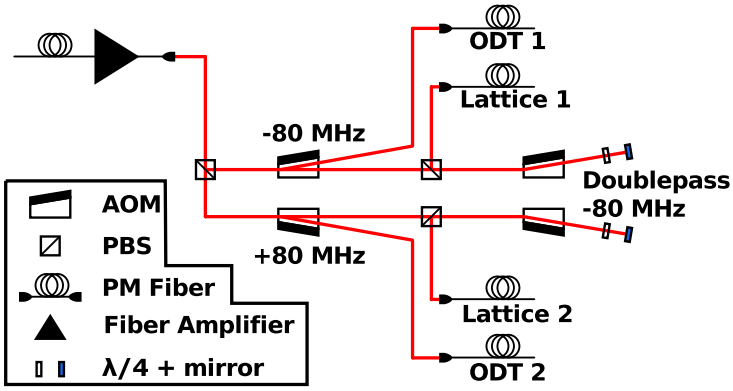

Figure 4.3 – *Schematic drawing of the 1557 nm laser setup, which is placed inside an isolated box on the laser table. The detuned beams of the two AOMs at the left are used to make the ODT beams, which are 160 MHz detuned with respect to each other, in order to prevent standing wave effects. The two doublepass AOMs are used to create two lattice beams that can be chirped individually.*

By using the undetuned zero-order beam from the ODT AOMs for the lattice double-pass AOMs, we use most of the available power. This enables the generation of two ODT beams that are 160 MHz detuned from each other, while having identical lattice beam frequencies, that are adjustable through individual control over the double-pass AOM

frequencies. The maximum power in the lattice beams is 300 mW per beam, the maximum power in the ODT beams is limited by the damage threshold of the fibers to 500 mW per beam.

In Fig. 4.4 the 1557 nm part of the optical setup around the main chamber is shown. The MOT coils are shown as reference points, in between them the crossed ODT beams (red) and the optical lattice beams (blue) are focussed. The fibers shown in the figure originate from their respective namesakes in Fig. 4.3. The crossed ODT beams can be aligned independently from each other, by moving a 500 mm focal length lens that is mounted on a 3D-micrometer stage. These stages allows fine-tuning of the overlap of the ODT-foci with the position of the magnetic trap center, which is crucial for optimising the transfer of the atomic sample.

The beam-waists of the ODT beams are focussed down to $\sim$90 μm, corresponding to a Rayleigh length of $\sim$1.6 cm. The ODT 1 beam is sent into the chamber along the long trap axis of the magnetic trap (or, equivalently, along the horizontal MOT beam). ODT 1 is reflected into the chamber by a shortpass dichroic mirror with a cutoff-wavelength at 1180 nm. (Thorlabs DMSP1180L), which allows the 1083 nm MOT beams to pass unhindered[3]. After having passed through the chamber, the 1557 nm light is reflected out of the MOT beam path again by a second dichroic mirror. Beam ODT 1 is reflected into a beam dump by a homebuilt optical isolator stage that consists of two PBS's and a near-IR Faraday rotator (Thorlabs I1550R5), that prevents backcoupling of light into the lattice fibers.

In order to execute lattice experiments on a sub-5 μs timescale, pre-programmed frequency ramps from home-built DDS's are used in combination with a fast RF switch to induce fast ramps of the frequencies of the lattices. This will be further explained in Sec. 5.2.

[3] Almost unhindered; since the dichroics are not exactly at 45° with respect to the MOT beam, there is a slight birefringent effect, but not so severe that it reduces the number of trapped atoms in the MOT.

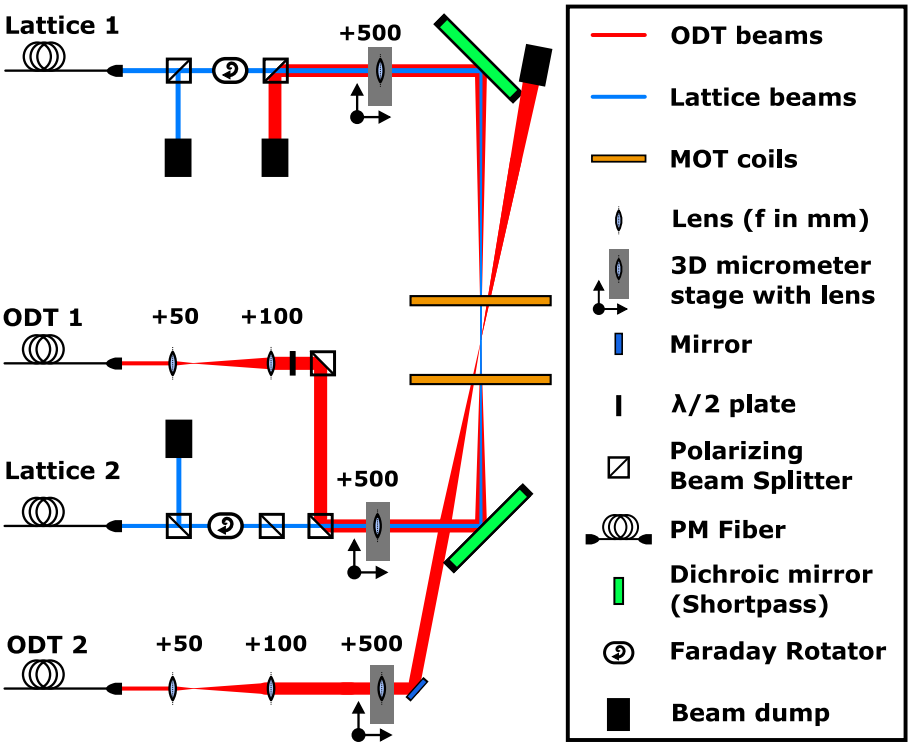

Figure 4.4 – *Schematic top view of the 1557 nm beam configuration at the level of the main chamber (not to scale). The crossed optical dipole trap is shown in red, with the foci overlapping in between the MOT coils, shown here for reference. The horizontal lattice beams are overlapped with one of the ODT beams to ensure overlap with the atomic sample. A system of polarising beam splitters and Faraday rotators is employed to ensure the lattice beams are not coupled back into the fibers. The shown fibers connect to their respective namesakes in Fig. 4.3. More info on the optical lattice is given in Chapter 5.*

4.3 Detection methods

4.3.1 MCP

The MCP detector (Hamamatsu F4766, 7.25 mm detector surface radius) is located 24.5 cm underneath the trap center. It is mounted on a

horizontal translation stage which allows it to be moved out of the way for the vertical lattice and vertical imaging beam. It is shielded with a grounded metal mesh (76 μm thread, 65% transparent) to prevent attracting electrons and ions, while allowing metastable atoms to pass through unhindered.

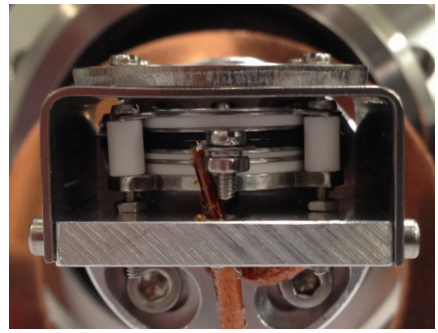

Figure 4.5 – *Photograph of the MCP detector with grounded shield on its translation stage.*

When a metastable helium atom impacts on the MCP surface, its internal energy is transferred to a surface electron which is accelerated to the back of the detector by a potential of up to 2.5 kV, generating an avalanche of electrons on its way. This allows the conversion of a flux of atoms into current pulses which can be measured at the anode of the MCP. This means a flux of atoms is measured in a time dependent fashion. The large gain of the MCP (up to 10^8) allows the detection of even low density clouds of atoms that would be challenging to measure with absorption imaging. The large gain, in combination with a pulse discriminator, even allows for single atom detection.

For MCP time-of-flight measurements, the atoms arrive at the detector after a ∼220 ms free fall under gravity. In this time, the momentum distribution of the expanding cloud completely determines the size of even the coldest cloud we can produce [84], which makes the measurement a suitable tool for temperature determinations. Also, there are analytical descriptions for the TOF-flux signals for clouds of various temperatures, which are extensively discussed in Ref. [132], which makes straightforward characterisation of the sample possible. The sections below provide an overview of the different functions that are used to analyse the different temperature regimes.

Thermal distributions

When a trapped cold atomic cloud is released, its size at the MCP detector is dependent on the initial size and the temperature. By measuring the time-of-flight flux profiles of the falling cloud, these properties can be reconstructed by fitting with a straightforward analytical function. For clouds with a temperature much higher than the critical temperature for a BEC, the profile can be described by the well known Maxwell-Boltzmann distribution. The flux of thermal atoms at the detector position is [84, 143]

$$\Phi_{th}(t) = N_{th}\frac{g}{\sqrt{2\pi}\,\sigma(t)}\frac{t^2+t_0^2}{2t}\;\exp\left(-\frac{x_0^2}{2\sigma(t)^2}\right)\left(1-\exp\left(-\frac{r_0^2}{2\sigma(t)^2}\right)\right), \tag{4.11}$$

where N_{th} is the total atom number, g the gravitational acceleration, $\sigma(t) = t\sqrt{k_BT/m}$ the ballistically expanding size of the cloud at time t, $t_0 = \sqrt{2h/g}$ the expected arrival time of the free falling cloud, $x_0 = h - gt^2/2$ with h =24.5 cm and r_0 =7.25 mm the radius of the MCP detector. For a MOT, the number of atoms can be obtained by fitting Eq. 4.11 to the TOF profile, as is shown in Fig. 2.17.

Ideal Bose gas

As the temperature of the atomic sample decreases (to in our case $\sim$1 μK), the chemical potential becomes non-negligible compared to the thermal energy and Bose-Einstein statistics have to be taken into account. The integrated flux for a Bose gas is [137]

$$\begin{aligned}\Phi_{Bose}(t) = &\frac{N_{th}}{g_3(z)}\frac{g}{\sqrt{2\pi}\sigma}\frac{t^2+t_0^2}{2t^2}\\ &\times\left[g_{5/2}\left(z\;\exp\left(-\frac{x_0^2}{2\sigma^2}\right)\right)-g_{5/2}\left(z\;\exp\left(-\frac{x_0^2+r_0^2}{2\sigma^2}\right)\right)\right]\end{aligned} \tag{4.12}$$

where the functions $g_n(u) = \sum_{j=1}^{\infty}(u^j/j^n)$ are called the Bose functions and $z = e^{\mu/k_BT}$ is the fugacity of the gas. In the limit where $k_BT \gg \mu$, Eq. 4.12 reduces to Eq. 4.11.

Bose-Einstein Condensates

In ultracold samples, quantum statistics play a dominant role. As the temperature of the sample decreases towards absolute zero, the atoms will start collectively occupying the ground state of the potential. The critical temperature at which this starts to occur is given by

$$k_B T_c = 0.94 \hbar \bar{\omega} N^{1/3}, \tag{4.13}$$

with average trap frequency $\bar{\omega} = (\omega_{rad}^2 \omega_{ax})^{1/3}$ and total number of thermal and BEC atoms N. Below T_c, the condensed fraction of the cloud is described by the time-independent Gross-Pitaevskii (GP) equation,

$$\left(-\frac{\hbar^2 \nabla^2}{2m} + V_{ext}(\vec{r}) + \tilde{g} |\Psi_0(\vec{r})|^2 \right) \Psi_0(\vec{r}) = \mu \Psi_0(\vec{r}), \tag{4.14}$$

where the first term is the kinetic part of the equation and V_{ext} denotes the trapping-potential. The third term introduces interactions between the atoms, with coupling constant $\tilde{g} = 4\pi\hbar^2 a/m$ being determined by s-wave scattering length a.

The density distribution of the condensate is found by solving the GP equation in the Thomas-Fermi approximation, which can be applied when the kinetic energy of the sample can be neglected with respect to the interaction energy [151]. The solution to the GP equation then becomes

$$n_{TF}(\vec{r}) = \frac{1}{\tilde{g}} [\mu - V_{ext}], \tag{4.15}$$

which descibes the density distribution of the BEC in the trap potential V_{ext}, with chemical potential μ. In the case of an harmonic trap, the profile assumes the characteristic parabolic shape. Normalisation leads to a relation between the atom number and the chemical potential of the condensate

$$\mu = \frac{1}{2} \left(\bar{\omega}^3 \hbar^2 m^{\frac{1}{2}} \right)^{2/5} N_{BEC}^{2/5}. \tag{4.16}$$

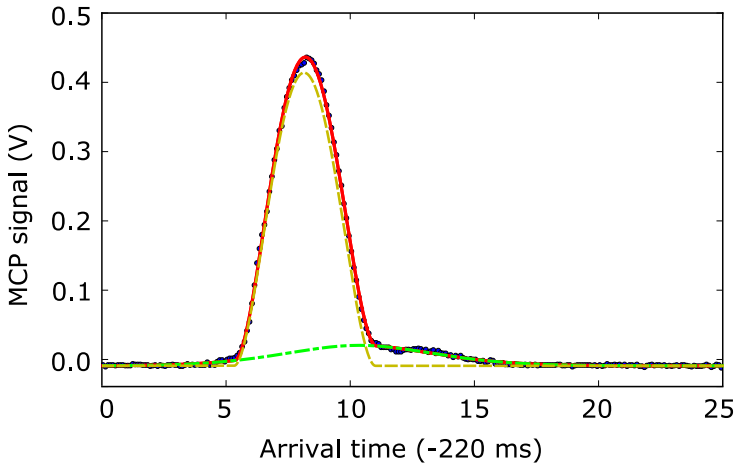

Figure 4.6 – *The blue datapoints make a time of flight signal of a typical BEC on the MCP detector, after a holdtime of 1 second. The time axis shows the observation time, which is set to 220 ms after the atoms are released from the trap. The red line is a fit of* $\Phi(t) = \Phi_{BEC}(t) + \Phi_{Bose}(t)$*, shown as the dashed yellow line (BEC fraction) and the dotted-dashed green line (thermal fraction), yielding* $N_{BEC} \approx 5.2 \times 10^6$ *atoms.*

As an harmonic trap is turned off and the condensate starts falling, the internal energy (or mean-field energy) is converted into kinetic energy, because the repulsive interaction pushes the cloud outward. The shape of the cloud undergoes a rescaling of the parabolic shape, leading to aspect-ratio inversion, a very characteristic property of BEC physics [152]. This effect is demonstrated in our experiment in Sec. 4.3.3. The flux at the MCP detector now becomes

$$\Phi_{BEC}(t) = N_{BEC}\frac{15}{16}g\frac{t^2+t_0^2}{2t^2}\sqrt{\frac{m}{2\mu}}\ \max\left[0,\ \ 1-\frac{m}{2\mu}\left(g\frac{t^2-t_0^2}{2t}\right)^2\right]^2, \tag{4.17}$$

Usually, an ultracold cloud that is detected on the MCP is analysed by fitting $\Phi(t) = \Phi_{BEC}(t) + \Phi_{Bose}(t)$ to the trace, because there will usually be some fraction of atoms in the 'thermal fraction', which is what we call the atoms that have not condensed into the ground state of the

trap. We fit them with $\Phi_{Bose}(t)$ because they are still very cold. A typical signal is shown in Fig. 4.6. This shows there are two regimes in practice; one in which the temperature is high compared to T_c and $\Phi_{th}(t)$ is the appropriate fit function, such as in Fig. 2.17, and the other where the temperature is of the order T_c and $\Phi(t) = \Phi_{BEC}(t) + \Phi_{Bose}(t)$ is the correct way of extracting information from the data. The MCP calibration is performed using a BEC and is explained in Sec. 4.3.2.

4.3.2 MCP calibration

The signal of the MCP detector is dependent on the electronics that amplify the MCP signal and is also sensitive to saturation effects of the MCP. To derive a number of atoms from the MCP measurements, we plot the chemical potential μ as a function of $N_{BEC}^{2/5}$, the number of atoms in the BEC to the power $\frac{2}{5}$. By increasing the holdtime in the trap, the number of atoms that remain in the trap decreases, and the chemical potential decreases along with it. Since we know that the relation between these two variables should be given by Eq. 4.16, we can retrieve a relation between the number of atoms in a condensate and the area underneath a BEC peak. This is done by fitting a line to the data in Fig. 4.7 and normalising the obtained slope value to provide a conversion factor, which in our case yields that we have $5.2{\times}10^6$ atoms in our BEC after a 1 second holdtime, with a condensate fraction of about 90%.

4.3.3 Absorption imaging

The MCP detection method, discussed in the previous section, is a unique selling point for helium. However, it cannot be used to investigate time-dependent behaviour of the expanding cloud, because it is limited to a fixed distance from the trap center. The conventional detection technique that is used in cold atom experiments is absorption imaging (for He* at 1083 nm), where a camera records a reduction of light due to resonant absorption by atoms, an example of which is shown in Fig. 4.1. The imaging method effectively records the 'shadow' the atoms cast on the camera chip, from which, if the trap parameters are known, the

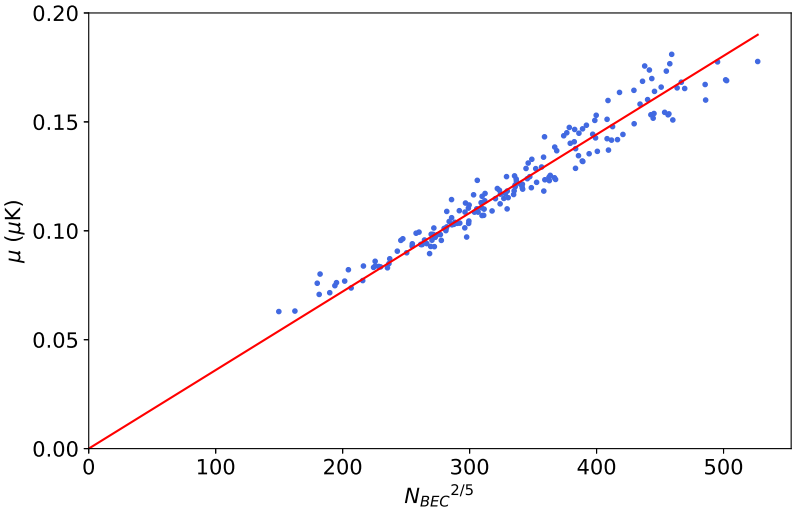

Figure 4.7 – *Chemical potential μ as a function of $N^{2/5}$ The red fit provides a slope that, together with Eq. 4.16 gives a conversion factor of 8.9×10^9 atoms/V·s.*

number of atoms and the temperature can be extracted. Furthermore, since an image can be taken at any time during the sequence[4], it can be used to investigate time-dependent behaviour of the atoms in one of the various trapping potentials. There are some limitations, most notably that after some time, the atomic cloud becomes too dilute and it absorbs insufficient light to create a discernible 'shadow' on the camera. Also, after release from the trap the atomic sample will fall out of the field of view of the camera due to gravity.

We use a Xenics Xeva 2.5-320 infrared camera, which consists of 320 x 256 pixels of 30 x 30 μm. It is an InGaAs detector, which at 1083 nm has a relatively high quantum efficiency of 60% compared to silicon based devices with $\leq$ 1.5% efficiencies. To avoid heating or imposing significant light forces on the atoms, low intensity light($I \ll I_{sat}$) is

[4]though not without consequence; absorption imaging, just like MCP detection, is a destructive measurement technique.

used to image the atomic sample, typically about 60 μW/cm^2. Under these conditions, the transmitted light intensity through a cloud with density distribution $n(x, y, z)$ decreases exponentially with the optical thickness of the cloud as

$$I_{out}(x, y) = I_{in}(x, y) \exp\left(\frac{-\hbar\omega_0(\Gamma/2)}{I'_{sat}} \int n(x, y, z)dz\right), \tag{4.18}$$

with transition frequency ω_0, linewidth $\Gamma/2\pi$ and effective saturation intensity $I'_{sat} = fI_{sat}/\xi$. The saturation intensity is modified by the factor f by the evolution of the population of the magnetic sublevels during the exposure to the probe light and polarisation of the light. In the MOT stage, $f = 18/10$ for unpolarised atoms and circularly polarised light, but changes to $f = 1$ due to pumping to the spin-stretched case. For circularly polarised light and spin-stretched atoms, which is the case after the MOT stage, $f = 1$ throughout the probing process.

We use circularly polarised light for the horizontal imaging, but because the effects are small due to the very short probe time (100 μs exposure per shot), they can be neglected [132, 134, 153]. The line-shape factor ξ is dependent on the magnetic field, temperature of the cloud and the properties of the laserbeam. It is discussed in detail by Tol [153].

The column density $n(x, y, z)$ can be determined by combining three measurements: the transmission image $I_{abs}(x, y)$ of the cloud, a cloudless picture of the probe beam $I_{probe}(x, y)$, which is taken 200 ms after release of the cloud, to ensure no atoms remain, and $I_{bgr}(x, y)$, a background image without probe light. The normalised transmission is then

$$\frac{I_{out}(x, y)}{I_{in}(x, y)} = \frac{I_{abs}(x, y) - I_{bgr}(x, y)}{I_{probe}(x, y) - I_{bgr}(x, y)}. \tag{4.19}$$

Fit functions for absorption images

Like the fit functions for the MCP traces in Sec. 4.3.1, absorption images can be analysed in order to extract information from the data. After a fringe-removal algorithm [137] that corrects artefacts from e.g. interference effects in the camera, otherwise leading to unphysical variations in light intensity between $I_{abs}(x, y)$ and $I_{probe}(x, y)$, the column density of the cloud can be retrieved

$$n(x, y) = -\frac{1}{\hbar\omega_0(\Gamma/2)} I_{sat}^{'} \ln\left(\frac{I_{out}(x, y)}{I_{in}(x, y)}\right). \tag{4.20}$$

Depending on the temperature of the sample, the distribution can be fitted with the appropriate function to extract physical parameters. Following the derivations in [132], the column density distribution for a thermal cloud (MOT) is assumed to be Gaussian shaped

$$n_{th} = \frac{N_{th}}{2\pi\sigma_x\sigma_y} \exp\left(-\frac{x^2}{2\sigma_x^2} - \frac{y^2}{2\sigma_y^2}\right), \tag{4.21}$$

with total atom number N_{th} and widths of the expanding cloud σ_i. After $\sim$ 1 ms, the widths of the cloud increase as $t\sqrt{k_B T/m}$ along every axis [84], which allows for thermometry by studying the time-dependent expansion of the cloud.

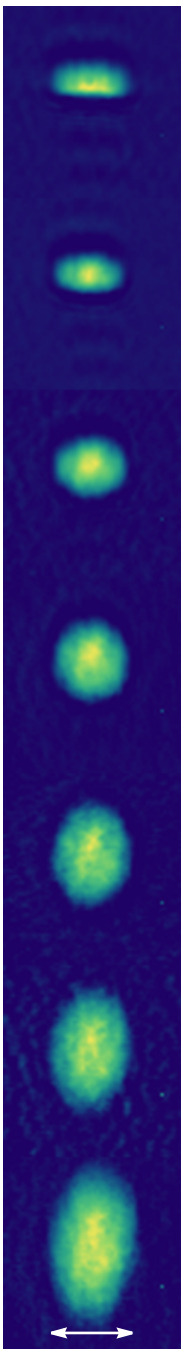

Figure 4.8 – *Aspect-ratio inversion of an ultracold cloud after release from the crossed optical dipole trap, observed with vertical imaging. The first image corresponds to an expansion time of 0.1 ms, increasing 4 ms with every consecutive TOF image. The weak trapping axis of the crossed optical dipole trap is oriented along the white arrow that indicates the scale of 500 µm.*

Once the cloud is cooled near critical temperatures, the density distribution starts to be influenced by quantum statistics, similar to the MCP detector case. For a gas close to T_c, the fit function becomes [137]

$$n_{Bose}(x,y) = \frac{N_{th}}{2\pi\sigma_x\sigma_y g_3(z)} g_2\left(z\ \exp\left(-\frac{x^2}{2\sigma_x^2} - \frac{y^2}{2\sigma_y^2}\right)\right), \tag{4.22}$$

with fugacity z and Bose functions $g_n(u)$. The imaging fit-function for a cloud below T_c is different from a Bose gas, and can be described in the Thomas-Fermi limit as

$$n_{BEC}(x,y) = \frac{5}{2\pi}\frac{N_{BEC}}{r_x r_y}\ \max\left[0,\ \ 1 - \frac{x}{r_x}^2 - \frac{y}{r_y}^2\right], \tag{4.23}$$

with r_i $(i = x, y)$ the radius of the trapped or expanding condensate. If the condensate is trapped, $r_i = \sqrt{2\mu/m\omega_i^2}$ is the Thomas-Fermi radius [152], which gives the original shape of the cloud as determined by the trap frequencies. Due to a difference in trap frequency for the different directions mentioned in 4.1, the expansion can differ greatly between these different directions. Specifically, the strength of the axial trapping axis is lower than that of the radial trapping axis, so the gradient of the mean field shift in the axial dimension is lower, leading to a slower expansion with respect to the radial dimensions. The radii increase as [151]

$$r_{rad}(t) = r_{rad}(0)\sqrt{1+\tau^2}, \tag{4.24}$$

$$r_{ax}(t) = r_{ax}(0)\left[1 + \frac{\omega_{ax}}{\omega_{rad}}^2\left(\tau\ \arctan(\tau) - \ln\sqrt{1+\tau^2}\right)\right], \tag{4.25}$$

with $\tau = \omega_{rad}t$. This results in aspect-ratio inversion, a transformation of the initial cigar-shaped cloud to a pancake-like shape, which can be observed with absorption imaging, and is considered an indication of Bose-Einstein Condensation. A demonstration of this effect is shown in Fig. 4.8, where we look along the vertical direction of the trap and increase the time-of-flight after release from the ODT for every consecutive shot.

Similar to the MCP fit fuctions, the absorption image can be fit by a combination of $n_{Bose} + n_{BEC}$ to simultaneously extract information about both temperature classes that make up the atomic sample.

Summary

In this chapter, we have seen the capture and further evaporative cooling of a cold atomic cloud in the horizontal crossed optical dipole trap, resulting in a BEC of $\sim 5 \cdot 10^6$ atoms. The optical system to create the ODT laser-beams is detailed and the two different detection techniques, absorption imaging and MCP detection, are explained. We are now ready to start performing actual experiments with the ultracold atomic sample that is prepared.

In the next chapter, the cloud will be transferred to an optical lattice and the peculiar behaviour of the atoms that ensues will be studied.

CHAPTER 5

Bloch Oscillations

QUANTUM mechanical effects rarely manifest themselves in a directly visible way in our macroscopic world, though they are of great importance for a deeper understanding of that same world. In the previous chapter we have seen quantum behaviour in action with the production of a Bose-Einstein condensate. In this chapter, we report the observation of Bloch oscillations (BO's) of a ^{4}He* Bose-Einstein condensate in an optical lattice at 1557.3 nm.

Bloch oscillations of cold atoms in periodic potentials formed by optical lattices were first studied by Ben Dahan *et al.* [154] and Wilkinson *et al.* [155]. Peik *et al.* [156] gave a quantum-optical interpretation of this effect in terms of photon exchanges between the atoms and the laser fields, showing that Bloch oscillations are equivalent to a sequence of rapid adiabatic passages between momentum states. Importantly, BO's provide a way to efficiently accelerate atoms by coherently transferring a well controlled, large number of photon momenta, which has been used to increase the resolution of recoil measurements with caesium and rubidium atoms [7, 46, 157, 158].

In this chapter, we demonstrate efficient momentum transfer via Bloch oscillations in an optical lattice and demonstrate the enhanced sensi-

This chapter is based on: *Bloch Oscillations with a metastable Helium Bose-Einstein Condensate*, R.F.H.J. van der Beek, O. Onishchenko, W. Vassen, K.S.E. Eikema, and H.L. Bethlem, Physical Review A **102**, 061302(R) (2020).

tivity offered by micro-channel plate detector based detection schemes. First, the theoretical framework around Bloch Oscillations is explained. Next, the optical lattice and its configuration in our experiments is described. This is followed by a demonstration of the method we use for calibrating the lattice depth. Finally we show a series of measurements that demonstrate efficient Bloch oscillations and their promising behaviour in relation to atom interferometry.

5.1 Bloch Oscillations - atoms in an optical lattice

First conceived by Bloch when theorising about electrons moving in crystal lattices, so-called Bloch oscillations describe the behaviour of electrons in periodic electric potentials [159]. Zener added a necessary piece of the puzzle that explained avoided crossings in an energy diagram [160]. Their predictions implied that electrons in a periodic electric field do not move in a linear fashion, but rather oscillate as a result of the periodicity of the potential. Bloch oscillations have never been observed in natural crystals because the very high scattering rate due to lattice defects prevents electrons from completing a Bloch period [161]. The first observation of Bloch oscillations was demonstrated in semiconductor superlattices, which were engineered with a large spatial period to increase the Bloch period, bringing the observable Bloch frequency in the THz regime [162].

To observe Bloch oscillations with atoms, the above mentioned issues are overcome by using 'perfect' optical lattices, greatly reducing the scattering rate due to defects. An added advantage is that an optical lattice, which operates at 1557 nm in our case, greatly increases the lattice period with respect to atomic crystal structures. This increases the Bloch period to time scales that are experimentally more easily accessible.

Consider a particle in a periodic potential, in our case an optical lattice potential $U(x) = U_0 \cos^2(kx)$ with $k = \frac{\pi}{d}$, where d is the lattice spacing, and potential depth U_0, usually given in units of the recoil energy, which

is in our case $E_R = \hbar^2 k^2 / 2m_{\mathrm{He}^*}$. The Hamiltonian is then

$$\hat{H}\psi(x) = \left(-\frac{\hbar^2}{2m}\frac{\partial^2}{\partial x^2} + U(x) \right) \psi(x). \tag{5.1}$$

The Bloch theorem [159] states that solutions for the eigenstate of this Hamiltonian are of the form

$$\psi_{n,q}(x) = e^{iqx} u_{n,q}(x), \tag{5.2}$$

with band index n, quasimomentum[1] q, defined modulo $2k$ and periodic function

$$u_{n,q}(x) = u_{n,q}(x + d). \tag{5.3}$$

Following the derivation in [163], the eigenvalues and eigenstates of the Hamiltonian of Eq. 5.1 can be calculated numerically for a finite number of coupled states. If a constant external force is introduced into the Hamiltonian, the resulting solutions are periodic in q and will show an oscillatory behaviour that has a period equal to

$$T_{Bloch} = \frac{2\hbar k}{ma}, \tag{5.4}$$

where the combination of atomic mass m and acceleration a form the external force, which could be gravity, for example. The energy solutions are commonly depicted as shown in Fig. 5.1, where the band structure of an atom in a $2E_R$ deep optical lattice is shown from $-q$ to q, commonly referred to as the first Brillouin zone. The dispersion relation of a free particle is shown as the quadratic gray dashed line. As a consequence of the band splitting, which increases linearly with lattice depth, the first Bloch band is flattened at the points it splits from the second band, breaking the quadratic shape of the band. When an atom is prepared in the first band, it can remain in this band under the influence of a 'weak' force, which will induce an oscillatory motion in q.

[1] quasimomentum or crystal momentum q is the 'good' quantum number, as opposed to the free-case momentum, since $\hat{p}$ does not commute with $\hat{H}$. For an atom in a moving lattice, q serves as the momentum with respect to the lattice.

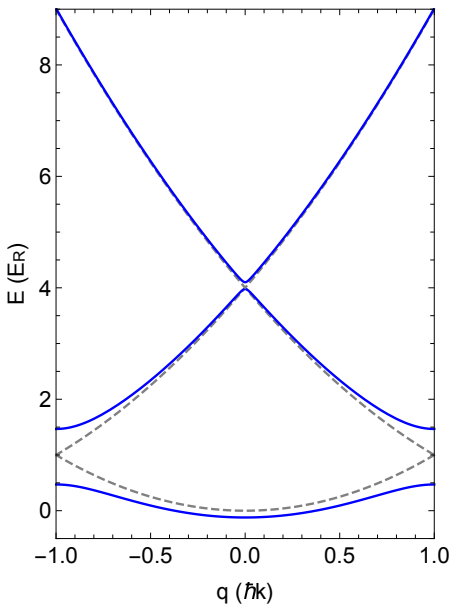

Figure 5.1 – *Level splitting of the Bloch bands of an optical lattice with $2E_R$ depth as a function of quasimomentum q. In the absence of a lattice, the kinetic energy of a particle will follow the well known quadratic momentum behaviour (dashed gray lines). The blue lines show the resulting band splitting for a lattice with one recoil energy lattice depth. Since the solutions for the energy bands are periodic in q with $2\hbar k$, the plot must be seen as if wrapped around a cylinder, with the bands connecting at $q = -1$ and 1.*

Fig. 5.1 should be viewed as if on the outside of a cylinder, such that $q = -1$ and $q = 1$ connect to form a continuous structure. In this frame, a Bloch oscillation can be explained as a particle moving over the lowest Bloch band. Consider a particle at rest, loaded into a lattice with zero velocity. If the lattice is now accelerated, the particle starts moving along the q axis. Once it approaches the edge of the Brillouin zone at $q = 1$, given that the acceleration is adiabatic, the particle continues moving over the lowest band, which means it will appear at the $q = -1$ point. This 'jump' in q-space is a real world change of momentum by $2\hbar k$, which occurs at the point where the lattice is moving at 1 v_R with respect to the particle. This results in the scenario that the particle that is now moving faster than the accelerating lattice and continues to move over the band until their respective velocities match at $q = 0$ and a full Bloch oscillation is completed.

Considering a constant force acting on a particle in the lattice, the mean velocity of the particle in band n can be written as [154]

$$\langle v \rangle_n(q) = \frac{1}{\hbar} \frac{dE_n(q)}{dq}, \tag{5.5}$$

which means the derivative of the band determines the shape of the velocity behaviour of the particle in the lattice. Specifically, if the lattice is weak and the bands are only slightly split, the derivative at the edges of the Brillouin zone are steep. This makes for a steep 'jump' in momentum space at half the Bloch period, whereas a deeper lattice that flattens the bands considerably, makes for a flatter derivative and therefore a more gradual momentum change.

5.2 Optical lattice

In our experiment, the optical lattice is made of two counterpropagating laserbeams that interfere to create a standing wave potential in which the atomic sample can be trapped. For linearly polarised beams, the potential is four times that of a single beam ODT (Eq. 1.9) due to interference effects. Fig. 5.2 shows the last part of the experimental setup including a cut-through of the coils used for creating the required magnetic fields, and part of the optical setup. The ultracold sample can be detected either by absorption imaging in time of flight or by letting the atoms fall onto a micro channel plate (MCP) detector. Absorption images are recorded by shining light resonant with the $2^3S_1 - 2^3P_2$ transition near 1083 nm (shown in purple in the figure) onto the camera. The MCP detector is placed 245 mm below the trap center, on a translation mount such that it can be moved 20 mm out of the center to allow vertical lattice beams to pass. Atoms falling under gravity are pushed towards the moved MCP by briefly pulsing a current through a magnetic field coil positioned just above the MCP.

As shown in Figures 4.4 and 5.2, isolator stages are implemented after the fibers that transport the lattice light to the experimental chamber, to protect the AOM's and fiber amplifier from backreflected light. Some tens of μW of power leak through these isolators, which we use to ensure the lattice beams are nicely overlapping by backcoupling the lattice beams into each others fibers (which does not harm the amplifier or

AOM's). The horizontal lattice is overlapped with one of the optical dipole trap arms, to ensure overlap with the atomic sample and optimise the transfer into the lattice.

In order to induce Bloch oscillations (BO's), we create an optical lattice potential from two counterpropagating beams that are derived from the same fiber amplifier as the ODT beams. Independent control of the power and timing of the ODT and lattice beams is achieved by using a distribution system of four acousto-optic modulators (AOM), as shown in Fig. 4.3.

For experiments in the horizontal one-dimensional (1D) lattice, the lattice beams are overlapped with one of the ODT beams on a polarizing beam splitter (PBS), as shown in Fig. 4.4. The $1/e^2$ waists of the lattice beams are set to 200 μm, i.e., approximately two times larger than the ODT. The AOMs used for lattice beam frequency control are driven by RF signals produced by direct digital synthesizer boards (DDS, Analog Devices AD9954), and then amplified by home-made RF amplifiers. This system makes it possible to ramp up the RF to well above 1 MHz/ms, needed to induce fast BO's.

BO's in the horizontal lattice configuration are induced by a linear frequency ramp of one of the lattice beams. The effective acceleration of the lattice is then given by

$$a = \frac{\lambda}{2} \frac{d\Delta\nu(t)}{dt}, \tag{5.6}$$

where λ is the lattice laser wavelength and $\Delta\nu(t)$ is the frequency difference between the two lattice beams [156]. The lattice beams can be controlled in both frequency and power by controlling the RF that is supplied to the AOMs (Gooch-Housego, 97-03199-01). The RF is generated by two direct digital synthesizers that are referenced to a common 20 MHz, provided by an AWG (Agilent 33250a).

Once pulse-settings are loaded into the timetable of the control software, the relevant parameters are uploaded to an Arduino controller,

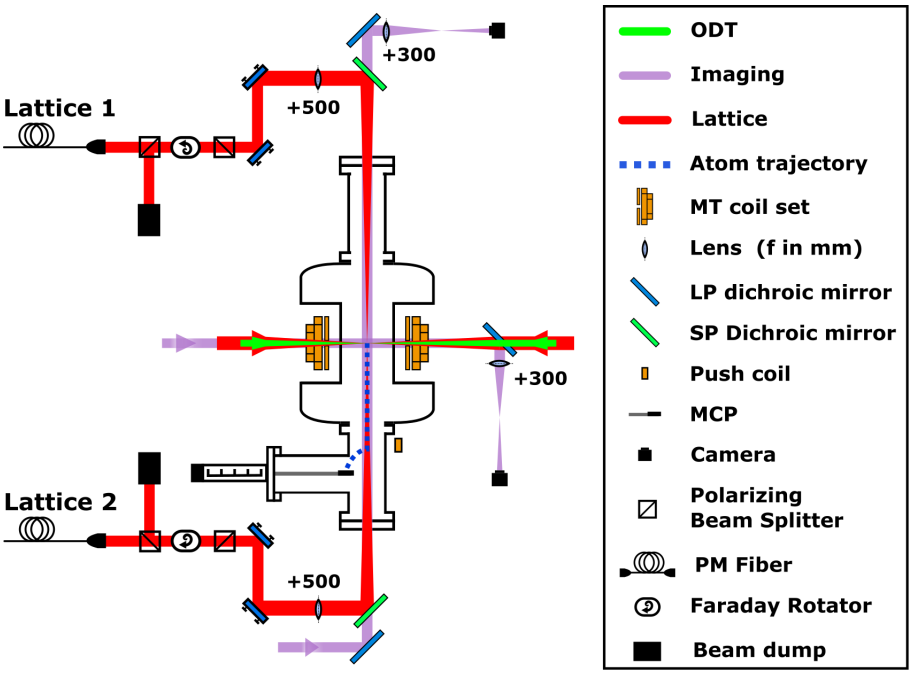

Figure 5.2 – *Schematic side view of the experiment showing a cross-section of the science chamber (not to scale), with the horizontal and vertical lattices (1557 nm) shown in red, the ODT (1557 nm) in green and the imaging beams (1083 nm) in purple. The horizontal lattice and ODT are shown here as horizontal focussed beams, a top view is shown in Fig. 4.4. Atoms are detected using absorption imaging after a short expansion time or by dropping the atoms onto a micro channel plate (MCP) that is mounted 245 mm below the trap center. The MCP is mounted on a translation stage that allows moving the detector out of the way of the vertical laser beams. Atoms are in this case pushed onto the detector by pulsing a current through the push coil. To separate the imaging light from the lattice- and ODT light, short- and longpass dichroic mirrors are implemented. The optics for the vertical lattice (shown in Fig. 4.4 for the horizontal lattice) consists of a combination of polarising beam splitters and Faraday rotators to ensure the lattice beams are not coupled back into each others fibers.*

which is triggered by the control software every time a new frequency- or power-ramp is required. The DDS's respond with a tunable output frequency and power, which is pre-amplified (Minicircuits TB-409-6+) and amplified (home-built) to up to the needed 2.5 W. This system works properly for pulse times of less than 200 μs and inter-pulse times of 1 ms. For shorter pulse lengths, as is the case with Rabi-measurements (see Sec. 5.3), we employ an RF switch in between the RF pre-amps and the RF amplifiers, which we use to cut pulses down to 5 μs out of the DDS output. The 1 ms inter-pulse time is set by the dead-time of the Arduino.

5.3 Calibration of the lattice: Rabi oscillations

In order to determine the depth of our optical lattice, we can use a measurement of the waist using the knife-edge method [164], which yields $w_0 \approx 200$ μm, to arrive at a depth of $\sim 0.88 E_R$ per 100 mW of power per lattice beam. This method assumes identical powers and waist sizes per beam, which is not necessarily the case. Moreover, it assumes perfect alignment, which is even more tricky.

An alternative method is to let the atoms reveal the depth of the lattice. This involves abruptly switching off an optical lattice moving at a speed of one recoil velocity, i.e. half the speed that is obtained in a Bloch oscillation. When looking at this case in the band-structure picture, the atoms are at the edge of the Brillouin zone, where the first and second band have split up. Since the populations of the two bands acquire a phase difference that is proportional to the lattice depth [163], the populations oscillate in and out of phase at frequency

$$2\pi f_{Rabi} = \frac{1}{2\hbar} U_0, \tag{5.7}$$

with lattice depth U_0 in units of E_R [165]. Fig. 5.3 shows a measurement of Rabi-oscillations of helium atoms in the horizontal optical lattice between momentum states with $0\hbar k$ and $2\hbar k$ with a damped sinusoidal fit that yields a lattice depth of $1.2 E_R$ at 150 mW per lattice beam, i.e.

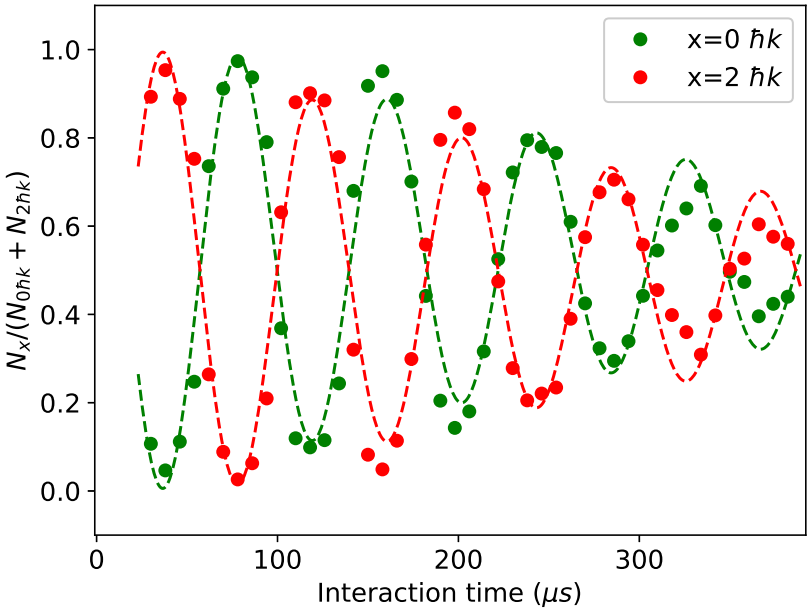

Figure 5.3 – *Rabi oscillations of the atomic sample, showing oscillations between the* $0\hbar k$ *(green) and* $2\hbar k$ *(red) momentum populations, measured with absorption imaging in the horizontal optical lattice, with 150 mW per beam. The fraction of atoms in each state is determined with respect to the total number of atoms in each absorption image. A damped sinusoidal fit (red and green dashed lines) yields a Rabi frequency of 76 kHz, translating to a lattice depth of approximately* $1.2E_R$.

$0.8E_R$ per 100 mW. This matches reasonably well with the expectations from the beam geometry and power. The Rabi oscillations show a clear damping, which is more severe in the vertical lattice than in the horizontal configuration. We attribute this to the vibrations of the lattice beam optics.

We note that we can only measure Rabi frequencies when the potential is small, limited by the timing resolution of the control software and the camera. For deeper lattices we assume a linear scaling of depth with power to extrapolate depths from measurements at lower power. This

was e.g. done to determine the lattice depth of 7.5 E_R for the measurements shown in Fig. 5.7, for which we used the Rabi-measurement that is shown in Fig. 5.3.

5.4 Measuring horizontal Bloch oscillations

We first performed experiments with Bloch oscillations in the horizontal lattice configuration. In this case we produce a BEC in the ODT and then turn it off, while turning the horizontal lattice beams on. As mentioned in Sec. 5.1, we want to prepare the atoms in the first band, because the band gaps become smaller as n, the band index, grows. This means that the avoided crossings become less 'avoided' and that the induced acceleration of the lattice may not be as high as in the first band, for all the atoms to co-accelerate.

To ensure atoms are not prepared in higher bands, the lattice must be turned on adiabatically. The criterion described in [154], which is valid for $U_0 \leq E_R$ and q=0, reads

$$\left| \frac{d}{dt} \frac{U_0}{E_R} \right| \ll 32\sqrt{2} E_R/\hbar. \tag{5.8}$$

When using a lattice depth of 1 E_R, Eq. 5.8 states that the lattice must be turned on slower than 0.2 microseconds, which is the case in our experiments.

The flattening of the band and its derivative is demonstrated in Fig. 5.4, which shows helium atoms that are accelerated at 4 m/s^2 in a horizontal lattice. The two sets of absorption images show the resulting momentum populations after a variable time in the accelerating lattice and a time-of-flight of 5 ms. Atoms in the upper part of the images have accelerated to the $2\hbar k$ momentum state, which we denote by saying they have undergone one BO, or N=1. The atoms in the lower part of the images remain in the $0\hbar k$ momentum state, or N=0.

Fig. 5.4a was measured using a $1.16E_R$ deep lattice, the images correspond to the blue datapoints in Fig. 5.4c. The red datapoints correspond

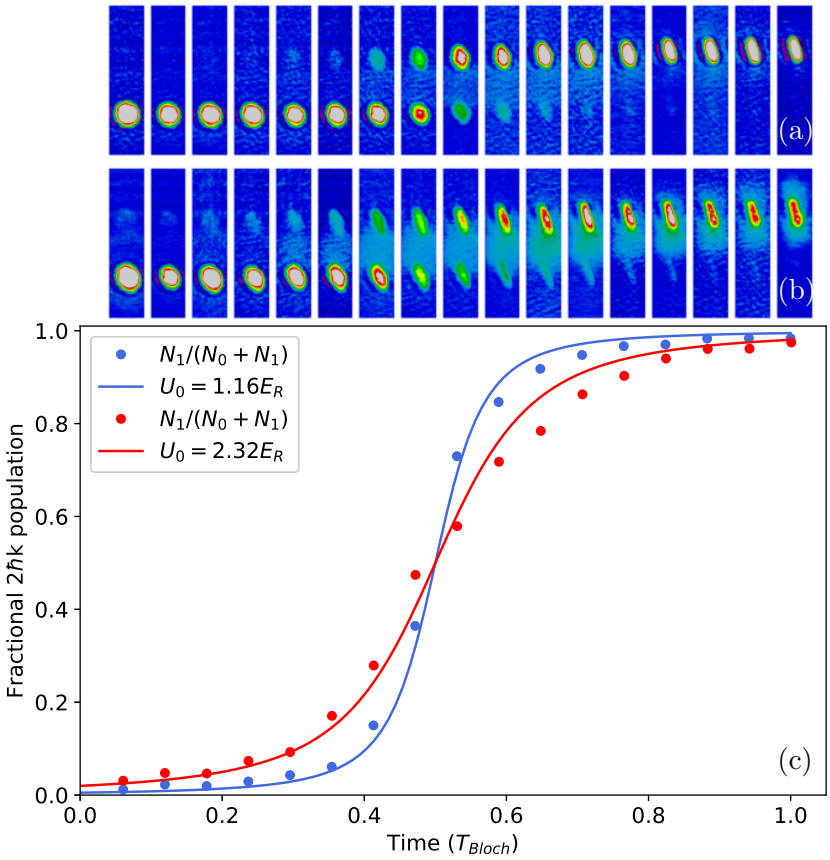

Figure 5.4 – *(a) and (b) Absorption images of the atoms in the horizontal plane after an expansion time of 5 ms, showing atoms that are accelerated by 4 m/s^2 in an optical lattice with a depth of (a) $1.16E_R$ and (b) $2.32E_R$. Atoms at the top of the images have been accelerated to $2\hbar k$. (c) The blue (red) datapoints correspond to the data from (a) ((b)) and show the probability that an atom is successfully accelerated. The population is retrieved from the ratio of the of atoms with momentum $2\hbar k$, relative to the total number of atoms. The blue and red lines show the expected behaviour of the atoms in the lattice, calculated from a calibration of the lattice depth and a two-state model of adiabatic rapid passage between momentum states [156].*

to the data of Fig. 5.4b, taken after acceleration with a $2.32E_R$ deep lattice. Fig. 5.4(c) demonstrates the flattening effect of a deeper lattice on the population of the $2\hbar k$ momentum state. The expected theoretical behaviour, shown as the blue and red lines, was calculated from a two-state model of adiabatic rapid passage between momentum states, as described in Peik *et al.* [156]. The data deviates slightly from the solid lines, which is caused by on the one hand an underestimation of the lattice depth and on the other hand the data analysis of the images, which show a considerable amount of noise around the accelerated atoms, especially in the deeper lattice. We attribute this noise to the small angle between the long axis of the ODT and the lattice, which also causes the shearing effect on the shape of the cloud as the atoms spend more time in the lattice.

5.5 Critical acceleration

In Sec. 5.1, we introduced a splitting of the band structure which allows an atom to adiabatically move over the lowest band and gain two photon momenta of velocity, while remaining in the band. The adiabaticity caveat in this process is related to the acceleration of the lattice. If the acceleration is too high, the probability of co-accelerating with the lattice is reduced. This can be seen as the Landau-Zener probability of successfully traversing an avoided crossing, as shown in Fig. 5.5. A particle can either continue its path in a higher band, in which the probability of co-accelerating reduces even further, or co-accelerate and traverse the avoided crossing. When viewed in the context of adiabatic transitions in the first Brillouin zone, the probability for an atom to succesfully co-accelerate with the lattice is given by the Landau-Zener relation [166]

$$P^N = (\eta(1 - e^{\frac{a_c}{a}}))^N, \tag{5.9}$$

where η denotes the technical efficiency (losses due to frequency- or timing imperfections), N is the number of BO's and a_c is the critical acceleration of He^* which is given by

$$a_c = \frac{\pi\hbar^2 k^3}{64 m_{\mathrm{He}^*}^2} \left(\frac{U_0}{E_R}\right)^2, \tag{5.10}$$

with m_{He^*} the atomic mass of $^4\mathrm{He}^*$ and $\mathrm{E}_R = \frac{\hbar^2 k^2}{2 m_{\mathrm{He}^*}}$ the one-photon recoil energy, with reduced Planck's constant $\hbar$, wavenumber $k = 2\pi/\lambda$ and potential depth U_0.

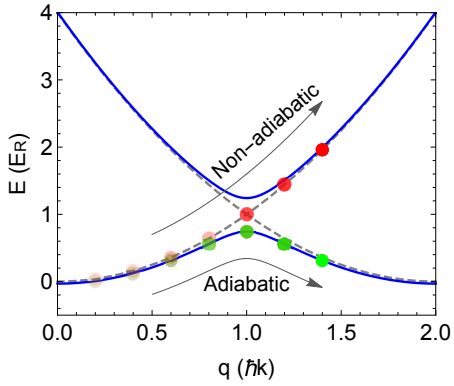

Figure 5.5 – *At the edge of the Brillouin zone, at $q = 1$, the splitting of the band structure (U_0=1 E_R in this graph), creates an avoided crossing. A particle can take the adiabatic- (green) or non-adiabatic (red) route over this crossing. Note that the red path indicates a tunnelling to the next bad, indicating the particle did not co-accelerates with the lattice. (Figure adapted from [166]).*

Fig. 5.6(a), (b) and (c) show absorption images of atoms in the horizontal plane after an expansion time of 5 ms illustrating the momentum distribution of the atoms after being subjected to an accelerated optical lattice with a depth $1.25E_R$ moving towards the right. In (a), the frequency difference between the two lattice beams is chirped from 0 to 660 kHz in 1.4 ms, resulting in an acceleration of about 370 m/s^2. In (b), the frequency is chirped in 0.7 ms, resulting in an acceleration of about 730 m/s^2, and (c) shows a 0.2 ms chirp, or 2600 m/s^2.
As observed from panel (a), the efficiency at low acceleration is near unity, resulting in a bright feature at a position corresponding to atoms that have been given a momentum of $8\hbar k$ (i.e. a velocity of 8×6.4 cm/s^2). At higher acceleration, not all atoms can follow the lattice, leading to a series of features revealing the discrete momentum states separated by $2\hbar k$, as shown in panel (b). At even higher acceleration, the efficiency becomes very small and most atoms remain in the $0\hbar k$ state, as shown in panel (c).

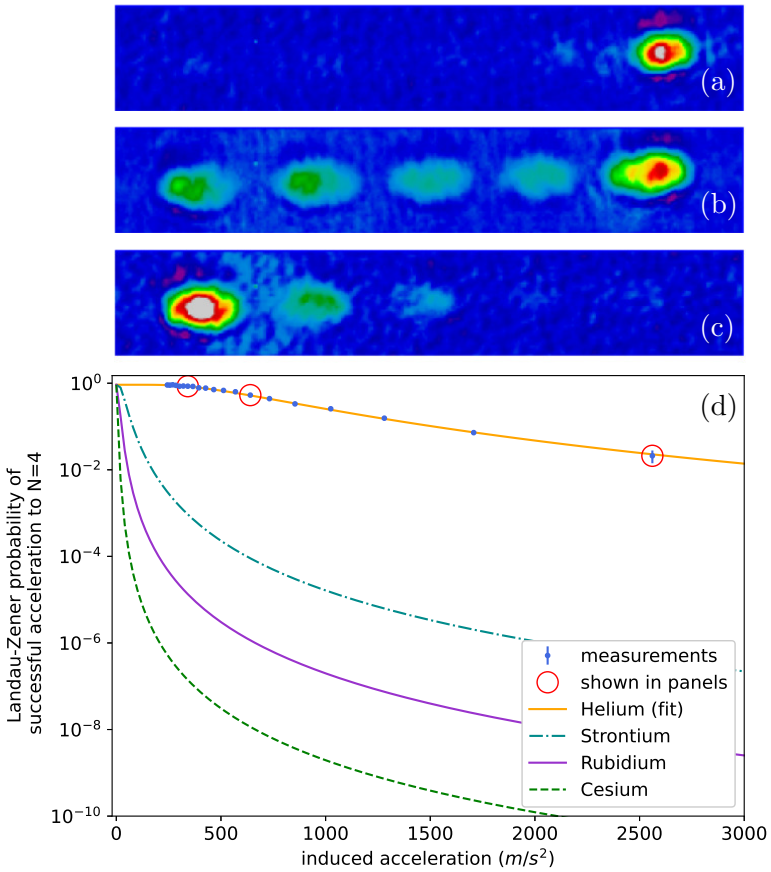

Figure 5.6 – *(a), (b) and (c) Absorption images of the atoms in the horizontal plane after an expansion time of 5 ms, showing atoms that are accelerated by 370 m/s^2 (a), 730 m/s^2 (b) and almost 2600 m/s^2 (c), in an optical lattice with a depth 1.25E_R. Atoms in the right-most feature have been successfully accelerated to 8 $\hbar k$. (d) The blue datapoints show the probability an atom is successfully accelerated to N=4, relative to the total number of atoms. The yellow line is a fit to the data of P^4, shown here to the fourth root (Eq. 5.10, details in text), the red circles show the datapoints related to the image-panels. Theory curves for other atomic species are shown, assuming equal lattice depth but lattice wavelengths commonly used for those species [7, 80, 81].*

The acceleration efficiency is quantified in Fig. 5.6(d) showing the fraction of atoms that is successfully co-accelerated with the lattice to 8 $\hbar k$, as a function of the lattice acceleration. The orange line in Fig. 5.6(d) shows a fit of Eq. 5.9 to the data using $N = 4$, yielding $\eta = 0.980(3)$ and a_c =1294(41) m/s^2. The fitted critical acceleration is in excellent agreement with a_c =1287(9) m/s^2, the value found from Eq. 5.10 with the depth of the lattice derived from a measurement of the Rabi frequency of the atoms in the lattice moving with a velocity of $\hbar k/m_{\mathrm{He}^*}$, i.e., one recoil velocity. The blue, purple and green lines show calculations for ^{88}Sr,^{87}Rb, ^{133}Cs, assuming similar depths for lattices operating at 532 nm, 780 nm and 866 nm, respectively [7, 80, 81], illustrating the relative ease by which helium can be rapidly and efficiently accelerated. Note that with the used settings, we cannot measure accelerations below 250 m/s^2 as in this case the different momentum states are not fully separated on the absorption imaging.

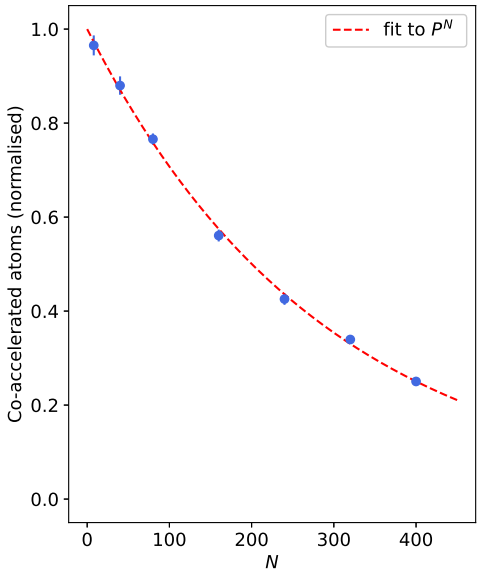

Figure 5.7 – *Normalised number of atoms that have been successfully co-accelerated with the lattice as a function of N, obtained from absorption measurements. The atoms were accelerated and decelerated back and forth with 8 BO's at a time, to a maximum of 400 BO's. The red fit (Eq. 5.9) with $a = 2845.33$ m/s^2 and $a_c = 42944.1$ m/s^2 (deduced from depth calibration using Rabi oscillations) yields an efficiency $\eta = 0.99654(6)$.*

Due to the Gaussian beam shape of the lattice beams, atoms near the center are more efficiently accelerated than those in the wings. As a consequence, the efficiency per BO increases with the number of momenta that are transferred, because the atoms at the wings are lost first. We

have also performed measurements where atoms are driven back and forth for up to 50 times between the $4\hbar k$ and -$4\hbar k$ momentum state, shown in Fig 5.7, transferring up to a total of $800\hbar k$. Here, a lattice depth of approximately $7.3E_R$ and a lattice acceleration of 2.86×10^3 m/s^2 were used. From this measurement an efficiency of 0.99654(7) per oscillation was derived. This is comparable to efficiencies found in other experiments (see for instance [167]). Note that, for helium, far less BO's are needed to achieve a certain velocity than for heavier atoms.

5.6 Measuring vertical Bloch oscillations

We now turn to Bloch oscillations in the vertical plane. In the vertical direction, Earth's gravity provides a constant force along the direction of the lattice giving rise to BO's even when the lattice itself is kept stationary [81]. The relation between the oscillation period, T_{Bloch} and the gravitational acceleration, g, is given by

$$T_{Bloch} = \frac{2\hbar k}{m_{\mathrm{He}^*}\, g}, \tag{5.11}$$

which, in the case of helium in our 1557 nm lattice, is roughly 13 ms. Therefore, by measuring the frequency of the gravity induced Bloch oscillations, g can be measured directly [81]. More elaborate schemes, using a combination of BO's and atom interferometer techniques can improve the sensitivity by several orders of magnitude [80].

Fig. 5.8 shows the atomic cloud after release from the vertical lattice using either absorption imaging after a 5 ms expansion time (panel (a)) or via detection on an MCP detector (panel(c)), revealing the discretised momentum distribution of the cloud. The time the atoms have spent in the vertical lattice is denoted in the panels.

To infer the mean momentum of the atomic cloud at the moment of release, we determine either the mean position of the atoms on the absorption images (blue data points in panel (b)) or the mean arrival time of the atoms on the MCP detector (blue data points in panel (d)),

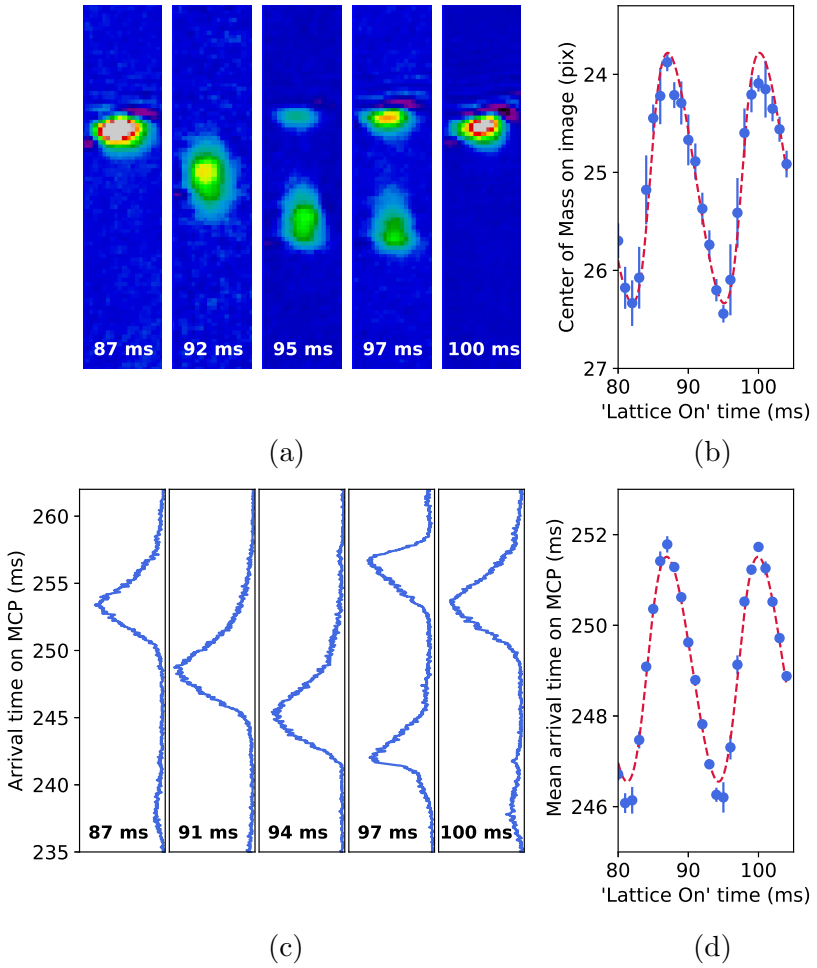

Figure 5.8 – *(a) Absorption image of the atoms in the vertical plane after an expansion time of 5 ms showing Bloch oscillations under gravity. The time that the atoms spent in the lattice for each measurement is denoted in each panel. (b) Mean position of the atoms derived from absorption images as a function of time spent in the lattice (blue data points) (c) Signal observed on the MCP detector after release showing Bloch oscillations under gravity. (d) Mean arrival time of the atoms derived from the MCP traces as a function of time spent in the lattice (blue data points). The red curves in (b) and (d) follow from a band-structure model.*

showing the characteristic sawtooth behaviour expected of Bloch oscillations [154, 155]. Each data point is the average of three measurements. The error bars show the standard deviation of the mean, which is determined by the number of atoms and their momentum spread; i.e., the phase-space density of the sample. This is the motivation for performing these experiments with a Bose-Einstein Condensate.

The red curves shown in panel (b) and (d) of Fig. 5.8 follow from a band-structure model [156] with the input parameters chosen to match the data. Note that the measurements shown in panel (b) and (d) are related to the momentum distribution of the cloud and hence are not sensitive to shot-to-shot fluctuations of the number of atoms. For the data shown in Fig. 5.8, the error obtained with absorption imaging is about 2 times larger than that with the MCP. However, this factor depends strongly on the number of atoms in the sample and (related to that) the voltage that is applied to the MCP detector. Note that all measurements in Fig. 5.8 and Fig. 5.9 have been taken at a constant MCP voltage.

5.7 Measuring gravity

Fig. 5.9 shows the mean arrival time of the atoms falling onto the MCP detector for much longer times spent in the lattice ($0.5E_R$). A clearly measurable contrast up to 6 seconds is obtained in which time the atoms have made over 450 consecutive Bloch oscillations. Panel (b) and (c) of Fig. 5.9 show a zoom-in of the data. Again, each data point is the average of three measurements while the error bar is the standard deviation of the mean.

The number of atoms that remain trapped in the lattice decreases rapidly due to the weak radial confinement. With absorption imaging, no distinguishable signal is observed after 2 seconds, whereas with the MCP detector, a clear signal is observed for up to 6 seconds, at which point the number of atoms has decreased by at least an order of magnitude. Oscillation times up to 12 seconds (not shown) have been observed by

applying higher voltages to the MCP, at which point the number of atoms has decreased with about three orders of magnitude. Counting the signal from individual He* atoms instead of simply measuring the current will likely further extend the time at which the atoms can still be observed [72, 150].

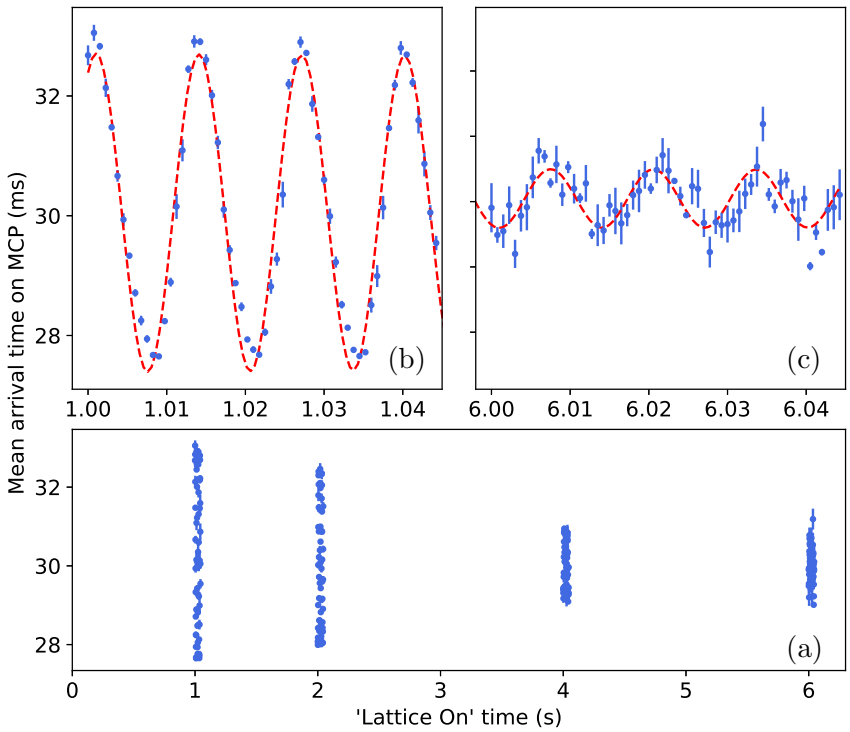

Figure 5.9 – *(a) Mean arrival time of the atoms falling onto the MCP detector as a function of time spent in the lattice ($0.5E_R$), showing Bloch oscillations due to gravity in a lattice. (b) and (c) zoom in showing Bloch oscillations after (b) 1 second and (c) 6 seconds in the lattice. The red line also shown in (b) and (c) is a result of a sinusiodal fit to the data in (a), yielding g=9.7946(4) m/s^2. Note that all measurements have been measured at a constant MCP voltage.*

There are noticeable damping effects on the BO's, which are attributed to three sources of rather different physical origin. (i) Atom-atom interactions; it was shown by Gustavsson *et al.* [168] that atom-atom interactions in a dense BEC lead to dephasing immediately after release of the cloud. In our measurements, we have minimised these effects by introducing a 5 second "hold time" before transferring the atoms to the lattice, at the cost of a reduced signal to noise. Note that it was recently pointed out that atom-atom interactions in a BEC can be used to generate useful entanglement to improve the measurements below the shot noise limit [169], which could directly be implemented in our experiment. (ii) Electronic noise; when the atom number is low, electronic (detector) noise reduces the apparent contrast. This can be avoided by counting the signal from individual atoms [72, 150]. (iii) Acoustic vibrations of the optics; as discussed by Ferrari *et al.* [81] vibrations of the mirrors and fibers will lead to dephasing. In our setup, we use two separate beam paths to create an optical lattice (instead of a retro-reflector) which makes our measurement sensitive to vibrations. We observed that the dephasing is particularly dependent on the alignment of the two lattice beams, which varies from day to day. Increasing the waist of our lattice will likely reduce this effect.

Due to the dephasing, the observed shape of the Bloch oscillation changes from a sawtooth to a sine-like function. This distortion would have to be minimized and modelled for a proper absolute measurement of g from this signal, which was beyond the scope of this experiment. In order to still obtain a statistical uncertainty estimate of our gravity measurement demonstration, we have fitted an (exponentially decaying) sinusoidal function to the data in panel (a) of Fig. 5.9, shown as the red line in panel (b) and (c). This fit yields[2] g =9.7946(4) m/s^2; i.e., a statistical uncertainty for a determination of g of 4×10^{-5}.

[2]It turns out there was a small amount of light from the ODT fibers leaking into the chamber (about 150 μW), to which we attribute the offset from the expected 9.81 m/s^2. In Chapter 6, we explain the mechanism behind this systematic effect.

5.8 Conclusion

We have demonstrated Bloch oscillations with a metastable helium BEC. Due to its light mass, helium can be efficiently accelerated to high velocities which makes it a particularly promising candidate for experiments that benefit from splitting the atomic wavefunction over large distances [157, 158, 170–172]. Our measurements illustrate the high signal-to-noise that can be obtained using an MCP detector. As a result of its low mass, the observed Bloch oscillations of helium are distinctly different from those of heavier atoms; the gravity induced Bloch frequencies in our vertical lattice have a frequency of only 73 Hz, while the characteristic length-scale of the motion of the atoms is as large as 200 μm.[3] This long length scale allows us to accurately determine the influence of a laser beam that is focused at the apex of the trajectories [174]. We plan to use this method to measure the tune-out wavelengths of He as a precise test of quantum-electrodynamic calculations [91].

[3]Note that with lithium atoms, Bloch frequencies as low as 20 Hz and length-scales of 300 μm have been obtained by applying a magnetic field gradient along the lattice direction [173].

CHAPTER 6

Outlook

And so, we have arrived at the final chapter, which serves to show a test of a novel technique of measuring the polarizability of metastable helium and to show and discuss our preliminary measurement of an interferometric signal with He^*, and indicate improvements for future experiments.

6.1 Polarizability measurements

As mentioned in Chapter 1, accurate knowledge of the polarizability is of interest for a variety of applications, such as optical clocks, precision spectroscopy and potential energy landscaping. With the setup that was described in the previous chapters, we have attempted a novel method for measuring the polarizability with Bloch oscillations. The key idea is that the frequency of Bloch oscillations depends on the magnitude of the linear potential. A small pertubation added to the lineair potential will result in a modification of this frequency, which can be accurately measured. This makes it possible to discern the influence of a weak additional force, such as that of a laser beam that is present in the path of the atoms during the BO's.

A schematic of our measurement method is shown in Fig. 6.1. A cold atomic sample, in our case a metastable Helium Bose-Einstein condesate, shown as the black dot, is held in a vertically oriented optical lattice, shown in red. Under gravity, the atoms will continuously per-

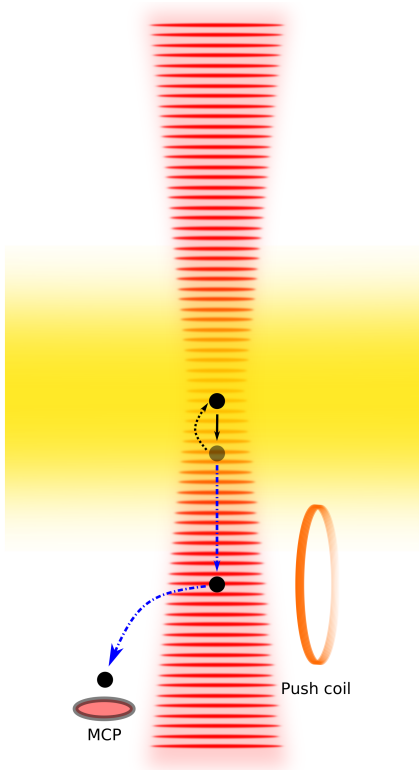

Figure 6.1 – *A schematic of the measurement method. A cold atomic sample, shown as the black dot, is held in a vertically oriented optical lattice, shown in red. Under gravity, the atoms will perform Bloch oscillations in the vertical direction with a characteristic time period, T_{Bloch}. T_{Bloch} is measured by switching off the optical lattice after a variable hold time and record the time it takes the atoms to reach a micro-channel plate (MCP) detector that is mounted off-axis. We superimpose onto the atoms an additional laser beam, shown in yellow, that is aligned in the horizontal plane. This laserbeam is focused such that its intensity varies significantly over the trajectory of the atoms. As a consequence, the atoms will experience a force that leads to a decrease or increase of the oscillation period that depends linearly on the polarizibility of the atom and the intensity of the laserbeam.*

form Bloch oscillations in the vertical direction, with a characteristic time period, T_{Bloch}, as explained in Chapter 5. We now superimpose an additional laser beam (shown in yellow) onto the atoms. This beam, which we call the 'pol-beam', is aligned along the horizontal direction and crosses the trajectory of the oscillating atoms. If the intensity of the pol-beam varies significantly over the trajectory of the atoms, the atoms will experience a wavelength dependent optical dipole force that leads to an acceleration or deceleration with respect to the already present gravitational acceleration, depending on the position of the pol-beam with respect to the atomic trajectory. This will result in a change in the oscillation frequency, which we intend to measure.

6.1.1 Measuring the effect of a HeNe laser on Bloch oscillations

In our experiment we use a helium-neon gas laser at a wavelength of 632.8 nm that is focused to a spot size of roughly 300 μm and an intensity of around 1 mW, resulting in a potential with a height of about 0.3 nK. The wavelength of the helium-neon is blue detuned from the 2^3S_1-2^3P_1 transition in helium, hence the potential is repulsive. The acceleration experienced by He^* is on the order of 0.001 m/s^2, or 10^{-4} g. The red curves in the upper and lower panel of Fig. 6.2 show the expected position and velocity of a single atom as a function of hold time in the lattice obtained from numerical integration of the equations of motion.

The physical effect taking place when turning on the pol-beam is as follows: as a result of the slightly larger acceleration the atom experiences due to the pol-beam, it takes slightly less time for the atom to be accelerated to a velocity of minus $\hbar k$, than would be the case without the pol-beam present. Due to the smaller Bloch period, the red curve slowly runs out of phase with the blue curve, resulting in phase shift of approximately 0.1π after 3 seconds of hold time, after which the atoms have made 227 oscillations.

The pol-beam is focused near the BEC position when it is in the ODT. From knife-edge measurements, the $1/e^2$ waist at the atoms is deter-

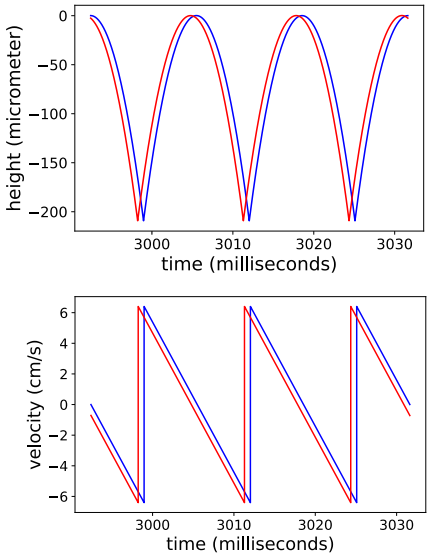

Figure 6.2 – *Numerical simulation of the position (upper panel) and velocity (lower panel) of a metastable atom in an optical lattice at 1557.3 nm as a function of time, with (red) and without (blue) the polarizibility laser present with an intensity and waist similar to those in the experiment. The lattice depth is assumed to be very small so that atoms are only resonant with the lattice light when their velocity is exactly minus $\hbar k = -6.2$ cm/s. The time axis starts after the atoms have made a total of 227 Bloch oscillations.*

mined to be 291 μm in the horizontal direction and 258 μm in the vertical direction. The focusing lens (250 mm focal length) is mounted on a two-axis manual translation stage; since the magnitude of the translations is on the scale of a few hundred microns, we can assume to a good approximation that the pol-beam's focus position at the sample will move by the same amount as the lens translation, as we are effectively moving the optical axis. The power of the helium-neon laser is measured (Thorlabs S120 VC detector) before and after the chamber, the average of the two measurements is taken to be the power seen by the atoms.

The data points in Fig. 6.3 show the mean arrival of He* atoms derived from MCP traces as a function of time spent in an optical lattice. Each data point is the average of 3 runs, each taking approximately 30 seconds. The error bars show the standard deviation of the mean. The black circles represent data taken when the pol-beam is off and only gravity is acting on the atoms. An offset of 223 ms is subtracted from the arrival time.

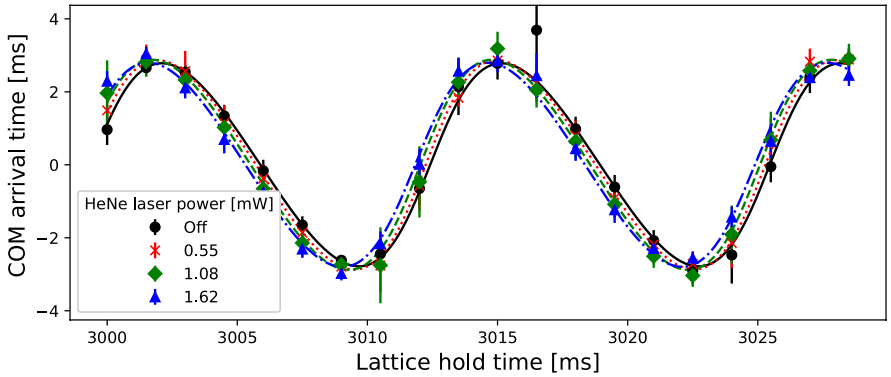

Figure 6.3 – *Bloch oscillations under gravity in the presence of the HeNe 632.8 nm pol-beam at various powers. The data points show the center-of-mass mean arrival time of He* atoms derived from MCP traces as a function of time spent in the optical lattice. An offset of 223 ms is subtracted from the arrival time. The black dots are taken without pol-beam, whereas the red crosses, green diamonds and blue triangles are taken at 0.55, 1.08, and 1.62 mW, respectively. Each data point is the average of 3 measurements. The error bars show the standard deviation of the mean. The curves through the data are a fit using eq. 6.1.*

From Fig. 6.2, we expect the mean arrival time of the atoms to resemble a sawtooth with a periodicity *and* peak to peak height of around 13 ms. As observed in Fig. 6.3, the measured traces appear to be smeared out, with the amplitude being smaller and the rising edge being less abrupt than expected. The smearing out is attributed to a number of reasons, already mentioned in Sec. 5.7. In this figure, we fit the curves using the elementary function representation of a smoothed sawtooth wave

$$\begin{aligned} &t_{\mathrm{arr}}(t_{\mathrm{osc}}, f_{\mathrm{Bloch}}, \delta) = \\ &A\,\frac{\arcsin\left((1-\delta)\sin(2\pi f_{\mathrm{Bloch}}(-2(t_{\mathrm{osc}}-t_0)+1/f_{\mathrm{Bloch}})/4)\right)}{\arcsin(1-\delta)} \\ &\times\,\frac{\arctan\left(\sin(2\pi f_{\mathrm{Bloch}}(t_{\mathrm{osc}}-t_0)/2)/\delta\right)}{\arctan(\frac{1}{\delta})} + C. \end{aligned} \tag{6.1}$$

Here, δ varies between 0 and 1 and determines the sharpness of the sawtooth, 0 being maximally sharp and 1 being a sine wave. The variable t_0 is a delay constant, and the parameters A and C are the amplitude and the vertical offset, which are determined by the fit.

Let us now look at the effect of the pol-beam; the red crosses, green diamonds and blue triangles are taken with a power of 0.55, 1.08, and 1.62 mW, respectively. The red, green and blue curves are fits to the data-points, where f_{Bloch} is fixed at the value found from the fit of the 'off' signal, shown as the black datapoints, and only t_0 is allowed to vary as a fitting parameter. This is justified through the assumption that f_{Bloch} is minimally affected by the presence of the weak pol-beam, and will change with a magnitude well below the fit error based on approximately two fringes. Thus a change of the phase of the oscillation

$$\Delta\phi_{t_0} = 2\pi\frac{\Delta t_0}{T_{\mathrm{Bloch}}} = 2\pi\Delta t_0 f_{\mathrm{Bloch}}, \tag{6.2}$$

can be calculated from a small change in the fitted t_0 value. As observed from Fig. 6.3, the interaction with the pol-beam indeed gives a phase shift of approximately the expected magnitude. However, before we can make this statement more precise, we need to address two issues: Firstly, we observe phase shifts due to mechanical vibrations and temperature changes. We believe this is mainly due to the fact that we use two seperate beam paths to create the optical lattice (instead of a retroreflector), and rather tightly focused laser beams. In order to suppress these shifts, we implemented a "toggle" mode, where we set the hold time to a zero-crossing of the center-of-mass arrival time, for example at 3005 ms in Fig. 6.3. We hold the oscillation time at this setting and alternate runs with the pol-beam on and off, in order to observe the phase shift. In the measurements presented here, we have used the falling edge of the fringe pattern. Once we have improved the stability of the optical setup, we hope to use the rising edge, which is more sensitive.

Secondly, the observed phase shift is very sensitive to the exact alignment of the pol-beam. To gain some insight into the behaviour of the alignment and its effect on the phase shift, the laser focus was scanned in both the horizontal and vertical plane. Fig. 6.4 shows the observed

phase shift of He* atoms after a hold time of 4.00789 seconds, i.e., after completing 307 Bloch oscillation in the optical lattice (blue data points) as a function of the horizontal (a) and vertical (b) position of a helium-neon laser with a power of 1.1 mW. Each data point is the average of 5 measurements of the difference in the arrival time with and without the pol-beam, translated into a phase shift

$$\Delta\phi_{\mathrm{on/off}} = 2\pi \frac{t_{\mathrm{on}} - t_{\mathrm{off}}}{rc} f_{\mathrm{Bloch}}, \tag{6.3}$$

where t_{on} and t_{off} are the measured arrival time with- and without pol-beam, respectively, and rc and f_{Bloch} are the slope of the fringe pattern and the Bloch frequency, respectively, which are obtained from measurements similar to those shown in Fig. 6.3. The error bars show the standard deviation of the mean of this quantity.

The solid red curves also shown in Fig. 6.4 are a fit to the data using a simulation that uses the naive model that was also use to make Fig. 6.2. In order to find the best fit, five parameters are varied: $\alpha_{(\lambda=632.8\ \mathrm{nm})}$, the polarizibility at the wavelength of the pol-beam, w_x and w_y, the waists of the laserfocus in the horizontal and vertical plane, respectively, and two parameters that account for the horizontal and vertical offset of the translation stage with respect to the trap center. The fitted horizontal and vertical offsets have been used to shift the experimental datapoints in Fig. 6.4. The largest positive and negative phase shifts are obtained when the laserbeam is shifted slightly above the highest point of the trajectories (i.e., slightly above the trap center), or slightly below the lowest point of the trajectories, respectively.

In our measurements, the waist of the pol-beam is comparable to the amplitude of the Bloch oscillations, which results in an almost symmetric height profile that resembles the derivative of the intensity profile of the laser beam. When the pol-beam is more tightly focused, the height profile becomes sharper and more asymmetric[1] This measurement demonstrates Bloch oscillations in position space, which sofar has only observed in one experiment using lithium atoms in a tilted lattice

[1] the positive phase shift being larger than the negative phase shift. In future, we plan to test the model more extensively using more tightly focused laser beams.

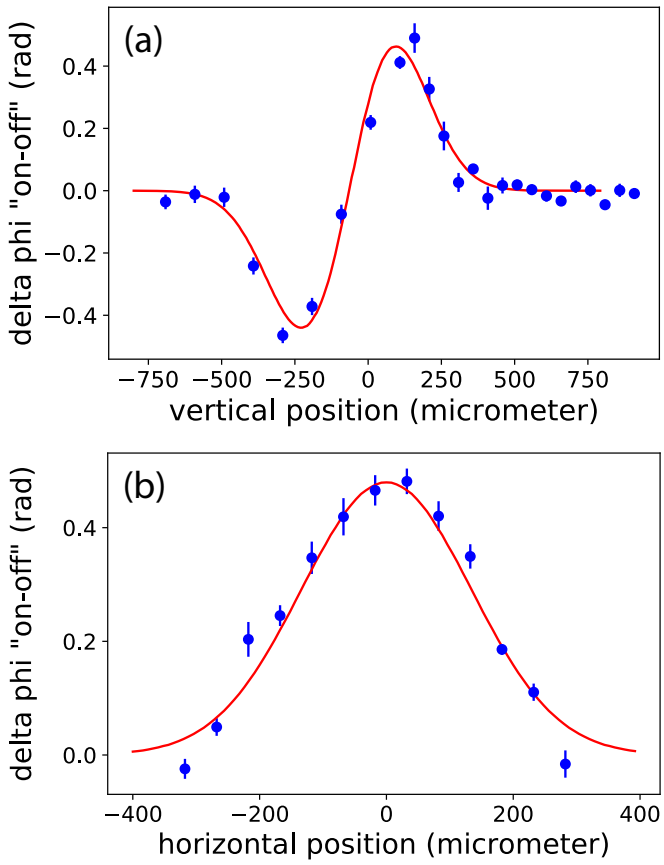

Figure 6.4 – *Observed phase shift of He* atoms after a hold time of 4.00789 seconds, i.e., after completing exactly 307 Bloch oscillation in the optical lattice (blue data points) as a function of the horizontal (a) and vertical (b) position (with respect to the center of the ODT) of a helium-neon laser with a power of 1.1 mW. Each data point is the average of 5 measurements of the difference of the arrival time with and without the pol-beam, translated into a phase shift. The error bars show the standard deviation of the mean. The red curves show a fit to the data using a numerical simulation.*

which is superimposed on a magnetic field gradient [175].

The simulated profiles match well, which gives confidence to the validity our model. We attribute the observed differences between the experimental data and the simulation to the fact that the spatial profile of our pol-beam is not described well by a Gaussian distribution. Best agreement with the experimental data is found with w_x=290 and w_y=270 μm, which is in reasonable agreement with w_x=258 μm and w_y=291 μm obtained from knife-edge measurements. The polarizibility is found to be $\alpha_{(\lambda=632.8\ \mathrm{nm})}$=-162 $\pm$12 $\pm$16 a_0^3, where the first error is the statistical error and the second is the estimated error due to the calibration of the powermeter. The obtained value is in reasonable agreement with the theoretically predicted value of $\alpha_{(\lambda=632.8\ \mathrm{nm})}$=-141 a_0^3 [176] which has an estimated error of 1 %.

Several improvements have yet to be made to the current setup, in order to gain a higher accuracy with this type of measurement. First of all, we have a small amount of light from the ODT leaking into the chamber, which, even though it is 'only' 154 μW, has been shown to give a significant phase shift. Though we assume this has provided a constant and thus common shift in the measurements shown above, it is of course very much an undesired systematic effect.

The first attempt of this technique has yielded a polarizability of He* at 632.8 nm with a statistical uncertainty of about 10 %, but this number could be improved with more measurements and a better determination of the laser parameters. We had planned to use our method to measure tune out wavelengths, particularly, the lowest tune out wavelength in He* at 413 nm, which is currently known with an accuracy of 5 ppm [91] and provides a crucial test of QED. We can use the the data presented in Fig. 6.4 to estimate the expected accuracy for such a measurement. The pol-beam, focused to $\sim$300 μm, gives rise, after the atoms have been held in lattice for 4 seconds, to a phase shift of 2.5 rad/(W$\cdot a_0^3$). The data points have a statistical sensitivity of 25 mrad, or, since each points consists of 10 runs (5 with and 5 without pol-beam) that take approximately 100 seconds in total, a statistical uncertainty of 0.25 rad/$\sqrt{\tau}$, with τ being the measurement time.

The exact tune-out wavelength is found by measuring the polarizibilty at a number of wavelengths around the tune-out wavelength, fit a line to it, and determine the intercept. Close to the tune-out wavelength, the polarizibility has a slope of $\sim$0.4 a_0^3/nm [176]. If we assume that we perform our measurement with an intensity of 100 mW, we would measure a line with a slope of $\sim$0.016 rad/nm. It can be shown [177] that the error in the determination of the intercept is simply the combined uncertainty of the data points divided by the slope, implying that the expected statistical error is equal to $\sim$0.26 nm after a measurement time of 1 hour. Sadly, this number is not at all competive with the measurements by Henson *et al.*[91], who have a statistical error of only 0.9×10^{-3} nm.

Perhaps, this was to be expected given that our current setup is able to measure forces on the order of $10^{-5}g$, whereas state-of-the art experiments reach $10^{-9}g$. Note that the uncertainty of the phase measurements is not much smaller than one would expect from the number of atom that we detect. We are basically deducing the average velocity of our atoms by determining the center of mass of the arrival time distributions. The expected phase uncertainty

$$2\pi \frac{\sigma_t}{\text{slope} \cdot T_{\text{Bloch}}} \frac{1}{\sqrt{n}}, \tag{6.4}$$

with σ_t being the width of the arrival time distibution, which is typically 2 ms, and the slope being the slope of the measured sawtooth, which is $\sim$1. Our measured phase shift implies we have $\sim$1000 atoms per run. This seems a bit small. More likely we have 10-100$\times10^3$ atoms per run, and some other sources of uncertainty; vibrations, electronic noise, etc. Importantly, even detecting 5×10^6 atoms per run would not be enough to reach the desired accuracy.

To be competive we need to perform Bloch oscillations in an interferometer scheme, with the pol-beam in one of the two arms. In this case we are no longer trying to measure a small velocity change of a sample of atoms with a relatively large velocity spread, but we would be measuring the velocity change of each atom individually.

6.2 Atom Interferometry

An interferometer is a measurement device that utilises the wave-nature of light or particles. Traditionally, an interferometer consists of a beam splitter that separates an incoming beam (light or matter) into two or more coherent paths. The outgoing beams are then made to recombine, for example, on a screen, where fringes due to interference can be detected. For interferometers with visible light, this can be done quite easily nowadays. But for matter waves, the associated de Broglie wavelength (Eq. 4.1) is typically 2 to 3 orders of magnitude smaller. The first demonstration that matter exhibits wave-like behaviour was the Davisson-Germer experiment, which showed a diffraction pattern of electrons that were fired at a crystal of nickel [178].

Several famous interferometric measurements are engraved in any physicists mind, for example the optical interferometer that was built by Michelson and Morley [21] to attempt to measure the effect of the 'luminiferous ether' on the speed of light, or one of the first experiments on atom interferometry, Young's double slit experiment, that was coincidentally performed with a beam of He* atoms [179]. Of course, the impressive first observation of a gravitational wave by the LIGO-VIRGO collaboration, using interferometer arms of several kilometres long, must also be mentioned here [180].

Metastable helium has long been interesting from the perspective of matter wave experiments. Examples include transversal Bragg scattering experiments in a well-collimated beam of He* atoms in Eindhoven [181], measurements of the Hanbury Brown-Twiss effect for bosons [182] and fermions [72], measurements of the Hong-Ou-Mandel effect for matter waves [183], and a realization of Wheelers delayed-choice experiment for single massive particles [184].

For understanding a matter-wave interferometer, we can use an analogy of an optical Mach-Zehnder interferometer, which consists of a beam splitter, mirrors and another beam splitter to recombine the beams. Some of the above mentioned experiments demonstrated that material structures such as crystals or microfabricated slits can be used as 'op-

tical elements' for matter waves. For example, the first Mach-Zehnder type matter wave interferometer was constructed with a cold beam of sodium atoms and silicon nitride grating structures [185]. The reversal of the roles of light and matter in an atomic beam type interferometer, when compared to an optical interferometer, was complete when standing light waves were first used as diffraction gratings that acted as beam splitter or combiner [186].

Simultaneously, a pulsed light atom interferometer was developed by Kasevich and Chu [187] in which the atoms were first trapped and cooled and the 'beam-splitters' and 'mirrors' consisted of pulses of optical lattice light, rather than fixed standing light waves. This is also the type of technique we intend to use in our helium interferometer.

To extract information from an atom interferometer, much like with an optical interferometer, we study the information in the interference fringes of the output ports. The phase difference that is picked up along the trajectories of the different arms is what creates the interference. In general, the phase difference between different arms of an interferometer is given by

$$\Delta\phi = \Delta\phi_{laser} + \Delta\phi_{propagation}, \tag{6.5}$$

where the $\Delta\phi_{laser}$ term describes the phase influence of the interaction between the laser light and the atoms, and $\Delta\phi_{propagation}$ is given by the difference in the phase pickup the atoms acquire on the paths of the interferometer. The latter is determined for every segment of the interferometer by the classical action

$$S_{cl} = \int_{t_i}^{t_f} \mathcal{L}(t)dt, \tag{6.6}$$

with Lagrangian $\mathcal{L}(t)$, which depends on the kinetic energy of the atoms and the potential they are subjected to.

6.2.1 π- and $\pi/2$ pulses

In order to make a Mach-Zehnder type interferometer, we need a tool to split up the atomic sample into two velocity classes. In the previous chapter, we have discussed the concept of Rabi-oscillations, where a lattice moving at $1\hbar k/m_{\mathrm{He}}$ with respect to the atomic sample, causes the atoms to oscillate in momentum space between $0\hbar k$ and $2\hbar k$. We can use this phenomenon to our advantage once more by pulsing the lattice on for a brief time so that the populations will be evenly divided over the two momentum states. This occurs when the beam-splitter pulse duration t_{bs} satisfies the condition

$$\frac{U_0}{2\hbar} t_{bs} = \pi/2, \tag{6.7}$$

with depth of the lattice U_0. This beam-splitter pulse is called a '$\pi/2$ pulse'. To invert the velocities of the two clouds that are formed after a $\pi/2$ pulse, we pulse the lattice for a time t_{mirror} that is twice as long as t_{bs}, satisfying

$$\frac{U_0}{2\hbar} t_{mirror} = \pi. \tag{6.8}$$

Such a mirror pulse is called 'π-pulse'. Note that in the case of an atom interferometer, this π-pulse can operate as a mirror for both arms at the same time, unlike in an optical interferometer. Together with our optical lattice and ultracold sample of metastable helium, we now have all the tools we need to make a He* pulsed light atom interferometer.

6.2.2 Mach-Zehnder atom interferometer scheme

Fig. 6.5 shows a typical Mach-Zehnder atom interferometry scheme, with the atomic trajectory in black and the laser-pulses in red. The output ports are the populations of the $0\hbar k$ and $2\hbar k$ momentum states, which can be detected by the methods described in the previous chapters.
The output of such an interferometer is sensitive to the phase shifts induced by the interaction with the laser radiation on the wave function of

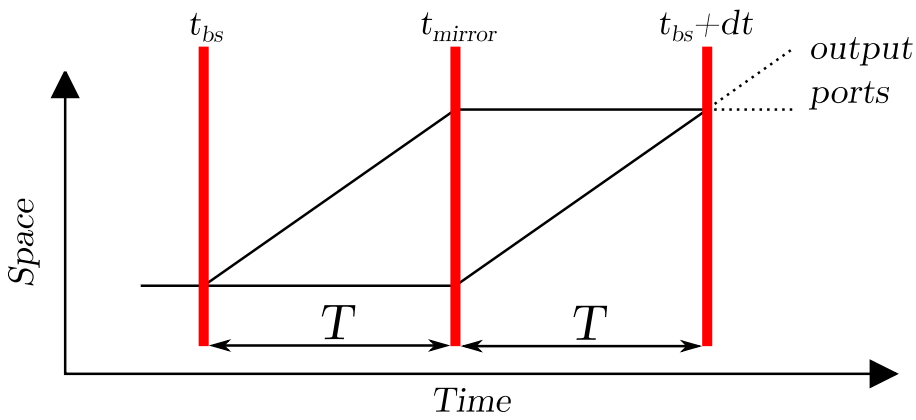

Figure 6.5 – *Schematic Mach-Zehnder atom interferometry sequence. The red lines show the short $\pi/2$ and π pulses, the black lines show the two interferometer arms. The two output ports after the recombination pulse can be detected in the same way as Rabi or Bloch oscillations.*

the atoms and any uniform acceleration that is present on the trajectory of the atoms. The phase of the output fringes depends on these variable as: [188, 189]

$$\Delta\phi = -k_{\text{eff}} a T^2 + \varphi_1 - 2\varphi_2 + \varphi_3, \tag{6.9}$$

with effective wavenumber $k_{\text{eff}} = k_1 + k_2$ (with k_i as the wavenumber of lattice beam i) acceleration a, inter-pulse time T and φ_i the phases of the three laser pulses used to split and recombine the atoms.

The ideal way to measure an acceleration, for example due to magnetic- or electric fields, would be a differential measurement, where the acceleration can be turned on and off manually. For a measurement of gravity, this is unfortunately not possible. Therefore, to measure g in a vertical interferometer setup, one can continuously ramp the lattice frequency, in order to compensate for the gravity-induced Doppler shift.

The Doppler shift that is induced by gravity is at 1557.3 nm about 6 kHz/ms, very small compared to the 82 kHz difference between the lattice beams moving at 1 recoil velocity. On the microsecond time-scale

of the interferometer pulses this is negligible, but at larger inter-pulse-times T, this does start to matter. Perfect compensation should provide an interferometer output with a phase shift that is insensitive to the inter-pulse time T. By maintaining $\Delta\phi$=0 and varying T, the imposed frequency ramp will reveal g.

6.3 First signal of our pulsed light He* interferometer

Our implementation of the scheme depicted in Fig. 6.5 is shown in Fig. 6.6. With this scheme we performed the first proof of principle demonstration of a pulsed light He* atom interferometer.

We made the first $\pi/2$ pulse by turning on one horizontal lattice beam, and flashing the second horizontal lattice beam on for 28 μs (with both lattice beams at 100 mW). The sample was left to evolve over T=100 μs, after which the second lattice beam was flashed on again for 56 μs, to create the π pulse. After another time T, the last pulse was sent, with a variable duration, increasing from 28 μs to 228 μs, in 40 steps of 5 μs.

We varied the time T to check the coherence of the interferometer, with T= 0.1 ms, 0.5 ms and 1 ms. The different measurements were recorded with absorption imaging after 8 ms time of flight. The mean momentum of the atomic cloud shows an oscillation in the populations of the $0\hbar k$ and $2\hbar k$ momentum states as a function of the pulse duration of the last beam-splitter, as expected.

The data was taken before the implementation of the fast RF-switch, which means we had to go to the limit of our computer control system in terms of time resolution. This means we were limited to 'weak' lattices ($<2E_R$), with low Rabi frequencies.

In the figure, the populations of the two momentum states show an offset from 0.5, which we attribute to a background by detection of atoms

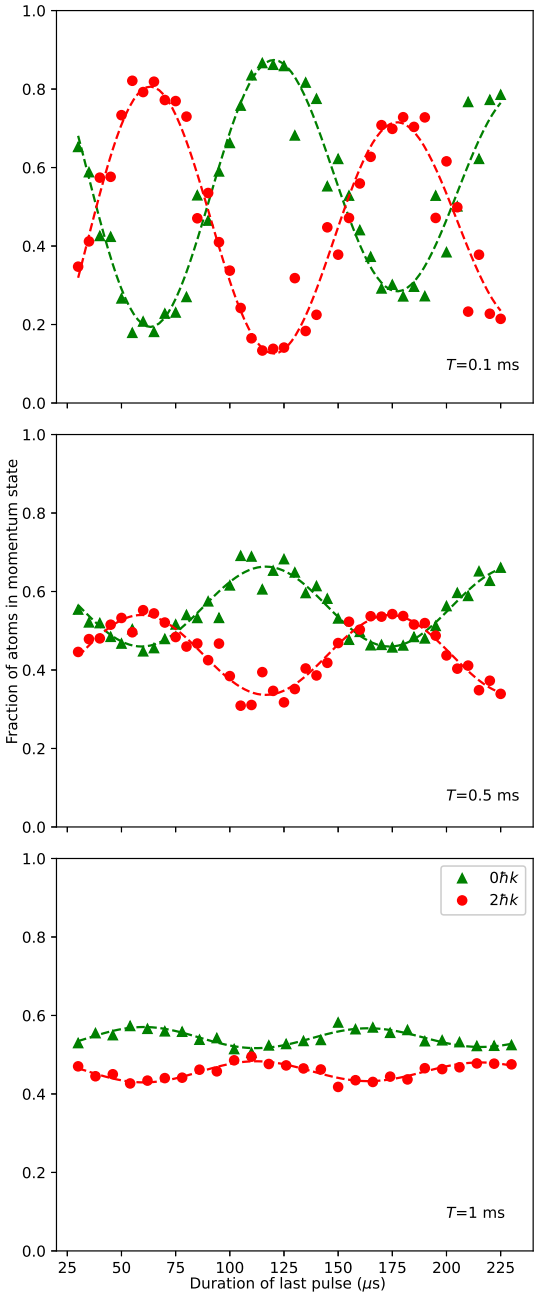

Figure 6.6 – *Proof of principle measurement of a He* atom interferometer with pulsed light. The graphs show the population of the 0ħk (green triangles) and 2ħk (red circles) momentum states, as a function of the duration of the second $\pi/2$ pulse of a horizontally oriented Mach-Zehnder interferometer with a He* BEC. The points are gathered through absorption imaging after an 8 ms time-of-flight. The inter-pulse time T is varied and set (from top to bottom) to 0.1 ms, 0.5 ms and 1 ms, as shown in the graphs.*

that do not participate in the interferometer, and thus contribute to the $0\hbar k$ signal. These could be remaining atoms that are part of the thermal fraction of the BEC, or atoms that do not take part in the sequence due to imperfections in the beam splitter pulses.

The observed contrast of the fringes decreases rapidly as T is increased, which we attribute to a loss of coherence due to vibrations of the lattice optics. The contrast loss that is caused by atoms falling out of the interaction region of the pulses is minimal, as the atoms only fall for about 2 ms, or 10 μm, small compared to the waist of the beam of 200 μm. Furthermore, in our case one of the lattice beams stays on during the interferometer sequence, acting as a waveguide, minimizing vertical movement.

6.4 Prospects for future atom interferometry with He*

The experiment we aimed to perform at the start of the project was a measurement of the recoil velocity. For this, we do not need a Mach-Zehnder, but a different interferometry scheme, called a Ramsey-Bordé interferometer. It consists of four $\pi/2$ pulses and the output phase shift is sensitive to the difference in momentum of the atoms in the different arms during the sequence, scaling quadratically with T. By increasing the velocity with Bloch oscillations in between the two sets of beam-splitter pulses, the sensitivity of the phase shift to the velocity is increased with N, the number of BO's [166].

In principle, we are now able to do this experiment. However, first some improvements must be made to the setup. One of the most important issues with our machine is vibrations of the optics, which washes out the phase coherence of the optical lattice beams. The lattice is especially sensitive to this, since both in the horizontal and vertical configuration, the lattice beams do not share any common optics on the experimental table. Several possible improvements come to mind, for example by strengthening the table that supports the main chamber experiment.

Vibration isolation from turbo pumps and backing pumps is also important, which is currently achieved by a vibration damper (see Fig 2.1, no 22) on the main chamber, but it is not implemented on any of the other turbo's.

Making sure optics are mounted on low, broad mounts is another optional improvement, as is adding weights to the support-structure to lower the eigenfrequencies of the system. This last option has already shown some effect; by adding lead blocks to the breadboard which holds the vertical imaging and lattice optics, a significant reduction of noise and movement, resulting in interference effects in the imaging, was observed.

For gravity measurements in the vertical lattice, as shown in Chapter 5, a better phase coherence between the lattice beams could also be facilitated by retro-reflecting one lattice beam. This would require the vacuum-windows to be anti-reflection coated for 1557 nm to minimise power losses, and a stabilised retro-reflection mirror system. Ideally, the lattice beam would also be collimated instead of focussed.

To improve the coherence of the beam-splitter and mirror pulses, a phase lock of the lattice beams is something we are considering. This could be implemented just before both beams enter the experimental chamber, to maximise the synchronising effect.

Lastly, an issue that is more difficult to overcome; working with the UHV vacuum system, which is real struggle. Every change to the system that involves opening the vacuum requires a full bake-out. This takes over a month of work because it includes realigning almost all of the optical beam paths that enter the main chamber, because the optics that are close to the chamber have to be removed, to allow the magnetic trap coil holders to be removed from the re-entrant windows before a bake. This makes it extremely inconvenient to make even the smallest change to the system, such as replacing windows that are not AR coated for the correct wavelength or checking potentially faulty electrical connections inside the vacuum.

One solution to the vacuum problem that would have been very useful in our setup, is conveniently placed valves that seal different components from each-other, which could reduce the volume that has to be baked out after a small adjustment to the system. We have one pneumatic valve that separates the main chamber from the first part of the Zeeman slower, but several other positions qualify for valve placement.

With this, I would like to end, and conclude that the new experimental setup, that has been over six years in the making, is now almost ready for precision interferometric experiments with helium.

Bibliography

[1] W. Thomson. Notices of the Proceedings at the Meetings of the Members of the Royal Institution of Great Britain with Abstracts of the Discourses. *The Journal of the Royal Institution of Great Britain.*, 16:363–397, 1902.

[2] A. Einstein. Zur Elektrodynamik bewegter Körper. *Ann. Phys.*, 322(10):891–921, 1905.

[3] P. Ehrenfest. Quote retrieved on 17 aug. 2020 from https://en.wikipedia.org/wiki/ultraviolet_catastrophe .

[4] A. Einstein. Über die von der molekularkinetischen Theorie der Wärme geforderte Bewegung von in ruhenden Flüssigkeiten suspendierten Teilchen. *Ann. Phys.*, 322(8):549–560, 1905.

[5] A. Einstein. Über einen die Erzeugung und Verwandlung des Lichtes betreffenden heuristischen Gesichtpunkt. *Ann. Phys.*, 322(6):132–148, 1905.

[6] A. Einstein. Ist die Trägheit eines Körpers von seinem Energieinhalt abhängig? *Ann. Phys.*, 323(13):639–641, 1905.

[7] R. H. Parker, C. Yu, W. Zhong, B. Estey, and H. Müller. Measurement of the fine-structure constant as a test of the standard model. *Science*, 360(6385):191–195, 2018.

[8] L. Morel, Z. Yao, P. Cladé, and S. Guellati-Khélifa. Determination of the fine-structure constant with an accuracy of 81 parts per trillion. *Nature*, 588(7836):61–65, 2020.

[9] D. Hanneke, S. Fogwell, and G. Gabrielse. Cavity control of a single-electron quantum cyclotron; Measuring the electron magnetic moment. *Phys. Rev. A*, 83:052122, 2011.

[10] S. Dimopoulos, P.W. Graham, J.M. Hogan, M.A. Kasevich, and S. Rajendran. Gravitational wave detection with atom interferometry. *Physics Letters B*, 678(1):37 – 40, 2009.

[11] A. Bonnin, N. Zahzam, Y. Bidel, and A. Bresson. Simultaneous dual-species matter-wave accelerometer. *Phys. Rev. A*, 88:043615, 2013.

[12] X. Wu, Z. Pagel, B.S. Malek, T.H. Nguyen, F. Zi, D.S. Scheirer, and H. Müller. Gravity surveys using a mobile atom interferometer. *Science Advances*, 5(9):eaax0800, 2019.

[13] A. Sommerfeld. Über das Spektrum der Röntgenstrahlung. *Ann. Phys.*, 351(6):721–748, 1915.

[14] W. Pauli. Sommerfelds Beitrage zur Quantentheorie. *Die Naturwissenschaften*, 35(5):129–132, 1948.

[15] W. Pauli. Exclusion principle and quantum mechanics. *Nobel Lecture*, 1946.

[16] A. Sommerfeld. Zur Quantentheorie der Spektrallinien. *Ann. Phys.*, 356(17):1–94, 1916.

[17] H. Aspden and D.M. Eagles. Aether theory and the fine structure constant. *Physics Letters.*, 41A(5):423–424, 1972.

[18] B.J. Carr and M.J. Rees. The anthropic principle and the structure of the physical world. *Nature*, 278:605–612, 1979.

[19] J.J. Balmer. Notiz uber die Spectrallinien des Wasserstoffs. *Annalen der Physik*, 261(5):80–87, 1885.

[20] J.R. Rydberg. Recherches sur la constitution des spectres d'emission des elements chimiques. *Kungliga vetenskapsakademiens handlingar*, 23(11):1–155, 1890.

[21] A.A. Michelson and E.W. Morley. On a method of making the wavelength of sodium light the actual and practical standard of length. *Phil. Mag.*, 24(151):463–466, 1887.

[22] M. Planck. Zur Theorie des Gesetzes der Energieverteilung im Normalspectrum. *Verh. Dtsch. Phys. Ges. Berlin 2*, 237, 1900.

[23] N. Bohr. On the constitution of atoms and molecules. *Phil. Mag.*, 26(153):476–502, 1913.

[24] F. Paschen. Bohrs Heliumlinien. *Annalen der Physik*, 355(16):901–940, 1916.

[25] F. Paschen. Die relativistische Feinstruktur von Spektrallinien. *Annalen der Physik*, 387:689–696, 1927.

[26] R.T. Birge. Probable values of the general physical constants. *Rev. Mod. Phys.*, 1:1–73, 1929.

[27] W.N. Bond and D.A. Newton. The values and inter-relationships of c, e, h, M_p, m_o, G and R. *The London, Edinburgh, and Dublin Philosophical Magazine and Journal of Science*, 10(67):994–1003, 1930.

[28] R.T. Birge. Probable values of e, h, $\frac{e}{m}$, and α. *Phys. Rev.*, 40:228–261, 1932.

[29] F.H. Spedding, C.D. Shane, and N.S. Grace. The fine structure of Hα. *Phys. Rev.*, 47:38–44, 1935.

[30] R.T. Birge. A new table of values of the general physical constants (as of august, 1941). *Rev. Mod. Phys.*, 13:233–239, 1941.

[31] U. Stille. Die atomaren Konstantene, e/m_0 und h. *Zeitschrift für Physik*, 121(3):133–200, 1943.

[32] J. W. M. DuMond and E. R. Cohen. Our knowledge of the atomic constants f, n, m, and h in 1947, and of other constants derivable therefrom. *Rev. Mod. Phys.*, 21:651–652, 1949.

[33] H. A. Bethe and C. Longmire. On the experimental value of the fine structure constant. *Phys. Rev.*, 75:306–307, 1949.

[34] J.A. Bearden and J.S. Thomsen. A survey of atomic constants. *Il Nuovo Cimento Series 10*, 5(2):267–360, 1957.

[35] E. R. Cohen and J. W. M. DuMond. Our knowledge of the fundamental constants of physics and chemistry in 1965. *Rev. Mod. Phys.*, 37:537–594, 1965.

[36] W.H. Parker, D.N. Langenberg, A. Denenstein, and B.N. Taylor. Determination of e/h, Using Macroscopic Quantum Phase Coherence in Superconductors. I Experiment. *Phys. Rev.*, 177(2):639–664, 1969.

[37] E.R. Cohen and B.N. Taylor. The 1973 Least-Squares Adjustment of the Fundamental Constants. *J. Phys. Chem. Ref. Data*, 2(4):663–734, 1973.

[38] K. von Klitzing, G. Dorda, and M. Pepper. New Method for High-Accuracy Determination of the Fine-Structure Constant Based on Quantized Hall Resistance. *Phys. Rev. Lett.*, 45:494, 1980.

[39] K. von Klitzing. The quantized Hall effect. *Rev. Mod. Phys.*, 58:519–531, 1986.

[40] E.R. Cohen and B.N. Taylor. The 1986 Adjustment of the Fundamental Physical Constants. *Rev. Mod. Phys.*, 59(4), 1987.

[41] P.J. Mohr and B.N. Taylor. CODATA recommended values of the fundamental physical constants: 1998. *Rev. Mod. Phys.*, 72:351–495, 2000.

[42] P.J. Mohr and B.N. Taylor. CODATA recommended values of the fundamental physical constants: 2002. *Rev. Mod. Phys.*, 77(1):1–107, 2005.

[43] P.J. Mohr, B.N. Taylor, and D.B. Newell. CODATA recommended values of the fundamental physical constants: 2006. *Rev. Mod. Phys.*, 80:633–730, 2008.

[44] G. Gabrielse, D. Hanneke, T. Kinoshita, M. Nio, and B. Odom. Erratum: New Determination of the Fine Structure Constant from the Electron g Value and QED. *Phys. Rev. Lett.*, 99(039902), 2007.

[45] D. Hanneke, S. Fogwell, and G. Gabrielse. New measurement of the electron magnetic moment and the fine structure constant. *Phys. Rev. Lett.*, 100:120801, 2008.

[46] R. Bouchendira, P. Cladé, S. Guellati-Khélifa, F. Nez, and F. Biraben. New determination of the fine structure constant and test of the quantum electrodynamics. *Phys. Rev. Lett.*, 106:080801, 2011.

[47] P.J. Mohr, D.B. Newell, and B.N. Taylor. CODATA recommended values of the fundamental physical constants: 2014. *Rev. Mod. Phys.*, 88:035009, 2016.

[48] T. Aoyama, M. Hayakawa, T. Kinoshita, and M. Nio. Erratum: Tenth-order electron anomalous magnetic moment: Contribution of diagrams without closed lepton loops. *Phys. Rev. D.*, 96:019901(E), 2017.

[49] T. Aoyama, T. Kinoshita, and M. Nio. Revised and improved value of the qed tenth-order electron anomalous magnetic moment. *Phys. Rev. D*, 97:036001, 2018.

[50] E. Tiesinga, P.J. Mohr, D.B. Newell, and B.N. Taylor. The 2018 CODATA Recommended Values of the Fundamental Physical Constants (Web Version 8.1). Available at http://physics.nist.gov/constants, 2020.

[51] A. Sommerfeld. Zur Feinstruktur der Wasserstofflinien. *Naturwissenschaften.*, 28(27):417–423, 1940.

[52] W.E. Lamb and R.C. Retherford. Fine structure of the hydrogen atom by a microwave method. *Phys. Rev.*, 72(3):241–243, 1947.

[53] W.E. Lamb and R.C. Retherford. Fine structure of the hydrogen atom. *Phys. Rev.*, 79(4):549–572, 1950.

[54] H.A. Bethe. The electromagnetic shift of energy levels. *Phys. Rev.*, 72(4):339–341, 1947.

[55] R.P. Feynman, editor. *QED, the strange theory of light and matter.* Princeton University Press, 1988.

[56] B.N. Taylor, W.H. Parker, and D.N. Langenberg. Determination of e/h, Using Macroscopic Quantum Phase Coherence in Superconductors: Implications for Quantum Electrodynamics and the Fundamental Physical Constants. *Reviews of Modern Physics*, 41(3):375–496, 1969.

[57] F.J. Dyson. Divergence of perturbation theory in quantum electrodynamics. *Phys. Rev.*, 85(4):631–632, 1952.

[58] M. Passera. Electron, muon and tau magnetic moments: a theoretical update. *Nucl. Phys. B*, 169:213–225, 2007.

[59] T. Aoyama, M. Hayakawa, T. Kinoshita, and M. Nio. Tenth-order QED contribution to the electron $g - 2$ and an improved value of the fine structure constant. *Phys. Rev. Lett.*, 109:111807, 2012.

[60] T. Aoyama, M. Hayakawa, T. Kinoshita, and M. Nio. Tenth-order electron anomalous magnetic moment: Contribution of diagrams without closed lepton loops. *Phys. Rev. D.*, 91:033006, 2015.

[61] F. Terranova and G.M. Tino. Testing the a_μ anomaly in the electron sector through a precise measurement of h/M. *Phys. Rev. A*, 89:052118, 2014.

[62] S. Sturm, F. Köhler, J. Zatorski, A. Wagner, Z. Harman, G. Werth, W. Quint, C.H. Keitel, and K. Blaum. High-precision measurement of the atomic mass of the electron. *Nature*, 506:467–470, 2014.

[63] M. Wang, G. Audi, A.H. Wapstra, F.G. Kondev, M. MacCormick, X. Xu, and B. Pfeiffer. The AME2012 atomic mass evaluation II: Tables, graphs and references. *CPC(HEP & NP)*, 36(5):1603–2014, 2012.

[64] A. Aspect, E. Arimondo, R. Kaiser, N. Vansteenkiste, and C. Cohen-Tannoudji. Laser Cooling below the One-Photon Recoil Energy by Velocity-Selective Coherent Population Trapping. *Phys. Rev. Lett.*, 61(7):826–829, 1988.

[65] F. Pereira Dos Santos, J. Léonard, J. Wang, C.J. Barrelet, F. Perales, E. Rasel, C.S. Unnikrishnan, M. Leduc, and C.N. Cohen-Tannoudji. Bose-Einstein condensation of metastable helium. *Phys. Rev. Lett.*, 86(16):3459–3462, 2001.

[66] A. Robert, O. Sirjean, A. Browaeys, S. Nowak, D. Boiron, C.I. Westbrook, and A. Aspect. A Bose-Einstein condensate of metastable atoms. *Science*, 292:461–464, 2001.

[67] J.M. McNamara, T. Jeltes, A.S. Tychkov, W. Hogervorst, and W. Vassen. Degenerate Bose-Fermi mixture of metastable atoms. *Phys. Rev. Lett.*, 97:080404, 2006.

[68] M. Wang, G. Audi, F.G. Kondev, W.J. Huang, S. Naimi, and Xing Xu. The AME2016 atomic mass evaluation (II). Tables, graphs and references. *Chinese physics C*, 41(3):30003, 2017.

[69] R.P.M.J.W. Notermans and W. Vassen. High-precision spectroscopy of the forbidden $2\ ^3S_1 \rightarrow 2\ ^1P_1$ transition in quantum degenerate metastable helium. *Phys. Rev. Lett.*, 112:253002, 2014.

[70] NIST online database. http://www.nist.gov/pml/data/index.cfm.

[71] G.V. Shlyapnikov, J.T.M. Walraven, U.M. Rahmanov, and M.W. Reynolds. Decay kinetics and Bose condensation in a gas of spin-polarized triplet helium. *Phys. Rev. Lett.*, 73(24):3247–3250, 1994.

[72] T. Jeltes, J.M. McNamara, W. Hogervorst, W. Vassen, V. Krachmalnicoff, M. Schellekens, A. Perrin, H. Chang, D. Boiron, A. Aspect, and C.I. Westbrook. Comparison of the Hanbury Brown-Twiss effect for bosons and fermions. *Nature*, 445:402–405, 2007.

[73] P. Zeeman. On the influence of magnetism on the nature of light emitted by a substance. *Astrophys. J.*, 5(332):332–347, 1897.

[74] W. Vassen, R.P.M.J.W. Notermans, R.J. Rengelink, and R.F.H.J. van der Beek. Ultracold metastable helium: Ramsey fringes and atom interferometry. *Appl. Phys. B.*, 122:289, 2016.

[75] G.W.F. Drake. Second order Zeeman shift of the $1\ ^1S_0$, $2\ ^1S_0$, and $2\ ^3S_1$ states. *private communication*, 2015.

[76] K. Pachucki. Second order Zeeman shift of the $1\ ^1S_0$, $2\ ^1S_0$, and $2\ ^3S_1$ states. *private communication*, 2015.

[77] D.A. Steck. http://www.steck.us/alkalidata, 2015.

[78] R.P. del Aguila, T Mazzoni, L. Hu, L. Salvi, G.M. Tino, and N. Poli. Corrigendum: Bragg gravity-gradiometer using the $1S0-3P1$ intercombination transition of 88-Sr (2018 New J. Phys. 20 043002). *New Journal of Physics*, 21(1):019502, 2019.

[79] P. Cladé, F. Biraben, L. Julien, F. Nez, and S. Guellati-Khelifa. Precise determination of the ratio h/m_u: a way to link microscopic mass to the new kilogram. *Metrologia*, 53(5):A75–A82, 2016.

[80] M. Andia, R. Jannin, F. Nez, F. Biraben, S. Guellati-Khélifa, and P. Cladé. Compact atomic gravimeter based on a pulsed and accelerated optical lattice. *Phys. Rev. A*, 88:031605, 2013.

[81] G. Ferrari, N. Poli, F. Sorrentino, and G. M. Tino. Long-Lived Bloch Oscillations with Bosonic Sr Atoms and Application to Gravity Measurement at the Micrometer Scale. *Phys. Rev. Lett.*, 97:060402, 2006.

[82] V. Astapenko. *Polarization Bremsstrahlung on Atoms, Plasmas, Nanostructures and Solids.* Springer-Verlag Berlin Heidelberg, 2013.

[83] R. Grimm, M. Weidemüller, and Y.B. Ovchinnikov. Optical dipole traps for neutral atoms. *Adv. At. Mol. Opt. Phys.*, 42:95–170, 2000.

[84] R.P.M.J.W Notermans. *High Precision Spectroscopy of Forbidden Transitions in Ultracold ^4He and ^3He.* PhD thesis, Vrije Universiteit, Amsterdam, 2017.

[85] Masao Takamoto, Feng-Lei Hong, Ryoichi Higashi, and Hidetoshi Katori. An optical lattice clock. *Nature*, 435(7040):321–324, 2005.

[86] J. Mitroy, M.S. Safronova, and C.W. Clark. Theory and applications of atomic and ionic polarizabilities. *J. Phys. B: At. Mol. Opt. Phys.*, 43:202001, 2010.

[87] M.A. Kadar-Kallen and K.D. Bonin. Light-force technique for measuring polarizabilities. *Phys. Rev. Lett.*, 68:2015–2018, 1992.

[88] R. J. Rengelink, Y. van der Werf, R. P.M.J.W. Notermans, R. Jannin, K. S.E. Eikema, M. D. Hoogerland, and W. Vassen. Precision spectroscopy of helium in a magic wavelength optical dipole trap. *Nature Physics*, 14(11):1132–1137, 2018.

[89] L. J. LeBlanc and J. H. Thywissen. Species-specific optical lattices. *Phys. Rev. A*, 75:053612, 2007.

[90] B. Arora, M. S. Safronova, and C.W. Clark. Tune-out wavelengths of alkali-metal atoms and their applications. *Phys. Rev. A*, 84:043401, 2011.

[91] B.M. Henson, R.I. Khakimov, R.G. Dall, K.G.H. Baldwin, L.-Y. Tang, and A.G. Truscott. Precision measurement for metastable helium atoms of the 413 nm tune-out wavelength at which the atomic polarizability vanishes. *Phys. Rev. Lett.*, 115:043004, 2015.

[92] E. Copenhaver, K. Cassella, R. Berghaus, and H. Müller. Measurement of a ^{7}Li tune-out wavelength by phase-patterned atom interferometry. *Phys. Rev. A*, 100:063603, 2019.

[93] B. Décamps, J. Vigué, A. Gauguet, and M. Büchner. Measurement of the 671-nm tune-out wavelength of ^{7}Li by atom interferometry. *Phys. Rev. A*, 101:033614, 2020.

[94] W.F. Holmgren, R. Trubko, I. Hromada, and A.D. Cronin. Measurement of a wavelength of light for which the energy shift for an atom vanishes. *Phys. Rev. Lett.*, 109:243004, 2012.

[95] R. Trubko, M.D. Gregoire, W.F. Holmgren, and A.D. Cronin. Potassium tune-out-wavelength measurement using atom interferometry and a multipass optical cavity. *Phys. Rev. A*, 95:052507, 2017.

[96] R. H. Leonard, A. J. Fallon, C. A. Sackett, and M. S. Safronova. Erratum: High-precision measurements of the ^{87}Rb d-line tune-out wavelength [phys. rev. a 92, 052501 (2015)]. *Phys. Rev. A*, 95:059901, 2017.

[97] F. Schmidt, D. Mayer, M. Hohmann, T. Lausch, F. Kindermann, and A. Widera. Precision measurement of the ^{87}Rb tune-out wavelength in the hyperfine ground state $f = 1$ at 790 nm. *Phys. Rev. A*, 93:022507, 2016.

[98] W. Kao, Y. Tang, N.Q. Burdick, and B.L. Lev. Anisotropic dependence of tune-out wavelength near dy 741-nm transition. *Optics Express*, 25(4):3411, 2017.

[99] R. Bause, m. Li, A. Schindewolf, X. Chen, M. Duda, S. Kotochigova, I. Bloch, and X. Luo. Tune-out and magic wavelengths for ground-state ^{23}na^{40}k molecules. *Physical Review Letters*, 125(2), 2020.

[100] A. J. Daley, J. Ye, and P. Zoller. State-dependent lattices for quantum computing with alkaline-earth-metal atoms. *The European Physical Journal D*, 65(1-2):207–217, 2011.

[101] A. Heinz, A. J. Park, N. Šantić, J. Trautmann, S. G. Porsev, M. S. Safronova, I. Bloch, and S. Blatt. State-dependent optical lattices for the strontium optical qubit. *Phys. Rev. Lett.*, 124:203201, 2020.

[102] R. Trubko, J. Greenberg, M.T. St. Germaine, M.D. Gregoire, W.F. Holmgren, I. Hromada, and A.D. Cronin. Atom interferometer gyroscope with spin-dependent phase shifts induced by light near a tune-out wavelength. *Phys. Rev. Lett.*, 114:140404, 2015.

[103] J. Mitroy and L.-Y. Tang. Tune-out wavelengths for metastable helium. *Phys. Rev. A*, 88:052515, 2013.

[104] G. W. F. Drake, J. G. Manalo, P.-P. Zhang, and K. G. H. Baldwin. Helium tune-out wavelength: Gauge invariance and retardation corrections. *Hyperfine Interactions*, 240(1):31, 2019.

[105] Y. Zhang, F. Wu, P. Zhang, L. Tang, J. Zhang, K. G. H. Baldwin, and T. Shi. Qed and relativistic nuclear recoil corrections to the 413-nm tune-out wavelength for the 2 $^3s_1$ state of helium. *Phys. Rev. A*, 99:040502, 2019.

[106] J. Keppler. De Cometis Libelli Tres. *Augsburg*, 1619.

[107] J. Clerk Maxwell. 1997 VIII. A dynamical theory of the electromagnetic field. *Phil. Trans. R. Soc.*, 155:459–512, 1865.

[108] S. Chu. Nobel lecture: the manipulation of neutral particles. *Rev. Mod. Phys.*, 70:685–706, 1998.

[109] C.N. Cohen-Tannoudji. Nobel lecture: manipulating atoms with photons. *Rev. Mod. Phys.*, 70:707–719, 1998.

[110] W.D. Phillips. Nobel lecture: laser cooling and trapping of neutral atoms. *Rev. Mod. Phys.*, 70:721–741, 1998.

[111] H.J. Metcalf and P. van der Straten. *Laser cooling and trapping.* Springer-Verlag, New York, USA, 1999.

[112] H. Kuhn. *Principles of Physical Chemistry.* John Wiley & Sons, 2009.

[113] A. Bondi. van der Waals Volumes and Radii. *The Journal of Physical Chemistry*, 68(3):441–451, 1964.

[114] S.S. Batsanov. van der Waals Radii of Elements. *Inorganic Materials*, 37:871–885, 2001.

[115] D.W. Fahey, W.F. Parks, and D.L. Schearer. High flux beam source of thermal rare-gas metastable atoms. *Journal of Physics E: Scientific Instruments*, 13:381, 2000.

[116] M.J. Verheijen, H.C.W. Beijerinck, L.H.A.M. van Moll, J. Driessen, and N.F. Verster. A discharge excited supersonic source of metastable rare gas atoms. *Phys. E: Sci. Instrum.*, 17(904):904–910, 1984.

[117] W. Vassen. *Laser spectroscopy of barium and helium Rydberg atoms*. PhD thesis, Vrije Universiteit, Amsterdam, 1988.

[118] W. Rooijakkers, W. Hogervorst, and W. Vassen. Laser deceleration and trapping of metastable helium atoms. *Opt. Commun.*, 135(1-3):149–156, 1997.

[119] W.D. Phillips and H. Metcalf. Laser Deceleration of an Atomic Beam. *Phys. Rev. Lett.*, 48(596):596–599, 1982.

[120] C.J. Foot. *Atomic physics*. Oxford master series in physics. Oxford University Press, 2005.

[121] R.F.H.J. van der Beek. Zeeman Slower Design and Construction. Master thesis, Vrije Universiteit, Amsterdam, 2014.

[122] R.J. Napolitano, S.C. Zilio, and V.S. Bagnato. Adiabatic following conditions for the deceleration of atoms with the Zeeman tuning technique. *Opt. Com.*, 80:110–114, 1990.

[123] N. Vansteenkiste, C. Gerz, R. Kaiser, L. Hollberg, C. Salomon, and A. Aspect. A frequency-stabilized LNA laser at 1.083 μm : application to the manipulation of helium 4 atoms. *Journal de Physique II*, 1(12):1407–1428, 1991.

[124] E. L. Raab, M. Prentiss, A. Cable, S. Chu, and D. E. Pritchard. Trapping of neutral sodium atoms with radiation pressure. *Phys. Rev. Lett.*, 59:2631–2634, 1987.

[125] S. Chu, L. Hollberg, J. E. Bjorkholm, A. Cable, and A. Ashkin. Three-dimensional viscous confinement and cooling of atoms by resonance radiation pressure. *Phys. Rev. Lett.*, 55:48–51, 1985.

[126] R. van Rooij, J.S. Borbely, J. Simonet, M.D. Hoogerland, K.S.E. Eikema, R.A. Rozendaal, and W. Vassen. Frequency metrology in quantum degenerate helium: direct measurement of the $2\ ^3S_1 \rightarrow 2\ ^1S_0$ transition. *Science*, 333:196–198, 2011.

[127] A. Antognini, F. Nez, K. Schuhmann, F.D. Amaro, F. Biraben, F.M.R. Cardoso, D.S. Covita, A. Dax, S. Dhawan, M. Diepold,

L.M.P. Fernandes, A. Giesen, A.L. Gouvea, T. Graf, T.W. Hänsch, P. Indelicato, L. Julien, C.-Y. Kao, P. Knowles, F. Kottmann, E.-O. Le Bigot, Y.-W. Liu, J.A.M. Lopes, L. Ludhova, C.M.B. Monteiro, F. Mulhauser, T. Nebel, P. Rabinowitz, J.M.F. dos Santos, L.A. Schaller, C. Schwob, D. Taqqu, J.F.C.A. Veloso, J. Vogelsang, and R. Pohl. Proton structure from the measurement of $2S - 2P$ transition frequencies of muonic hydrogen. *Science*, 339:417–420, 2013.

[128] T. Bergeman, G Erez, and H.J. Metcalf. Magnetostatic trapping fields for neutral atoms. *Phys. Rev. A*, 35:1535–1546, 1987.

[129] W. Petrich, M.H. Anderson, J.R. Ensher, and E.A. Cornell. Stable, tightly confining magnetic trap for evaporative cooling of neutral atoms. *Phys. Rev. Lett.*, 74(17):3352–3355, 1995.

[130] Yu.V. Gott, M.S. Ioffe, and V.G. Telkovskii. Some new results on confinement in magnetic traps. *Nuclear Fusion, (International Atomic Energy Agency, Vienna*, Suppl. 2, Pt. 3, 1962.

[131] D.E. Pritchard. Cooling neutral atoms in a magnetic trap for precision spectroscopy. *Phys. Rev. Lett.*, 51:1336–1339, 1983.

[132] A.S. Tychkov. *Bose-Einstein condensation of metastable helium atoms*. PhD thesis, Vrije Universiteit, Amsterdam, 2008.

[133] M. Mewes, M. Andrews, N. Van Druten, D. Kurn, D. Durfee, and W Ketterle. Bose-einstein condensation in a tightly confining dc magnetic trap. *Phys. Rev. Lett.*, 77:416–419, 1996.

[134] N. Herschbach. *Trapping triplet helium atoms: inelastic collisions and evaporative cooling*. PhD thesis, Vrije Universiteit, Amsterdam, 2003.

[135] P.O. Schmidt, S. Hensler, J. Werner, T. Binhammer, A. Görlitz, and T. Pfau. Doppler cooling of an optically dense cloud of magnetically trapped atoms. *J. Opt. Soc. Am. B*, 20(5):960–967, 2003.

[136] W. Rooijakkers. *Laser cooling and trapping of metastable helium atoms*. PhD thesis, Vrije Universiteit, Amsterdam, 1997.

[137] R. van Rooij. *Frequency metrology in quantum degenerate helium.* PhD thesis, Vrije Universiteit, Amsterdam, 2012.

[138] M.H. Anderson, J.R. Ensher, M.R. Matthews, C.E. Wieman, and E.A. Cornell. Observation of Bose-Einstein condensation in a dilute atomic vapor. *Science*, 269:198–201, 1998.

[139] K.B. Davis, M.-O. Mewes, M.R. Andrews, N.J. van Druten, D.S. Durfee, D.M. Kurn, and W. Ketterle. Bose-Einstein condensation in a gas of sodium atoms. *Phys. Rev. Lett.*, 75(22):3969–3973, 1995.

[140] A. Einstein. *Quantentheorie des einatomigen idealen Gases*, pages 237–244. Sitzungsberichte der Preussischen Akademie der Wissenschaften. Physikalisch-mathematische Klasse, 1924.

[141] S. Bose. Plancks Gesetz und Lichtquantenhypothese. *Zeitschrift für Physik*, 26(1):178–181, 1924.

[142] M. Fox. *Quantum optics. An Introduction.* OUP Oxford, 2006.

[143] A.S. Tychkov, T. Jeltes, J.M. McNamara, P.J.J. Tol, N. Herschbach, W. Hogervorst, and W. Vassen. Metastable helium Bose-Einstein condensate with a large number of atoms. *Phys. Rev. A*, 73(3):031603(R), 2006.

[144] R.G. Dall and A.G. Truscott. Bose-Einstein condensation of metastable helium in a bi-planar quadrupole Ioffe configuration trap. *Opt. Comm.*, 270:255–261, 2007.

[145] S.C. Doret, C.B. Connolly, W. Ketterle, and J.M. Doyle. Buffer-gas cooled Bose-Einstein condensate. *Phys. Rev. Lett.*, 103:103005, 2009.

[146] M. Keller, M. Kotyrba, F. Leupold, M. Singh, M. Ebner, and A. Zeilinger. Bose-Einstein condensate of metastable helium for quantum correlation experiments. *Phys. Rev. A*, 90:063607, 2014.

[147] Q. Bouton, R. Chang, A.L. Hoendervanger, F. Nogrette, A. Aspect, C.I. Westbrook, and D. Clément. Fast production of

Bose-Einstein condensates of metastable helium. *Phys. Rev. A*, 91:061402(R), 2015.

[148] A.S. Flores, H.P. Mishra, W. Vassen, and S. Knoop. Simple method for producing Bose-Einstein condensates of metastable helium using a single-beam optical dipole trap. *Appl. Phys. B*, 121:391–399, 2015.

[149] R.P.M.J.W. Notermans, R.J. Rengelink, and W. Vassen. Comparison of spectral linewidths for quantum degenerate bosons and fermions. *Phys. Rev. Lett.*, 117:213001, 2016.

[150] W. Vassen, C.N. Cohen-Tannoudji, M. Leduc, D. Boiron, C.I. Westbrook, A.G. Truscott, K. Baldwin, G. Birkl, P. Cancio Pastor, and M. Trippenbach. Cold and trapped metastable noble gases. *Rev. Mod. Phys.*, 84:175–210, 2012.

[151] Y. Castin and R. Dum. Bose-Einstein condensates in time dependent traps. *Phys. Rev. Lett.*, 77(27):5315–5319, 1996.

[152] L. Pitaevskii and S. Stringari. *Bose-Einstein condensation*. Oxford University Press, Oxford, UK, 2003.

[153] P.J.J. Tol. *Trapping and evaporative cooling of metastable helium*. PhD thesis, Vrije Universiteit, Amsterdam, 2005.

[154] M. Ben Dahan, E. Peik, J. Reichel, Y. Castin, and C. Salomon. Bloch oscillations of atoms in an optical potential. *Phys. Rev. Lett.*, 76:4508–4511, 1996.

[155] S. R. Wilkinson, C. F. Bharucha, K. W. Madison, Qian Niu, and M. G. Raizen. Observation of Atomic Wannier-Stark Ladders in an Accelerating Optical Potential. *Phys. Rev. Lett.*, 76:4512–4515, 1996.

[156] E. Peik, M. Ben Dahan, I. Bouchoule, Y. Castin, and C. Salomon. Bloch oscillations of atoms, adiabatic rapid passage, and monokinetic atomic beams. *Phys. Rev. A*, 55:2989–3001, 1997.

[157] P. Cladé, S. Guellati-Khélifa, F. Nez, and F. Biraben. Large momentum beam splitter using bloch oscillations. *Phys. Rev. Lett.*, 102:240402, 2009.

[158] H. Müller, S. Chiow, S. Herrmann, and S. Chu. Atom interferometers with scalable enclosed area. *Phys. Rev. Lett.*, 102:240403, 2009.

[159] F. Bloch. Über die Quantenmechanik der Elektronen in Kristallgittern. *Z. Phys.*, 52:555–600, 1929.

[160] C. Zener. A theory of the electrical breakdown of solid dielectrics. *Proceedings of the Royal Society of London. Series A, Containing Papers of a Mathematical and Physical Character*, 145(855):523–529, 1934.

[161] M. Ben Dahan. *Transport et relaxation d'atomes de cesium; oscillations de Bloch et Resonance de diffusion.* PhD thesis, l'Université Paris IV, 1997.

[162] K. Leo, Bolivar, P.H., Brüggemann, F., Schwedler, R., and Köhler, K. Observation of Bloch oscillations in a semiconductor superlattice. *Solid State Comm.*, 84(10):943 – 946, 1992.

[163] N.W. Ashcroft and N.D. Mermin. *Solid State Physics.* Cengage Learning, 2011.

[164] J.M. Khosrofian and B.A. Garetz. Measurement of a gaussian laser beam diameter through the direct inversion of knife-edge data. *Appl. Opt.*, 22(21):3406–3410, 1983.

[165] M. Cristiani, Oliver Morsch, J. Müller, Donatella Ciampini, and E. Arimondo. Experimental properties of Bose-Einstein condensates in one-dimensional optical lattices: Bloch oscillations, Landau-Zener tunneling, and mean-field effects. *Phys. Rev. A*, 65:063612, 2002.

[166] P. Cladé. Bloch oscillations in atom interferometry. In *Proceedings of the International School of Physics "Enrico Fermi"*, volume 188, pages 237–244, 2013.

[167] P. Cladé, E. de Mirandes, M. Cadoret, S. Guellati-Khélifa, C. Schwob, F. Nez, L. Julien, and F. Biraben. Determination of the Fine Structure Constant Based on Bloch Oscillations of Ultracold Atoms in a Vertical Optical Lattice. *Phys. Rev. Lett.*, 96:033001, 2006.

[168] M. Gustavsson, E. Haller, M. J. Mark, J. G. Danzl, G. Rojas-Kopeinig, and H.-C. Nägerl. Control of Interaction-Induced Dephasing of Bloch Oscillations. *Physical Review Letters*, 100(8):080404, 2008.

[169] S.S. Szigeti, S.P. Nolan, J.D. Close, and S.A. Haine. High Precision, Quantum-Enhanced Gravimetry with a Bose-Einstein Condensate. *arXiv e-prints*, 2020.

[170] T. Kovachy, P. Asenbaum, C. Overstreet, C. A. Donnelly, S. M. Dickerson, A. Sugarbaker, J. M. Hogan, and M. Kasevich. Quantum superposition at the half-metre scale. *Nature*, 528(7583):530–533, 2015.

[171] G. Rosi, G. D'Amico, L. Cacciapuoti, F. Sorrentino, M. Prevedelli, M. Zych, Č. Brukner, and G. M. Tino. Quantum test of the equivalence principle for atoms in coherent superposition of internal energy states. *Nature Communications*, 8(1), 2017.

[172] P. Asenbaum, C. Overstreet, T. Kovachy, D.D. Brown, J.M. Hogan, and M.A. Kasevich. Phase shift in an atom interferometer due to spacetime curvature across its wave function. *Phys. Rev. Lett.*, 118:183602, 2017.

[173] Z.A. Geiger, K.M. Fujiwara, K. Singh, R. Senaratne, S.V. Rajagopal, M. Lipatov, T. Shimasaki, R. Driben, V.V. Konotop, T. Meier, and D.M. Weld. Observation and uses of position-space bloch oscillations in an ultracold gas. *Phys. Rev. Lett.*, 120:213201, 2018.

[174] O. Onishchenko, R.F.H.J. van der Beek, R. Jannin, Y. van der Werf, K.S.E. Eikema, and H.L. Bethlem. *In Preparation*, 2020.

[175] Z.A. Geiger, K.M. Fujiwara, K. Singh, R. Senaratne, S.V. Rajagopal, M. Lipatov, T. Shimasaki, R. Driben, V.V. Konotop, T. Meier, and D.M. Weld. Observation and Uses of Position-Space Bloch Oscillations in an Ultracold Gas. *Phys. Rev. Lett.*, 120:213201, 2018.

[176] R.P.M.J.W. Notermans, R.J. Rengelink, K.A.H. van Leeuwen, and W. Vassen. Magic wavelengths for the $2\ ^3S \rightarrow 2\ ^1S$ transition in helium. *Phys. Rev. A*, 90:052508, 2014.

[177] J.R. Taylor and S.L.L.J.R. Taylor. *Introduction To Error Analysis: The Study of Uncertainties in Physical Measurements*. ASMSU/Spartans.4.Spartans Textbook. University Science Books, 1997.

[178] C. J. Davisson and L. H. Germer. Reflection of electrons by a crystal of nickel. *Proceedings of the National Academy of Sciences*, 14(4):317–322, 1928.

[179] O. Carnal and J. Mlynek. Young's double-slit experiment with atoms: A simple atom interferometer. *Phys. Rev. Lett.*, 66:2689–2692, 1991.

[180] B. P. Abbott and et al. Gw170817: Observation of gravitational waves from a binary neutron star inspiral. *Phys. Rev. Lett.*, 119:161101, 2017.

[181] A. E. A. Koolen, G. T. Jansen, K. F. E. M. Domen, H. C. W. Beijerinck, and K. A. H. van Leeuwen. Large-angle adjustable coherent atomic beam splitter by Bragg scattering. *Phys. Rev. A*, 65:041601, 2002.

[182] M. Schellekens, R. Hoppeler, A. Perrin, J. Viana Gomes, D. Boiron, A. Aspect, and C.I. Westbrook. Hanbury Brown Twiss effect for ultracold quantum gases. *Science*, 310:648–651, 2005.

[183] R. Lopes, A. Imanaliev, A. Aspect, M. Cheneau, D. Boiron, and C.I. Westbrook. Atomic Hong-Ou-Mandel experiment. *Nature*, 520:66–68, 2015.

[184] A.G. Manning, R.I. Khakimov, R.G. Dall, and A.G. Truscott. Wheeler's delayed-choice gedanken experiment with a single atom. *Nat. Phys.*, 11:539–542, 2015.

[185] D. W. Keith, C. R. Ekstrom, Q. A. Turchette, and D. E. Pritchard. An interferometer for atoms. *Phys. Rev. Lett.*, 66:2693–2696, 1991.

[186] E. M. Rasel, M. K. Oberthaler, H. Batelaan, J. Schmiedmayer, and A. Zeilinger. Atom wave interferometry with diffraction gratings of light. *Phys. Rev. Lett.*, 75:2633–2637, 1995.

[187] M. Kasevich and S. Chu. Atomic interferometry using stimulated raman transitions. *Phys. Rev. Lett.*, 67:181–184, 1991.

[188] R. Jannin. *Atom interferometry with a Bose-Einstein condensate: effect of internal interactions*. PhD thesis, Université Pierre et Marie Curie - Paris VI, 2015.

[189] A. Sugarbaker. *Atom Interferometry in a 10 m Fountain*. PhD thesis, Stanford University, 2014.

List of Publications

Chapter 5 is based on:

R.F.H.J. van der Beek, O. Onishchenko, W. Vassen, K.S.E. Eikema, and H.L. Bethlem, "Bloch Oscillations with a metastable Helium Bose-Einstein Condensate," *Phys. Rev. A* **102**, 061302(R), 2020.

The author also contributed to:

W. Vassen, R.P.M.J.W. Notermans, R.J. Rengelink, and R.F.H.J. van der Beek, "Ultracold metastable helium: Ramsey fringes and atom interferometry," *Appl. Phys. B* **122**, 289, 2016.

Summary

THE main subject of this thesis is to demonstrate that helium is a promising candidate for matter wave interferometry, with the goal of providing an improved value for the fine-structure constant, α. In particular, fast and efficient momentum transfer via Bloch oscillations in an optical lattice is demonstrated, together with the enhanced sensitivity offered by an ion-detector based detection scheme that is unique to He^*. The experiments are performed in a setup that was built to produce, slow down and trap ultracold ($\approx$0.2 μK) metastable ^{4}He atoms.

The approach to realising an ultracold sample of He^* atoms consists of a sequence of trapping and cooling stages. The experiment starts at the plasma discharge source, where helium atoms are excited to the so-called metastable 2^3S_1 state, with a lifetime of $\sim$7800 seconds, 20 eV above the atomic ground state. The atomic beam exiting from the source is 2-D collimated by 1083 nm laser light, resonant to the closed 2^3S_1- 2^3P_2 cooling transition. Next, the atoms are slowed down from about 1000- to 50 m/s in a two meter long Zeeman slower through continuous absorption of resonant 1083 nm light. The slowed atoms are captured in a Magneto-Optical Trap (MOT), that holds up to 5×10^8 atoms at a temperature of 1 mK.

The MOT cloud is compressed, spin-polarised and transferred to a cloverleaf Magnetic Trap (MT), which provides both axial and radial trapping through a set of coils outside the vacuum. In the MT, 1D-Doppler cooling is applied to the atomic sample to reduce the temperature to about 150 μK. Following this step, the temperature is reduced further by forced evaporative radio-frequency cooling, resulting in the onset of a Bose-Einstein Condensate (BEC). The atoms are transferred from the MT to a crossed horizontal optical dipole trap (ODT), in which the sample is

further evaporatively cooled to produce a BEC of 5×10^6 atoms.

The BEC is then transferred from the ODT to either a horizontal or vertical optical lattice, consisting of two counter-propagating laser beams at 1557 nm. By detuning the frequency of one of the lattice beams, the standing wave can be accelerated. The trapped helium atoms can follow the accelerating lattice through a process called Bloch oscillations (BO's), which describes the behaviour of particles in a periodic potential that are subjected to a force. Specifically, in this scenario, particles' velocities increase in increments of two recoil velocities, instead of continuously. Bloch oscillations of cold atoms in periodic potentials formed by optical lattices were first studied in 1996. Importantly, BO's provide a way to efficiently accelerate atoms by coherently transferring a well controlled, large number of photon momenta, which has been used to increase the resolution of recoil measurements with caesium and rubidium atoms.

In this thesis, Bloch oscillations with a metastable helium BEC are demonstrated. Due to its light mass, helium can be efficiently accelerated to high velocities which makes it a candidate for experiments that benefit from splitting the atomic wave-function over large distances. Additionally, Rabi-oscillations in an optical lattice are shown, which serve to probe the depth of the lattice, and a measurement of gravity through Bloch oscillations in a static vertical optical lattice is demonstrated, with a statistical uncertainty of 4×10^{-5}. Finally, the first proof of principle demonstration of a pulsed light He^* atom interferometer is shown. The measurements illustrate the high signal-to-noise that can be obtained using an MCP detector. Next to that, we have demonstrated a measurement method for determining the polarizability of an atom at a specific wavelength, by observing the induced change of of the characteristic Bloch oscillation frequency by introducing that wavelength to the system.

Samenvatting

In dit proefschrift worden experimenten beschreven die aantonen dat helium een geschikte kandidaat is voor atoominterferometrie, met het doel om de bepaling van de fijnstructuurconstante, α, op termijn te verbeteren. In het bijzonder wordt snelle en efficiente impulsoverdracht via Bloch oscillaties in een optisch rooster aangetoond, in combinatie met een hoge meetgevoeligheid door gebruik van ionen-detectie methoden, die mogelijk is door de speciale eigenschappen van metastabiel helium. Deze experimenten zijn uitgevoerd in een vacuüm-opstelling die speciaal gebouwd is om metastabiel ^{4}He te produceren, af te remmen, te vangen en af te koelen tot ultrakoude ($\approx$0.2 μK) temperaturen.

Bloch oscillaties van metastabiele heliumatomen in een optisch rooster. Zelfs vertaald in het Nederlands is de titel van mijn proefschrift nog niet vanzelfsprekend begrijpelijk, maar na het lezen van deze samenvatting, is deze hopelijk wel wat duidelijker. Laten we achteraan in de titel beginnen, bij het optisch rooster, een gereedschap dat al vele jaren gebruikt wordt in meerdere velden binnen de natuurkunde. Door twee (al dan niet gefocuste) laserbundels van dezelfde golflengte te overlappen, ontstaat door interferentie tussen de twee lichtbundels een staande golf. De intensiteit van het licht vormt hierbij een regelmatig patroon van pieken en dalen, waarin deeltjes gevangen kunnen worden; een optisch rooster. Het vangen van deeltjes met optische vallen wordt veel gebruikt in de fysica; zo wordt er in de biofysica veel gebruik gemaakt van optische pincetten om bijvoorbeeld DNA te manipuleren, of worden in de atoomfysica neutrale deeltjes gevangen om mee te experimenteren.

Zo ook in dit geval: de deeltjes waarmee wij werken zijn heliumatomen, het tweede element in het periodiek systeem. Omdat helium een relatief eenvoudig systeem is, kunnen theoretici met berekeningen zeer accurate

voorspellingen doen van de interne structuur van het atoom, die vergeleken kunnen worden met nauwkeurige metingen om zo de theorie te testen. Op kamertemperatuur bewegen heliumatomen met een snelheid van zo'n 1300 meter per seconde. Om de lichte heliumatomen onder controle te houden tijdens onze experimenten worden ze afgekoeld tot een fractie van een graad van het absolute nulpunt, waardoor de atomen vrijwel compleet stilstaan. Voordat de atomen gevangen kunnen worden in het optisch rooster, moet het overgrote deel van de snelheid (of temperatuur) er dus al uitgehaald zijn, zonder overmatige verliezen van het aantal atomen.

Het verzamelen van genoeg koude heliumatomen om een experiment te doen is een precair proces, wat begint met het veranderen van de elektronische toestand van het helium atoom naar een configuratie waarmee we het atoom makkelijker kunnen manipuleren; de zogenoemde metastabiele 2^3S_1 toestand, met een levensduur van zo'n 7800 seconden en een interne energie van ongeveer 20 eV. Zodra het atoom zich in deze toestand bevindt, kunnen we met laserlicht met een golflengte van 1083.3 nm het atoom heel precies manipuleren door het continu lichtdeeltjes, ook wel fotonen genoemd, te laten absorberen, waarbij het atoom telkens een klein duwtje krijgt in de richting waarin het licht zich voortbewoog. Dit kan omdat er een overgang van de metastabiele 2^3S_1 naar de 2^3P_2 toestand bestaat die altijd terugvalt naar de metastabiele toestand. Door het laserlicht op precies de juiste frequentie aan te bieden die past bij de overgang, kunnen we de atomen afremmen en vangen.

Om dit alles voor elkaar te krijgen, is een grote vacuüm opstelling gebouwd, schematisch weergegeven in Fig. 2.1 in hoofdstuk 2. Om de atomen in de metastabiele toestand te krijgen, worden ze in de zogenoemde heliumbron (zie Fig. 2.4) langs een naald op hoog voltage geleid, waarbij een plasma ontstaat en de atomen met grote snelheid, meer dan 1000 m/s, in een bundel uit de bron richting de hoofdkamer geschoten worden. Om de atomen te kunnen vangen, moeten ze afgeremd worden tot ongeveer 50 m/s, wat bereikt wordt door een laserbundel tegen de atoombundel in te schijnen. Doordat de atomen continu fotonen absorberen, die elke keer een klein beetje van de snelheid eruithalen,

9.2 cm/s per absorptie, remmen de atomen af. Binnen 2 milliseconden gebeurt dit zo'n 12.500 keer. Omdat de snelheid van de atomen verandert, wordt ook de frequentie van het 1083 nm laserlicht voor de atomen anders, vanwege het Doppler effect (dit effect beschrijft frequentieveranderingen door snelheidsverschillen tussen de waarnemer en de bron, zoals het verschil in de klank van de sirene van een ambulance die aan komt rijden of al voorbij is gereden). Dit compenseren we door een magneetveld aan te leggen over het traject dat de atomen afleggen. Hierbij maken we gebruik van het Zeeman effect, dat beschrijft hoe de energietoestanden in het atoom verschuiven, afhankelijk van de sterkte van het aanwezige magneetveld. Continue afremming van de atomen wordt bereikt door de vorm van het veld precies zo te kiezen, dat het Zeeman effect compenseert voor het Doppler effect op elk punt van het traject van de atomen.

Nadat de atomen afgeremd zijn tot ongeveer 50 m/s, komen ze aan in de hoofd-vacuümkamer. Hier worden de atomen gevangen in een magneto-optische val (MOT). Zoals de naam al doet vermoeden, bestaat die uit een combinatie van een magneetveld en meerdere laserbundels, die de atomen naar het midden van de kamer duwen en genoeg kracht leveren om de zwaartekracht te overwinnen zodat de atomen niet naar beneden vallen. Zo ontstaat er een wolkje van heliumatomen in het centrum van de val van ongeveer 500 miljoen atomen bij een temperatuur van ongeveer 1 milliKelvin. Dit klinkt heel koud, maar het is nog lang niet koud genoeg om de experimenten te doen die wij willen.

Daarom laden we de atomen over in een pure magneetval, die wordt gecreëerd door een aantal sets spoelen die vlak buiten het vacuüm geplaatst zijn. Deze val wordt beschreven in hoofstuk 3. Eenmaal gevangen in het magneetveld van deze val, koelen we de atomen verder door de meest hete atomen eruit te snijden met behulp van een radiofrequentveld, het zogenaamde verdampingskoelen. Dit proces wordt soms vergeleken met het afkoelen van een kop koffie, waarbij het geheel afkoelt door het verdampen van de hete bovenlaag. Hierdoor daalt de temperatuur van de verzameling atomen die we overhouden (zo'n 5×10^6 deeltjes) zo ver dat we niet meer van een temperatuur kunnen spreken, maar dat een gedeelte van de atomen zich in een andere fase-toestand

bevindt; een Bose-Einstein condensaat (BEC). In deze toestand gedragen de atomen zich niet langer als individuele deeltjes, maar vertonen collectief gedrag, dat bepaald wordt door de kwantummechanica.

In hoofdstuk 4 wordt beschreven hoe het BEC vervolgens wordt overgeladen in een optische dipoolval (ODT), die net als het optisch rooster bestaat uit twee overlappende gefocuste laserbundels. Deze bundels zijn, net als alle andere vallen, heel precies uitgelijnd op het centrum van de kamer, zodat de wolk atomen in elke val op dezelfde plek vastgehouden wordt. Het BEC wordt in deze val overgeladen om met de atomen in een magneetveldvrije omgeving te kunnen experimenteren. In de ODT kan het verdampingskoelen worden doorgezet om een puur BEC over te houden, of er kan een optisch rooster in de horizontale of verticale richting worden aangezet om de atomen in te laden. Dit rooster kan vervolgens versneld worden door de frequentie van een van de bundels gecontroleerd te veranderen ten opzichte van de frequentie van de andere bundel. Dit is het punt waarop we het eigenlijke experiment kunnen gaan doen. De voorheen beschreven stappen waren enkel de benodigde voorbereiding.

Zo komen we dus uit bij Bloch oscillaties, een beschrijving van het gedrag van deeltjes onder invloed van een kracht, terwijl ze gevangen zijn in een periodieke structuur,. In ons geval, heliumatomen in een optisch rooster, kunnen we bij een versnelling van het rooster, de atomen die erin gevangen zijn op een heel specifieke manier zien meebewegen. De atomen zullen niet op een continue manier meeversnellen, maar stapsgewijs door middel van de absorptie van een foton uit een van de laserbundels waar het optische rooster uit bestaat, en het uitzenden van een foton in de richting van de andere bundel. Zo versnellen de atomen dus in stappen van tweemaal de impuls van een foton.

In de experimenten in hoofdstuk 5 wordt getoond dat helium door middel van een optisch rooster snel en efficiënt versneld kan worden vanwege haar lage massa. Daarnaast zijn er andere voordelen van het gebruik van helium, zoals de lage tweede-orde gevoeligheid voor magneetvelden, de hoge nauwkeurigheid van de massabepaling en de mogelijkheid tot het gebruik van ionen-detectie methoden vanwege de hoge interne energie

van de metastabiele toestand.

Door het optische rooster verticaal aan te zetten, zonder een frequentieverschil tussen de bundels, staat het rooster ten opzichte van het laboratorium stil. Er is echter nog steeds een kracht aanwezig, die altijd aanwezig is op aarde: de zwaartekracht. De atomen zullen dus in het rooster versneld naar beneden gaan vallen, waardoor vanuit het oogpunt van de atomen juist het rooster omhoog versneld lijkt te worden. Hierdoor zullen de atomen dus Bloch oscillaties gaan vertonen, die erop neerkomen dat de atomen een klein stukje vallen (zo'n 0,2 millimeter), voordat ze terug omhoog versneld worden door middel van absorptie en re-emissie van fotonen. De atomen zullen dus gaan 'stuiteren' in het optisch rooster, op een frequentie die afhankelijk is van de zwaartekracht. Door deze frequentie te meten, meten we dus eigenlijk de zwaartekracht!

Door de atomen een heel aantal keer te laten stuiteren in het optische rooster, kunnen we hele kleine krachten meten, die naast de zwaartekracht ook nog op de atomen werken. Een voorbeeld hiervan is de invloed van een laserbundel, die overlapt met een gedeelte van de afstand die de atomen vallen. Afhankelijk van de golflengte en de sterkte van de laserbundel, zullen atomen hiervan een additionele versnelling ondergaan. Dit uit zich in een frequentieverandering van de Bloch oscillaties die we meten.

Een mogelijke toepassing van deze methode is het bepalen van de gevoeligheid van het heliumatoom voor bepaalde golflengtes. Zo zijn er golflengtes die resonant zijn met een overgang in het atoom, zoals de gebruikte 1083.3 nm, waar het atoom extreem gevoelig voor is. De mate van gevoeligheid wordt uitgedrukt in de zogenoemde polarizeerbaarheid van het atoom, dat voor elke golflengte ander is. Bij een resonante overgang is deze oneindig, omdat het atoom een foton heel makkelijk absorbeert. De golflengte die gebruikt wordt voor de ODT en het optisch rooster, 1557 nm, heeft een polariseerbaarheid die resulteert in een dusdanige attractieve kracht op het helium atoom, dat het gevangen kan worden door gefocuste bundels van deze golflengte.

Er zijn echter ook golflengtes waar het atoom helemaal niets van voelt, een zogenaamde tune-out golflengte. Hier is de polariseerbaarheid gelijk aan 0. Een voor de hand liggende vraag is waarom deze golflengtes überhaupt interessant zijn, ze doen immers per definitie juist niets met het atoom? Voor theoretici blijken echter de precieze waardes van tune-out golflengtes wel degelijk van belang, omdat ze als een nauwkeurige test van de theorie kunnen dienen.

Een tweede vraag die zich vervolgens aandient is wellicht hoe je iets meet wat nu juist geen effect heeft op de atomen? Het antwoord is dat we de golflengte stukje bij beetje kunnen veranderen rondom de verwachte tune-out waarde, en dan meten waar het effect van de laserbundel op de Bloch frequentie minimaal is. Door telkens een meting met en zonder bundel af te wisselen, kunnen we hele kleine veranderingen van de valversnelling meten, en dus de polariseerbaarheid van de bundel daaruit afleiden. Dit experiment was in volle gang tijdens het einde van mijn tijd bij het project, en een kleine vooruitblik is gegeven in het eerste gedeelte van hoofdstuk 6.

Het hoofddoel, het uiteindelijk verbeteren van de bepaling van de fijnstructuurconstante, wordt gedaan door de snelheidsverandering van een helium atoom te meten, nadat het een foton van een bekende energie heeft geabsorbeerd. Hieruit kan dan α worden afgeleid. Om dit heel precies te meten, wordt gebruik gemaakt van atoominterferometrie, dat in bepaalde configuraties gevoelig is voor zeer kleine snelheidseffecten. De basiselementen van een 'klassieke' optische interferometer; een lichtbron, bundelsplitsers en spiegels, hebben allemaal een materiële of optische tegenhanger in de materiegolf-interferometrie. De rollen van materie en licht worden in essentie omgedraaid in deze vorm van interferometrie.

Waar een optische interferometer gebruik maakt van bijvoorbeeld een laserbundel als bron om interferentie te meten, wordt bij materiegolf-interferometrie, of atoominterferometrie, zoals de naam eigenlijk al weggeeft, materie gebruikt in plaats van licht. Dit kan door de atomen, in ons geval dus helium, af te koelen totdat ze zo koud zijn dat ze het eerder beschreven collectieve gedrag gaan vertonen. Dan kunnen we de

wolk atomen beschouwen als materiegolf. Daarnaast is er een optische tegenhanger van de fysieke spiegels; laserpulsen van specifieke lengte en intensiteit, die ervoor zorgen dat stilstaande atomen een bepaalde snelheidsverandering krijgen, en bewegende atomen tot stilstand gebracht worden. Een bundelsplitser wordt optisch gerealiseerd door met een laserpuls enkel de helft van de atomen in een bepaalde snelheidsklasse van snelheid te laten veranderen.

Deze basiselementen worden gedemonstreerd in het tweede deel van hoofdstuk 6. Afsluitend wordt vooruitgeblikt op mogelijke toekomstige experimenten en verbeteringen die daarvoor nodig zijn.

Dankwoord

Bij het schrijven van dit dankwoord werd het me duidelijk dat ik een heleboel mensen dank verschuldigd ben. De belangrijkste is Wim Vassen. Het is moeilijk om je niet meer in persoon te kunnen bedanken voor de kans die je me gegeven hebt en voor de jaren begeleiding bij dit uitdagende project. Zoals ik in mijn eerste mail naar jou schreef, overtuigde jouw enthousiasme me meer dan alle andere factoren om aan dit specifieke project te beginnen.

Er zijn veel momenten waar ik met een glimlach aan terugdenk, zoals toen ik voor het eerst een signaal kreeg van de Zeeman afremmer of voor het eerst een MOT had; Een van de beste dingen daarvan was dat jij daar dan weer heel enthousiast van werd en meteen aan alle knoppen wilde gaan zitten om het beter, groter en mooier te maken.

In het experiment waren er helaas veel meer tegenslagen dan we verwacht hadden. Naast geimplodeerde vacuumvensters, stroomstoringen, kapotte laser-versterkers, kapotte, net nieuw-gekochte laser-versterkers en koelwater overstromingen, was de grootste tegenslag het vacuum, dat maar niet op het benodigde lage niveau wilde komen, ondanks meer dan tien keer inpakken met stooklinten en aluminiumfolie. En hoewel jouw optimisme soms leidde tot moeilijk waar te maken verwachtingen, was het ook zeker een houvast in de tijden dat het experiment niet leek te willen doen wat we wilden.

Helaas mocht zelfs jouw onmetelijke optimisme aan het einde niet baten en hebben we afscheid van je moeten nemen. Het was een voorrecht om met jou gewerkt te mogen hebben en het experiment in jouw naam voort te hebben mogen zetten. De resultaten die uiteindelijk behaald zijn, zijn een eerbetoon aan jouw visie; het is voor eeuwig jammer dat jij ze niet meer hebt mogen meemaken. Ik hoop dat je ze prachtig had gevonden. Bedankt voor alles.

Toen ik in 2014 als masterstudent begon met het interferometrie-project, stond er een lege tafel in het lab en waren er veel mooie ideeen van Wim. Er is een persoon zonder wie veel essentiele onderdelen van de opstelling er niet of veel later waren geweest, Rob Kortekaas, de technicus van de groep. Jij leverde, soms letterlijk, de lijm die de opstelling heel houdt. Wanneer wij promovendi willen werken met laserkoeling, komen we eerst naar jou voor waterkoeling om de lasers op temperatuur te houden, een breadboard om op te bouwen en een mooie doos om erom heen te zetten.

Samen met Hans hebben wij drie kilometer koperdraad om een lange buis gewikkeld en een magneetval ontworpen die werkelijk geen millimeter aan ruimte onbenut liet. De opstelling die er nu staat is voor mij niet alleen een langgerekt metalen ding met zo veel mogelijk niks erin, maar ook een verzameling van vacuumkamers waar ik bij elk onderdeel herinneringen heb over hoe we geworsteld hebben om vacuumflenzen goed op hun plek te krijgen, turbopompen te monteren op onmogelijke hoeken en zelfs ter plekke lekkende lasnaden dicht te lassen. Ik ben ongelofelijk dankbaar voor jouw handige en georganiseerde werkwijze en vele tips over hoe ik het beste kan zagen, boren, vijlen, lektesten, aandraaien, losdraaien, lostrekken, loswrikken, losbreken, schoonmaken, wikkelen en snorkelen. Dankzij jou heb ik na 5 jaar experimentele fysica geen tweede natuurkundige meer nodig om een gloeilamp te vervangen.

Remy and Bob wil ik bedanken voor het het warme welkom in de Helium groep. Zonder jullie was ik misschien nooit doorgerold in het PhD traject; het was altijd supergezellig in het lab! Jullie vaardigheden en behulpzaamheid hebben mij vaak verder geholpen als ik geen idee had wat er aan de hand was met mijn opstelling. Ook moet ik jullie beiden bedanken voor het bijdragen aan het totaal verpesten van mijn gevoel voor humor. Ik heb veel van jullie geleerd en kijk nog steeds op tegen de berg van kennis die jullie graag met mij deelden.

Special thanks also to Adonis. We've worked together for half a year on my machine, during which I learned a lot, possibly the most from your ever-patient and kind attitude. I wish you and your wife Mary-Jane all the best. Thanks are also owed to Hari and Steven, for many interesting stories and lots of help with getting to know the machine.

Toen Remy naar Stanford vertrok en Bob naar Hannover, was ik huiverig om alleen in de helium-hoek te komen te zitten, maar gelukkig kwamen Yuri en Raphael daar snel voor in de plaats. In de moeilijke tijden tijdens Wim's afwezigheid hebben wij samen de boel draaiende gehouden en doorgezet. Ik heb veel steun aan jullie gehad. Het spectroscopie experiment is altijd al een succesverhaal geweest, en jullie zetten dat volgens mij op een bewonderenswaardige manier voort!

Oleksiy werd eind 2018 aangenomen op het interferometrie project om er wat meer vaart in te krijgen. En dat is meer dan gelukt. Jouw frisse blik op het experiment bezorgde me in het begin wat ongemak, omdat ik na veel gedoe met sommige onderdelen een 'als het werkt, kom er dan vooral niet meer aan' houding had ontwikkeld. Maar daar had jij geen boodschap aan en dat bleek soms erg handig. Samen hebben we voor het eerst Bloch oscillaties en interferometrische signalen gezien met helium. Ik realiseerde me pas na enkele maanden hoe ongelofelijk bijzonder deze signalen zijn. Ik kan je niet genoeg bedanken dat jij me geholpen hebt om deze resultaten te realiseren. Bedankt voor alles en heel veel succes en geluk toegewenst in Duitsland, samen met Jackie!

Veel dank ook voor de doctoren en professoren die voor ondersteuning zorgden in de moeilijke omstandigheden en zich inzetten om het project doorgang te laten vinden. Maarten Hoogerland, Wim Ubachs, Kjeld Eikema en Rick Bethlem, veel dank voor alle moeite die jullie erin hebben gestoken! Daarbij ben ik vooral veel dank verschuldigd aan Rick, die de dagelijkse begeleiding van het project overnam en ervoor gezorgd heeft dat er er een strak plan was, er uiteindelijk een artikel gepubliceerd is en dat ik op schema bleef. (Nouja, enigszins dan...)

In de vele jaren in het LaserLaB heb ik vele mensen zien komen en gaan, en al deze mensen hebben op hun eigen manier bijgedragen aan mijn ervaringen in het lab. Door mee te denken met gekke problemen of mooie presentaties te geven, of door gewoon gezellig te kletsen zo nu en dan. Bedankt Elmer, Maarten, Aernout, Frank, Meissa, Joel, Sayan, Matthias, Charlaine, Julian, Mathieu, Robert, Wander, Chungfeng, Edcel, Julia, Mario en nog vele anderen. Daarnaast dank voor de

hardwerkende collega's van de elektronische werkplaats van de VU, Rob, Mario, Lex, Wesley, Pieter en Peter. Zonder jullie hulp in het bouwen van specialistische RF versterkers, FET-schakelingen en HV-versterkers, was veel van het gedane werk niet mogelijk geweest. Ook de fijnmechanische werkplaats verdient veel lof; Frans, Hans, Rob en Joost, jullie hebben veel aandacht geschonken aan de opstelling en ik voelde me altijd welkom om bij jullie binnen te lopen. Ook veel dank aan Marja, Regine en Chandra, voor alle administratieve ondersteuning, en Henk voor het geduldig luisteren.

Laura en Matthijs, ook jullie ben ik natuurlijk ook bijzonder veel dank verschuldigd. Wij hebben samen vanaf de minorkeuze in de bachelor Natuur- en Sterrenkunde, tot het einde van onze opleidingen, alles samen gedaan. En daar hebben jullie mij, zonder dat misschien altijd door te hebben, echt doorheen gesleept! Maar het bleef niet alleen bij studeren natuurlijk. Skivakanties, vele avondjes in het GdG, spelletjes doen, ontspannen in de zon na werktijd, trainen voor triathlons en ga zo maar door! Hierbij ook veel dank aan Vincent, Eelco, Cyriana, Caspar en Dianne. Laura, jij in het bijzonder hebt veel veranderd in mijn leven: je hebt me leren skieen, geleerd wat buitenspel is en me aan het wielrennen gekregen (mijn vader is je daarvoor stiekem heel dankbaar volgens mij).

Daarnaast zijn er heel veel mensen die mij tijdens dit project hebben aangemoedigd of anderszins ondersteund, door een luisterend oor te bieden of voor afleiding te zorgen. Sjoerd en Nanda, Lotte, Thomee, Elke en Leonie, Ananda, Kyra, Kira en Katinka, bedankt voor alle mooie dingen die we hebben gedeeld, die waren altijd een welkome onderbreking op waar ik dan ook mee bezig was. Ik hoop dat er nog vele volgen!

Lieve Pappa, Mamma en Pieter, ik weet niet waar ik moet beginnen bij het uitdrukken van hoe dankbaar ik ben voor jullie steun en liefde. Jullie zijn er altijd als ik jullie nodig heb. Ook al begrepen jullie misschien niet alles van wat ik elke dag in dat lawaaierige lab aan het doen was, 'iets met lasers en vacuum, je wordt er toch niet radioactief van??', was en is er altijd zorg om mijn welbevinden. Bedankt dat jullie het mogelijk maakten dat ik naar het verre Amsterdam kon gaan om te studeren en werken, en dat ik altijd op jullie kon rekenen.

En als laatste Wesley, jij bent altijd mijn zonnetje in huis, ook als het in mijn hoofd regent. Ik ben ongelofelijk gelukkig en trots met jou in mijn leven, en ik zie uit naar alles wat het leven ons gaat brengen.